DEVELOPMENT OF HIGH-BEAM QUALITY HIGH POWER YTTERBIUM-DOPED FIBER LASERS

A DISSERTATION SUBMITTED TO

THE GRADUATE SCHOOL OF ENGINEERING AND SCIENCE

OF BILKENT UNIVERSITY

IN PARTIAL FULFILLMENT OF THE REQUIREMENTS FOR

THE DEGREE OF

DOCTOR OF PHILOSOPHY

IN

MATERIALS SCIENCE AND NANOTECHNOLOGY

By

Yakup Midilli

January 2022

DEVELOPMENT OF HIGH-BEAM QUALITY HIGH POWER YTTERBIUM-DOPED FIBER LASERS

By Yakup Midilli

January 2022

We certify that we have read this dissertation and that in our opinion it is fully adequate, in scope and in quality, as a dissertation for the degree of Doctor of Philosophy.

Bülend Ortaç(Advisor)

Gül Yağlıoğlu

Çağlar Elbüken

Ihor Pavlov

Onur Tokel

Approved for the Graduate School of Engineering and Science:

Ezhan Karaşan
Director of the Graduate School

ABSTRACT

DEVELOPMENT OF HIGH-BEAM QUALITY HIGH POWER YTTERBIUM-DOPED FIBER LASERS

Yakup Midilli
Ph.D. in Materials Science and Nanotechnology
Advisor: Bülend Ortaç
January 2022

High power fiber laser (HPFL) systems have drawn considerable interest for the last decades in health, industry, and especially defense applications due to their compactness, robustness, and high directionality. In this respect, the defense industry is currently in high demand for HPFL systems in the naval, air force, and ground operations. As an example, they have been implemented to the battleship, armored vehicles, and most currently to the drones. Outstanding features of these systems allow us to utilize them in various applications; however, this great demand brings some shortcomings. For example, power scaling of high-power fiber lasers has been impeded by non-linear interactions such as Stimulated Raman Scattering (SRS) and Transverse Mode instability (TMI).

Regarding these non-linear interactions, I have built high-power fiber laser oscillators and amplifier systems based on both commercial and homemade self-fabricated Ytterbium (Yb)-doped large mode area active (LMA) fibers. Amplifier systems have been built based on the Master Oscillator Power Amplifier (MOPA) configuration, and the average power reaches up to 1 kW power level. Besides, the fiber oscillator system has been built with a power level up to 2 kW power level and M^2 value of 1.2, the beam quality parameter of the fiber laser system.

To understand and investigate the TMI effect on the fiber laser system and the fiber itself, I have intended to observe the intensity change of the probe lasers and the color center formation inside a homemade active fiber in the presence of TMI. Then, I have rebuilt the system to eliminate the TMI effect and repeated the same experiments to ensure that the TMI effect was responsible for the difference. For that purpose, I have installed a fiber laser system whose fiber has been coiled in a large bending diameter to ensure the existence of the TMI effect. I have utilized two different probe lasers with 645 nm and 520 nm central wavelengths, respectively. I have coupled these probe lasers to the fiber laser system via free-space arrangements. Afterward, I have repeated the same experiment only with the 520 nm probe laser ensuring the absence of the TMI effect by rebuilding the

laser structure. Finally, I have taken data about the intensity change of the probe lasers for both cases and compared them.

Having benefited from the experience of these studies, to suppress the SRS and TMI, I have fabricated a new type of generation Yb-doped LMA active fiber having an ultra-low numerical aperture (NA) around 0.034. Then I have built a monolithic MOPA system based on this fiber with a 1 m bending diameter. In addition, I have obtained 1 kW maximum power with a diffraction-limited beam quality with an M^2 value of 1.16.

Additionally, I have studied the side-pump combining technique, which is one of the mitigation methods for TMI. It allows us to pump the active fiber from both sides, thus decreasing the thermal load on fiber. Finally, I have studied the side pump combiner on both homemade self-fabricated Photonic Crystal Fiber (PCF) and ultra-low NA active fiber in a (1 + 1) x 1 pumping configuration with 95% and 89% pump coupling efficiencies, respectively.

Keywords: Optical Fibers, Fiber Lasers, Amplifiers, Oscillators, Ultra-low Numerical Aperture, Transverse Mode Instability, Side Pump Combining Technique.

ÖZET

YÜKSEK IŞIN KALİTELİ YÜKSEK GÜÇLÜ İTERBİYUM KATKILI FİBER LAZERLERİN GELİŞTİRİLMESİ

Yakup Midilli
Malzeme Bilimi ve Nanoteknoloji, Doktora
Tez Danışmanı: Bülend Ortaç
Ocak 2022

Yüksek güçlü fiber lazer (YGLS) sistemleri, kompaktlıkları, sağlamlıkları ve yüksek yönlülükleri nedeniyle sağlık, endüstri ve özellikle savunma uygulamalarında son yıllarda büyük ilgi görmüştür. Bu bağlamda, savunma sanayi deniz, hava kuvvetleri ve kara harekatlarında şu anda HPFL sistemleri yüksek talep görmektedir. Örnek olarak, son zamanlarda savaş gemilerine, zırhlı araçlara ve özellikle de dronlara uygulanmaya çalışılmaktadır. Bu sistemlerin üstün özellikleri, onları çeşitli uygulamalarda kullanmamızı sağlar; ancak bu büyük talep bazı eksiklikleri de beraberinde getiriyor. Örneğin, yüksek güçlü fiber lazerlerin güç ölçeklemesi, Uyarılmış Raman Saçılımı (SRS) ve Enine Mod kararsızlığı (TMI) gibi doğrusal olmayan etkileşimler tarafından engellenmiştir.

Bu doğrusal olmayan etkileşimlerle ilgili olarak, hem ticari hem de ev yapımı kendi kendine üretilen İterbiyum (Yb) katkılı geniş mod alanlı aktif (LMA) fiberlere dayalı yüksek güçlü fiber lazer osilatörleri ve yükselteç sistemleri kurdum. Yükselteç sistemleri, Master Osilatör Güç Amplifikatörü (MOPA) konfigürasyonuna dayalı olarak inşa edilmiştir ve ortalama güç 1 kW güç seviyesine ulaşmaktadır. Ayrıca fiber osilatör sistemi, 2 kW güç seviyesine kadar güç seviyesi ve fiber lazer sisteminin ışın kalite parametresi olan 1.2 M^2 değeri ile yapılmıştır.

Fiber lazer sistemi ve fiberin kendisi üzerindeki TMI etkisini anlamak ve araştırmak için, prob lazerlerin yoğunluk değişimini ve TMI varlığında ev yapımı bir aktif fiber içindeki renk merkezi oluşumunu gözlemlemeyi amaçladık. Ardından, TMI etkisini ortadan kaldırmak için sistemi yeniden kurdum ve farktan TMI etkisinin sorumlu olduğundan emin olmak için aynı deneyleri tekrarladım. Bu amaçla, TMI etkisinin varlığını sağlamak için fiberi büyük bir bükülme çapında sarılmış bir fiber lazer sistemi kurdum. Sırasıyla 645 nm ve 520 nm merkezi dalga boylarına sahip iki farklı prob lazer kullandım. Bu prob lazerlerini, boş alan düzenlemeleri aracılığıyla fiber lazer sistemine bağladım. Daha sonra

aynı deneyi sadece 520 nm prob lazer ile tekrarladım ve lazer yapısını yeniden oluşturarak TMI etkisinin olmamasını sağladım. Son olarak, her iki durum için prob lazerlerin yoğunluk değişimi hakkında veri alıp karşılaştırdım.

Bu çalışmaların deneyiminden yararlanarak, SRS ve TMI'yi bastırmak için, 0.034 civarında ultra düşük sayısal açıklığa (NA) sahip yeni bir tür Yb katkılı LMA aktif fiber ürettik. Daha sonra 1 m bükülme çapına sahip bu fibere dayalı monolitik bir MOPA sistemi kurdum. Ayrıca M^2 değeri 1.16 olan ışın kalitesi ile 1 kW maksimum güç elde ettim.

Ayrıca TMI için hafifletme yöntemlerinden biri olan yan pompa birleştirme tekniğini de inceledim. Aktif fiberi her iki taraftan da pompalamamızı sağlar, böylece fiber üzerindeki termal yükü azaltır. Son olarak, sırasıyla %95 ve %89 pompa bağlantı verimliliği ile (1 + 1) x 1 pompalama konfigürasyonunda hem ev yapımı kendinden imal edilmiş Fotonik Kristal Fiber (PCF) hem de ultra düşük NA aktif fiber üzerinde yan pompa birleştiricisini inceledim.

Anahtar sözcükler: Optik Fiberler, Fiber Lazerler, Yükselteçler, Osilatörler, Ultra Düşük Nümerik Açıklık, Aykırı Mod İstikrarsızlığı, Yan Pompalama Birleştirme Tekniği.

This thesis
is dedicated to
the love of
my life
Nazmie
and our
dearest
daughter
İnci.

Acknowledgement

Throughout my 7-year long journey, I have faced obstacles, challenges, hardships, and difficult times besides the happy moments. But, I'm aware that I could not be successful without his support, encouragement, guidance, and supervision. Therefore, first and foremost, I have to thank my supervisor, Assist. Prof. Dr. Bülend Ortaç, this thesis would have never been accomplished without his assistance and dedicated involvement in every step throughout the process. Also, I would like to express my gratitude to Prof. Dr. Gül Yağlıoğlu and Assist. Prof. Dr. Çağlar Elbüken for their contributions, helpful advice, and guidance throughout this study. Besides, I would like to thank the rest of my thesis committee members for their insightful comments and encouragement.

I would also like to extend my deepest gratitude to Elif Yapar Yıldırım and Dr. Ali Karatutlu for their homemade preform and fiber fabrication involvement. I also thank them for their fruitful discussions about the fibers. Special thanks to Dr. Esra Kendir since completing this dissertation would not be possible without her support and deep discussion about the color center observation study.

I'm deeply grateful to Bartu Şimşek for his support, friendship throughout this long journey. We have shared many things and stood for challenges and hardships together. He has also helped me design and fabricate the side pump combiners.

I'm also grateful to my former labmates Elif Uzcengiz Şimşek, Ekin Balk, Uğur Teğin, Tolga Bağcı, Canan Kurşungöz Bağcı, Orhun Kaya, Fehmiye Yıldız for their friendship and support in my experiments.

I am indebted to my parents, Havva and Şahin, my dear sisters, Kevser and Ayşe, and brothers, Adem and İdris, for their unconditional support, patience, and love throughout my life and my education.

Finally, the most significant appreciation goes to my love Nazmie for her endless patience and support about everything. She has endured all of the hardships for me and sacrificed her life, wishes, and desires. I always felt her support and love in my heart. Thus, this thesis is dedicated to the love of my life and our baby girl İnci.

Contents

List of Figures

List of Tables

Chapter 1

Introduction

The first laser operation was observed with a cube of synthetic ruby crystal in 1960 by Theodore H. Maiman [1]. After this pioneering invention, scientists have researched to find new materials suitable for laser operation. For a particular time, gas lasers and conventional bulk solid-state lasers have been widely used for the needs of the industry [2–9]. Then, fiber lasers took the stage due to the industry's growing demand. Power scaling has appeared as the primary motivation, driven by curiosity and to fulfill the enormous demands of scientific and medical applications. Besides, fiber laser would be the candidate for remote monitoring and sensing, free-space communication, material processing, and defense applications due to its extraordinary features compared to the counterparts mentioned above. Fiber lasers can provide high output power, excellent beam quality, narrow line width, and different mode of operation depending on the needs. In that respect, fibers lasers have dominated both the scientific community and the industry since they can respond to their needs faster. In addition, thanks to the physical properties of the optical fiber, robust and light in weight laser systems could be constructed based on them.

After this brief introduction, I would like to summarize the history of the rare-earth-doped optical fibers, which opens the way to high-power fiber laser systems. First of all, the first rare-earth-doped active fiber device was proposed in 1964

with a Neodymium (Nd) element [10]. In this study, a flash lamp was used as a pump source. However, with the development in the semiconductor industry, laser diodes have started to be used as pump sources for fiber lasers. The first usage of laser diodes in a fiber laser system was realized in 1974 [11]. In this study, an Nd-doped silica fiber has been pumped by a Gallium Arsenide (GaAs) laser diode. The Neodymium element was the first dopant for the interest due to its high power operation and efficiency of the 1060 nm transition at the bulk solid-state lasers. The wide availability of the Nd-doped crystalline was another motivation to question the Nd-doped silica fiber fabrication at that time.

After successfully implementing the Nd element inside the optical fiber, a great effort has been made to fabric low-loss active fibers to increase the quality and power handling capacity. For that purpose, utilizing the MCVD system and the solution doping technique together, low-loss rare-earth-doped silica fibers were manufactured first in 1985 with Nd element [12]. Thus, after ten years of intense work, the first single-mode laser was demonstrated using low-loss Nd-doped silica fiber. After that, the success of Nd doping has led researchers to focus on other rare-earth elements such as Erbium (Er), Ytterbium (Yb), Thulium (Tm), Praseodymium (Pr), and Holmium (Ho). Among these rare-earth-elements, firstly, the single-mode laser operation was demonstrated using an Er-doped fiber amplifier in 1987 by Payne et al. [13]. The operating wavelength of the Er-doped fiber corresponds to the telecommunication region (1.55 μm). This situation has led to an increased interest in fiber devices and parallel with the development in fiber technologies. Er-doped fiber amplifiers (EDFA) have dominated the telecommunication industry for a particular time.

Afterward, Yb-doped fibers have taken the stage for a long time especially, in high-power fiber laser systems due to their unique electronic structure [14–27]. Especially after the invention of the Large Mode Area (LMA) optical fibers, the power scaling of Yb-doped fiber lasers has been boosted exponentially beyond the kW power level. In short, the first cladding-pumped Yb-doped fiber amplifier system was demonstrated above 100 W power level in 1999 [28]. After that point, a record power has been achieved beyond the first 1 kW [29] and then 2 kW [30] power levels within just six years. This situation could be possible due to the

remarkable feature of the Yb atom itself. Some of them can be mentioned briefly that quantum defect is relatively small compared to other rare-earth elements. It also has a broad gain bandwidth between 975 nm and 1180 nm wavelength regions. Additionally, it has a very long meta-stable state lifetime of around 1 ms and a simple energy level structure with only two 4f energy levels. These so-called advantages make Yb element the best choice for the high-power laser operation.

In this thesis, I demonstrate high-power Yb-doped fiber laser systems in oscillator and amplifier configuration based on commercial and homemade active fibers. 1 kW and 2 kW power levels have been attained. The possible non-linear limitations, such as Stimulated Raman Scattering (SRS) and Transverse Mode Instability (TMI), have been confronted during the experiments. A new type of active fiber has been offered to solve this problem. Besides, a relationship between the spectroscopic data of the homemade fiber and the TMI effect has been researched extensively. Additionally, the side pump combining technique that allows us to pump the active medium bidirectionally has also been studied on homemade Photonic crystal fiber (PCF) and a unique homemade fiber with ultra-low numerical aperture.

1.1 Theoretical background

In this section, I would like to give some theoretical information about the light-guiding mechanism inside the optical fiber. Then, I will mention the working principle of the lasers briefly. Afterward, I will talk about fiber laser properties such as beam quality. Finally, I will elaborate on the power scaling of Yb-doped fiber lasers and the possible limitations such as Stimulated Raman Scattering (SRS) and Stimulated Brillouin Scattering (SBS).

1.1.1 Optical fibers as a waveguide

In this section, I will give brief information about optical fibers, divided into three in terms of mode content: single-mode, multi-mode, and LMA fibers [31–35]. They are also divided into two, in terms of refractive index profile: step-index and graded-index fibers [36–40]. However, I will focus mainly on the double-clad (DC) large mode area (LMA) step-index fibers [41–43]. They are optical waveguides in which the light propagates along. The standard optical fiber has a layered structure having different refractive indices. The fiber's inner part is called the core region, having a higher refractive index than the outer layer, the cladding region. The main element of the core and the cladding regions is the silica (SiO_2), though the dopants in the core region increase the refractive index, resulting in this difference. This silica glass structure is then coated by low-index acrylic polymer, also called optical polymer, to sustain this wave-guide mechanism. After that, the whole structure is recoated by a high-index polymer, also called mechanical polymer, to sustain the flexibility of the optical fiber. The schematic illustration of a DC LMA fiber's refractive index profile has been shown in **Fig. 1.1a**. Additionally, the corresponding sketch of this fiber has also been shown in **Fig. 1.1b**, pointing out the layered structure of the core, cladding, and polymer regions.

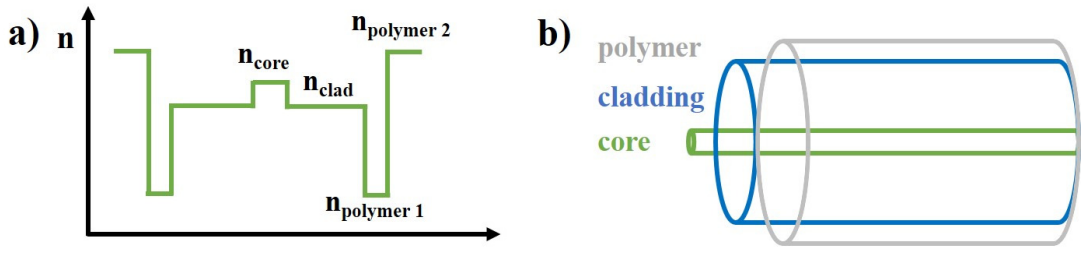

Figure 1.1: (a) The refractive index profile of a double clad step-index optical fiber and (b) the representative sketch illustrating the core, cladding and the polymer regions of it.

$$n_1 \sin\theta_1 = n_2 \sin\theta_2 \tag{1.1}$$

$$n_1 \sin \theta_c = n_2 \sin 90^\circ \tag{1.2}$$

$$\theta_c = \arcsin\left(\frac{n_2}{n_1}\right) \tag{1.3}$$

The light has been refracted while traveling to a medium having a different refractive index. Snell's law governs the relationship between the incidence and the refraction angles as in **Eqn. 1.1** [44–46]. There is a special parameter called the critical angle (θ_c) corresponding to the 90° angle of refraction. It can easily be calculated by using Snell's law as in **Eqn. 1.2** and **Eqn. 1.3**. θ_c is indeed a critical parameter for the wave-guiding mechanism of an optical fiber since when the angle of incidence is bigger than this angle, the incoming ray has been reflected repeatedly inside the optical fiber [47].

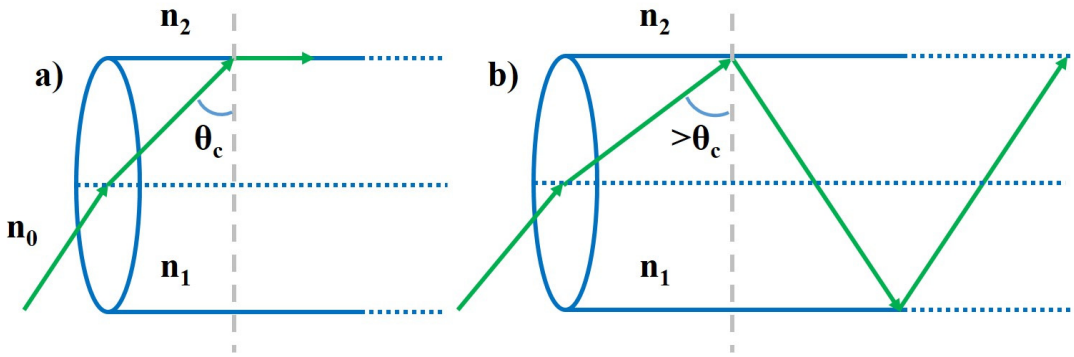

Figure 1.2: The light guiding mechanism inside an optical fiber (a) with critical angle and (b) the total internal reflection.

This phenomenon is called total internal reflection (TIR), responsible for guiding the light ray inside the optical fiber. The schematic illustrations of the θ_c and TIR have been illustrated in **Fig. 1.2a** and **Fig. 1.2b**, respectively.

$$\alpha = \arcsin \frac{1}{n_0} \sqrt{n_{core}^2 - n_{clad}^2} \tag{1.4}$$

$$NA = \sqrt{n_{core}^2 - n_{clad}^2} = \sin \alpha \tag{1.5}$$

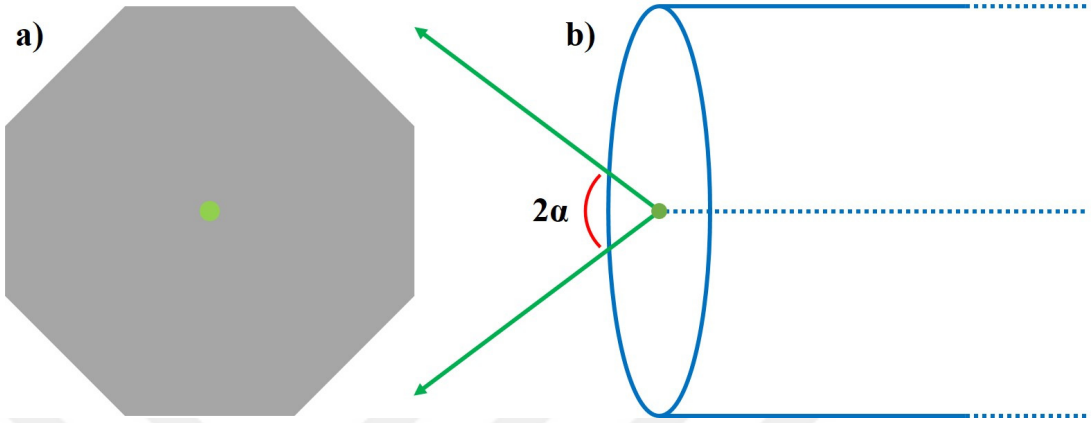

Figure 1.3: (a) The schematic illustration of a octagonal active fiber's cross section and (b) the corresponding drawing of this fiber's acceptance angle.

Another critical parameter related to optical fibers is the acceptance angle (α), defined as the maximum angle of incidence that the fiber can accept [48,49]. This angle could also be derived utilizing Snell's law where n_0 is the refractive index of air, and thus it has been shown as in **Eqn. 1.4**. Moreover, the sine of this angle corresponds to the numerical aperture (NA) of the fiber, shown as in **Eqn. 1.5**. For the sake of illustration, a sketch of the cross-section image of an octagonal active double-clad LMA fiber has been shown in **Fig. 1.3a** and corresponding acceptance angle drawing of the fiber has also been shown in **Fig. 1.3b**.

The acceptance angle is related to the V number parameter and also to the NA of the fiber as shown in **Eqn. 1.6**, where a is the core radius of the fiber. I would like to note that the V number determines the power fraction of modes, supported by the core region of the fiber. The threshold value for an optical fiber's single-mode operation would be 2.405 in the literature [50–52]. Additionally, the V number is an essential parameter of the fiber that directly influences the beam quality of a laser system.

$$V = \frac{2\pi a}{\lambda} \sin \alpha = \frac{2\pi a}{\lambda} NA \tag{1.6}$$

1.1.2 Yb-doped laser gain media

Ytterbium (Yb) is a rare-earth element with an atomic number of 70 with an electronic configuration of $[Xe]6s^24f^{14}$. Yb element has two oxidation states (3+ and 2+); however, Yb^{3+} is favored in laser operations [53, 54]. This element has distinctive properties, such as a simple electronic structure between two states, ground state ($^2F_{7/2}$) and excited state($^2F_{5/2}$) [55, 56]. The electronic level structure of Yb^{3+} with two manifolds has been sketched as shown in **Fig. 1.4**. The ground state has four sub levels, whereas the excited state has three ones. The absorption and the stimulated emission processes occur between these energy levels. For the Yb element, from the ground state to the excitation state, three possible excitation energies correspond to 915 nm, 940 nm, and 975 nm, respectively. The corresponding four possible emission wavelengths from excitation state to the ground state, depending on the pump energy, are 975 nm, 1040 nm, 1080 nm, and 1140 nm, respectively, as sketched in **Fig. 1.4**. Besides the simplicity in the electronic level structure, it has a long upper-state lifetime around hundreds of microseconds or milliseconds.

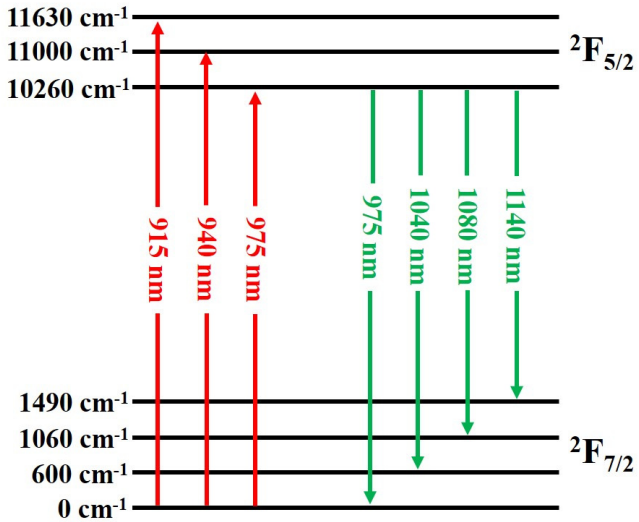

Figure 1.4: Two manifold energy level structure of Yb^{3+} with Stark levels.

The required amount of energy can be stored during this time, making the laser operation possible. This phenomenon is called population inversion, in which the number of atoms in the excited state is more than the number of atoms in the

ground state. When this condition is satisfied, the stimulated emission can take place [57]. It should be noted that this feature is a general property of the rare-earth elements, not just valid for the Yb element. It should be noted that this feature is a general property of the rare-earth elements, not just valid for the Yb element. Yb-doped fibers have a broadband gain spectrum compared to other rare-earth elements [58, 59]. They also have better conversion efficiencies compared to others [60–63]. In this respect, the Yb element is a good candidate for high-power laser operation.

1.1.2.1 Laser dynamics

As mentioned briefly above, the Yb element has an uncomplicated energy level structure. Ground, excited, and meta-stable states comprise the three-level laser structure of Yb-doped laser. Atoms are excited via two different pumping mechanisms: electrical and optical pumping [64]. The latter one is valid for the case of Yb-doped fibers. Photons with higher energy and lower brightness are used for pumping. The absorption mechanism, spontaneous and stimulated emission processes are governed by rate equations, which model the dynamics of the laser gain medium [65–67]. Ordinary differential equations establish the relationship between the intensity of photons and the charge carrier density.

$$\frac{dn_1}{dt} = -(R_{21} + W_{12})n_1 + (R_{21} + W_{21} + A_{21})n_2 \tag{1.7}$$

$$\frac{dn_2}{dt} = (R_{21} + W_{12})n_1 - (R_{21} + W_{21} + A_{21})n_2 \tag{1.8}$$

The population of the excited state increases with the absorption phenomenon of the pump energy as in the **Eqn. 1.7**. After a sufficient intense pumping, the upper-level population exceeds 50%, and thus the inversion population is reached. Therefore, the net gain is attained for the laser operation. Radiative and non-radiative transitions are two possible energy transfer methods between the energy

states. Radiative transitions result in an emission of a photon by spontaneous or stimulated emissions. The rate of these emissions is modeled by **Eqn. 1.8**.

$$n_2 = \frac{R_{21} + W_{12}}{R_{21} + R_{12}W_{12} + W_{21} + A_{21}} \tag{1.9}$$

$$n_1 = n_{total} - n_2 \tag{1.10}$$

n_1 and n_2 are the corresponding population levels of the ground and the excited states whereas n_{total} is the total number of Yb atoms inside the fiber, shown in **Eqn. 1.9** and **Eqn. 1.10**, respectively. R parameters are responsible for the pumping rates whereas the W parameter are responsible for the emission rates. σ^p and σ^s are absorption and emission cross-sections for pump and signal light, respectively. Additionally, I and ν stand for the intensity and the frequency of the pump and emission photons, respectively. Finally, A is the upper level lifetime as shown in the **Eqn. 1.11** and **Eqn. 1.12**.

$$R_{12} = \sigma_{12}^{(p)} \frac{I_p}{h\nu_p}, R_{21} = \sigma_{21}^{(p)} \frac{I_p}{h\nu_p} \tag{1.11}$$

$$W_{12} = \sigma_{12}^{(s)} \frac{I_s}{h\nu_s}, W_{21} = \sigma_{21}^{(s)} \frac{I_s}{h\nu_s}, A_{21} = \frac{1}{\tau} \tag{1.12}$$

1.1.2.2 Laser beam quality parameters

Yb-doped fibers have the lowest quantum defect, the difference between the pump and signal photon energies, compared to other rare-earth-doped fibers. Therefore, the maximum achievable slope efficiency is highest for Yb-doped fibers. This feature makes them a perfect candidate for the high-power laser operation.

$$Brightness \equiv B = \frac{P}{\lambda^2 (Q)^2} \tag{1.13}$$

After this brief introduction, I would like to emphasize another essential property of fiber lasers. They are called brightness converters since they enhance laser brightness. It is a crucial parameter for a laser system that severely affects the laser beam's ability to be focused directly related to the laser beam quality. The reason why is the semiconductor laser diodes have very low brightness due to their inherent structure. Therefore, there exists a massive demand for brightness enhancement. The brightness parameter is related to the power per unit area, wavelength, and quality factor (Q) of the laser as shown in **Eqn. 1.13**.

$$Q = M^2 = \frac{BPP_{(laser)}}{BPP_{(Gaussian)}} = \frac{w\Theta}{w_0\theta} \tag{1.14}$$

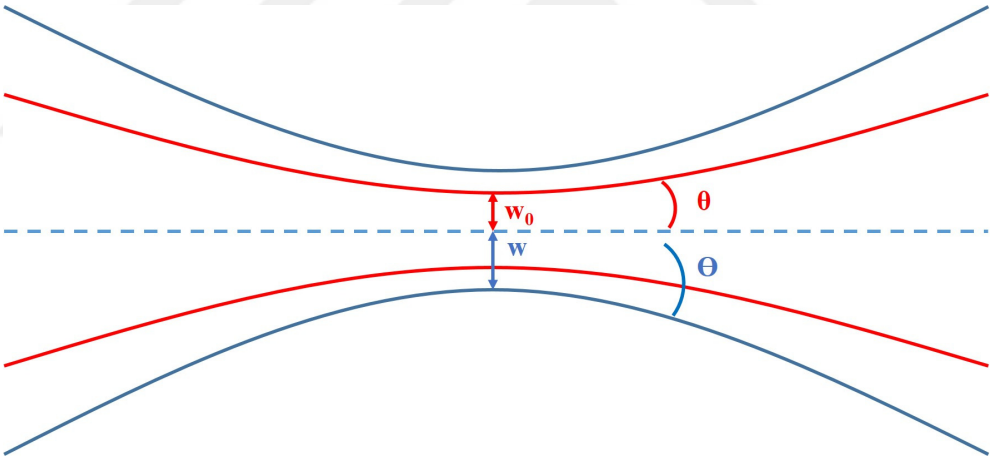

Figure 1.5: Beam radius versus z position of Gaussian and laser beams for comparison.

The beam quality of a laser beam, also known as M^2, is defined as the ratio of Beam parameter products (BPP) of a laser and the perfect Gaussian beam as shown in **Eqn. 1.14**. This number determines the focusability of the laser beam. Therefore, it affects the performance of the laser at long distances while operating special missions like material processing or as a laser weapon to destroy the specific target. The schematic illustration of a beam waist diameters of a Gaussian and a random laser beam with corresponding divergences has been shown in **Fig. 1.5**. Additionally, the beam waist diameter of a random laser beam while propagating along z-direction has been shown in **Eqn. 1.15**.

$$w_z^2 = w_0^2 \left(1 + (z - z_0)^2 \left(\frac{M^2\lambda}{\pi w_0^2}\right)^2\right) \tag{1.15}$$

1.1.3 Non-linear dynamics of continuous-wave HPFLs

High power fiber laser systems are promising and effective solutions for both industry and defense applications due to their extraordinary features, as mentioned before. However, several factors affect the performance of these systems called non-linear effects resulting from the inherent nature of the optical fibers themselves. These non-linear effects are Stimulated Raman Scattering (SRS), Stimulated Brillouin Scattering (SBS), and Transverse Mode Instability (TMI) [68–75]. All of these effects have a different impact on the performance of the laser systems. SRS limits the output power of the laser by transferring the energy to another frequency via the Stokes shift, also called the Raman shift. On the other hand, SBS does not limit the power scaling of the laser system but broadens the output optical spectrum, unfavored for some critical applications, such as the Coherent beam combination (CBC). Finally, TMI, rather a newly discovered phenomenon, directly affects the beam quality of the laser systems by deteriorating the output beam via the interference between the fundamental mode and higher modes of the fiber [76–78].

1.1.3.1 Stimulated Raman Scattering

Stimulated Raman Scattering (SRS) is a crucial non-linear process that can severely degrade a laser system's maximum output power level at a specific wavelength by switching the power to another wavelength by Stokes shift. This process was discovered in 1928 by Raman, known as the Raman effect [79]. It was also explored that it is a material-dependent effect that varies with the optical fiber's production material, such as for fused Silica, Raman gain g_R is around $\approx$ 1x10^{-13}m/W [80]. Briefly, the core composition of the fiber's core region plays a critical role in the Raman gain of the fiber. In addition to this, it should be noted

that the gain spectrum of the Fused Silica material extends over an extensive frequency range up to 40 THz, with a broad peak located near 13 THz [81]. The broadband frequency range is related to the non-crystalline structure of the fused silica material since amorphous materials; molecular vibrational frequencies form a continuum in the gain spectrum.

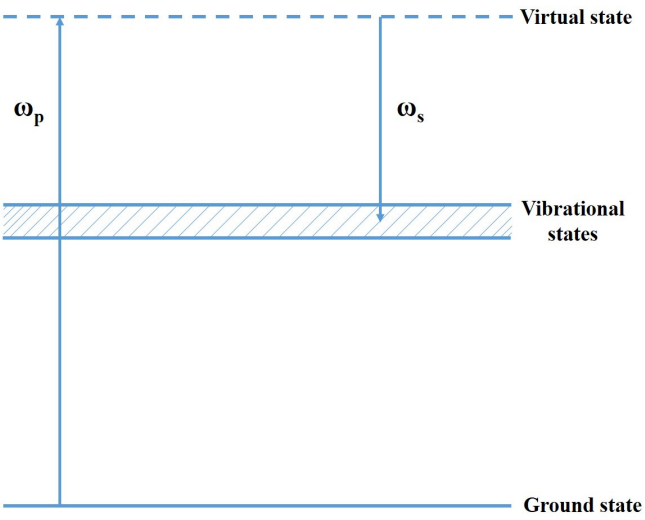

Figure 1.6: Schematic illustration of spontaneous Raman scattering.

Before stimulation, spontaneous Raman Scattering occurs, and after a certain pump power threshold, Stimulated Raman Scattering is excited. The working mechanism of spontaneous Raman scattering is the downshifting of the frequency by transferring the small amount of power from one optical field to another determined by the vibrational modes of the medium. The schematic illustration of spontaneous Raman scattering has been shown in **Fig. 1.6**. From a quantum mechanical perspective, a pump photon with an energy of $h\omega_p$ excites the molecule to a virtual state, and a photon with reduced energy of $h\omega_s$ is emitted spontaneously.

$$\frac{dI_s}{dz} = g_R I_p I_s - \alpha_s I_s \tag{1.16}$$

$$\frac{dI_p}{dz} = -\frac{\omega_p}{\omega_s} g_R I_p I_s - \alpha_p I_p \tag{1.17}$$

In a simple approach, the mathematical model of the SRS phenomenon would be governed by a set of coupled equations as shown in **Eqn. 1.16** and **Eqn. 1.17**. The parameters in the equations can be classified as the following: I_s is the Stokes intensity, I_p is the pump intensity, the Raman-gain coefficient g_R is related to the cross-section of spontaneous Raman scattering, and α_s and α_p are fiber losses at Stokes and pump frequencies, respectively.

$$\frac{d}{dz}\left(\frac{I_s}{\omega_s}+\frac{I_p}{\omega_p}\right)=0 \tag{1.18}$$

These two coupled equations can be simplified by ignoring the fiber losses, and thus these equations would turn into one simple equation as shown in **Eqn. 1.18**. This assumption states that the total number of photons in pump and Stokes beams remains constant during the SRS process. With the help of these equation sets, the pump power threshold for the SRS phenomenon by neglecting the pump power depletion, although it must be considered for the complete description of the SRS effect. After certain calculations with necessary assumptions, the critical power level of SRS can be found as shown in **Eqn. 1.19**. A_{eff} stands for the effective cross-section area of the fiber, and L_{eff} is the effective fiber length. In summary, the effective cross-section area of the fiber is directly related to the Raman threshold power, whereas the effective fiber length is inversely related. Therefore, this effect can be mitigated by increasing the diameter of the fiber and decreasing the optical fiber length.

$$P_{th}\approx\frac{16A_{eff}}{g_R L_{eff}} \tag{1.19}$$

For the sake of illustration, an example of optical spectrum during the high power laser operation based on the highly-doped LMA active fiber has been shown in **Fig. 1.7**. Since fiber length has been chosen as more than the optimum one 1^{st} and 2^{nd} Stokes have been appeared. Depending on the fiber length and the laser power more Stokes might arise in the spectrum.

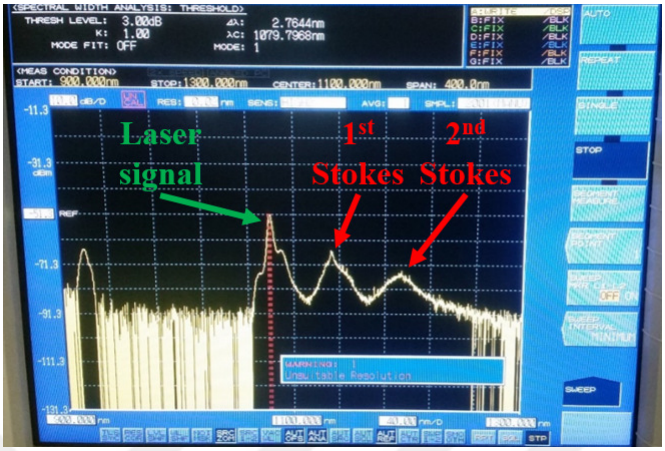

Figure 1.7: An optical spectrum example with Stokes emissions due to the SRS.

1.1.3.2 Stimulated Brillouin Scattering

Stimulated Brillouin Scattering (SBS) is another non-linear effect similar to SRS in working principle; however, SBS would be triggered at a lower power level than SRS. This non-linear process had first been discovered in 1964 [82]. Although there are similarities between the dynamics of the SRS and SBS effects, there is the main difference between them. The Stokes wave propagates in a backward direction in the case of SBS in an optical fiber. SBS can occur even at low power levels, and it is more related to the spectral behavior of the pump wave. All these differences between them are of interest with a fundamental change. The acoustic phonon interacts with the photons during the SBS effect, while optical phonons interact with the photons during the SRS effect. SBS is also a material-dependent effect and for fused Silica, Brillouin gain g_B is around $\approx$ 5x10^{-11}m/W [83]. Another difference between them is that the Brillouin gain spectrum lies within a narrower frequency range than the SRS effect.

$$-\frac{dI_s}{dz} = g_B I_p I_s - \alpha I_s \tag{1.20}$$

$$\frac{dI_p}{dz} = -g_B I_p I_s - \alpha I_p \tag{1.21}$$

Similar to the SRS case, there are two coupled equations governing the SBS effect as shown in **Eqn. 1.20** and **Eqn. 1.21**. In this case, there are two assumptions, which are $\omega_p \approx \omega_s$ and $\alpha_s \approx \alpha_p = \alpha$. That is the reason why these two coupled equations possess the current form. Afterward, similar to the case for the SRS effect, threshold power for the SBS effect can be calculated after certain steps as shown in **Eqn. 1.22**.

$$P_{th} \approx \frac{21 A_{eff}}{g_B L_{eff}} \tag{1.22}$$

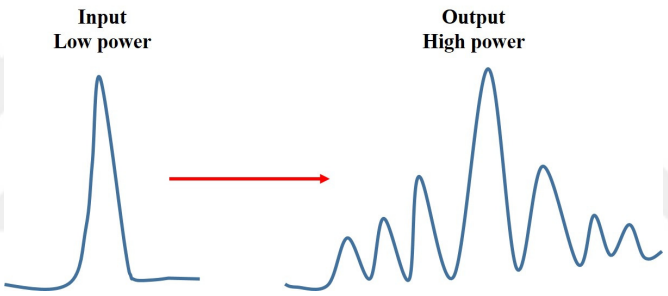

Figure 1.8: The change of the optical spectrum due to SPM.

$$n = n_0 + n_2 I \tag{1.23}$$

Another non-linear effect, Self-Phase Modulation (SPM), arises commonly in the single-mode fiber due to the Kerr effect, responsible for the non-linear change in the refractive index with the intensity as shown in **Eqn. 1.23**. SPM is mainly responsible for broadening the optical spectrum of the laser system as shown in **Fig. 1.8**.

1.1.3.3 Transverse Mode Instability

Since their invention, laser systems have been unavoidable due to the increase in their application areas. At first, they have been used for scientific purposes. Still, outstanding outcomes have been received within the technological developments after their implication in most industrial fields. The high performance of

laser systems in this field resulted in great demand for power-scale of these systems. However, this situation made fiber-based ones more favorable due to the extraordinary features of the fiber material, such as wave-guide structure and the capability to handle a considerable amount of power in a small area. Thus, all of the efforts have been focused on increasing the average power of the fiber laser systems. Eventually, several systems can handle multi kW diffraction-limited beams under a high thermal load, even without requiring any complex optical arrangements, unlike other competing solid-state laser technologies.

However, the everlasting demand of the industry for the scale of the high power laser system led to make some improvements in the design and architecture of both fiber itself and the whole system due to thermally induced non-linear effects [84]. Nowadays, the most popular one is Transverse Mode Instability (TMI), one of the current significant limitations for the power-scaling of high power fiber lasers systems. TMI causes deterioration of the beam quality of the laser system above a specific output power level. The history of this so-called effect is no longer than a decade, and the physics behind it is still under investigation worldwide [85, 86]. However, it has been widely accepted that the main reason for TMI onset is the thermo-optic non-linear coupling between the fundamental mode, LP_{01} and the first higher-order mode (HOM), LP_{11}. They interfere with each other so that the refractive index grating (RIG) object has been created due to the modal interference pattern (MIP) resulting from this modal interference. Then, this grating structure leads to the energy transfer between different modes, most likely the LP_{01} and LP_{11} in a repeating manner after reaching a certain threshold pump power level with the help of a relative phase of the fields.

The schematic illustration of this energy transfer between the LP_{01} and the LP_{11} has been shown in **Fig. 1.9** for the sake of visualization. There are specific theories upon the origin of this quasi non-linear effect, yet both are related to the refractive index change (RIC) in the core region of the fiber. Some claim that the population-inversion-induced RIC might be responsible for the TMI formation at low powers. It means that the difference between polarizability of excited and unexcited Yb^{3+} ions with a variation in the population of excited level $^2F_{7/2}$ of

Yb^{3+} ions results in a slight change in the refractive index of the fiber core region so that TMI is triggered indirectly [87, 88].

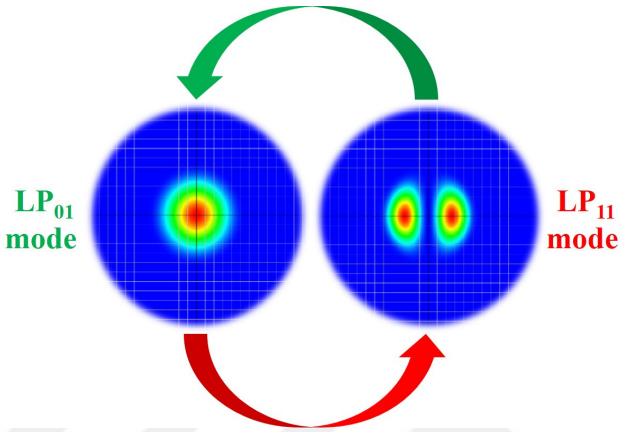

Figure 1.9: The schematic illustration of the energy transfer between the fundamental mode and the first higher order mode.

Another one states that inversion-induced RIC formation creates the RIG object, and this leads to the creation of the TMI effect [89]. On the other hand, most of the studies show that at high power levels, TMI is said to be predominantly driven by thermo-optical effects such as Stimulated Thermal Rayleigh Scattering (STRS) [90–96], thermal-lensing [97,98] and photo-darkening [99–102]. Primarily, STRS is attributed as the most related to the TMI effect concerning the origin of this effect. The simulation studies in these works have been governed based on the paraxial wave equation in cylindrical coordinates to mimic the optical fiber as a wave-guide as stated in **Eqn. 1.24**.

$$i\frac{\partial \Psi}{\partial z} = \frac{1}{2k}[\nabla_t^2 - k^2 + n(x,y)^2 k_0^2]\Psi \tag{1.24}$$

where Ψ the scalar field amplitude, k is a suitably chosen wave vector magnitude, ∇_t^2 is the transverse Laplacian operator, n(x,y) is the refractive index distribution along with the fiber, and $k_0 = 2\pi/\lambda$ the vacuum optical wave vector magnitude. Besides, the presence of TMI starts with the interference of more than one mode. Many studies have also been conducted as a simulation study via non-linear mode-coupling theory. The equations used to simulate this mode coupling between two modes are stated below in **Eqns. 1.25,1.26,1.27 and 1.28**.

$$\frac{\partial P_1^N}{\partial z} = -g_2 \chi e^{g_1 z} P_1^N(z) P_2^N(z) \tag{1.25}$$

$$\frac{\partial P_2^N}{\partial z} = g_1 \chi e^{g_2 z} P_1^N(z) P_2^N(z) \tag{1.26}$$

$$P_1^N(z) = P_1(z) e^{-g_1 z} \tag{1.27}$$

$$P_2^N(z) = P_2(z) e^{-g_2 z} \tag{1.28}$$

The power of the two modes are represented by $P_1(z)$ and $P_2(z)$ and the fiber amplifier gains are independent of propagation distance z, represented, respectively, by g_1 and g_2, the following coupled non-linear equations can be written for STRS power coupling between the two modes if the background loss is ignored [91].

After elaborating on the physical origin of this effect, some efforts have been made to mitigate this effect. Additionally, some solutions have been offered in the literature. First of all, these solutions are divided into two groups as passive and active mitigation strategies. Passive strategies for mitigating the TMI effect can be classified as fiber design, fiber core composition, quantum defect, gain saturation, and finally, pump wavelength and direction. In contrast, the active ones are dynamic mode excitation with an acousto-optic deflector, dynamic mode excitation with a photonic lantern, pump modulation, and finally phase-shift manipulation with seed bursts [85].

Chapter 2

Multi kW LMA Fiber Oscillator and Amplifier Systems

2.1 Introduction

High power fiber lasers (HPFLs) had a long journey while reaching the current situation with the development in rare-earth doping of the optical fibers. Historically, the amplification process had been first shown in 1964 with a 1 m Neodymium (Nd) doped fiber before Erbium (Er), and Ytterbium (Yb) doping [10]. This achievement was around the milliwatts range in the 1 μm wavelength region. After a few decades, the 1 μm emission has been attained in a milliwatts range power with a Yb-doped silica optical fiber. The oscillation and the amplification processes had been shown theoretically and experimentally [103–105]. Apart from Silica, Yb-doping has also been studied in other host glasses such as ZBLAN fluoride glasses [106]. The gain mechanism inside the laser cavity has been analyzed from many respects in Yb-doped fiber lasers at that time. Furthermore, the amplified spontaneous emission (ASE) process has also been observed, and detailed studies were performed to prevent possible problems due to this effect. For example, some critical parameters such as pump wavelength, fiber length, cavity design, and the doping concentration have been

optimized to scale the power of the HPFLs [107–109].

After a great effort, the power of the HPFL was scaled first to a few watts, this time with Yb-doped silica optical fibers. And then, it was scaled to beyond 100 W power level. Finally, 500 W and kW level HPFL systems would be achievable with new fiber designs in Master Oscillator Power Amplifier (MOPA) system [110–114]. The power scale trend of the HPFL systems exponentially increased up to a certain point with the development of each component in the fiber laser system. First of all, high power pump diode lasers are essential components to achieve high power laser operation. And this requires development in the semiconductor laser fabrication industry. Then, to combine the power of the individual diode bars, complex optical designs are needed in the pump diode lasers. Afterward, each pump diode laser should be combined with a high-power pump combiner to accumulate all the pump fiber in a single output fiber. Besides, for the production of the laser signal inside the cavity, high power fiber Bragg gratings (FBGs) are also crucial components for HPFL systems. The production of FBG also requires complex and expensive systems such as UV or femtosecond laser sources. And finally, the progress in the rare-earth-doped active fiber manufacturing technology made the HPFL systems possible. That is to say, it is like a chain mechanism in which each element depends on the other. Therefore, for progress, cumulative success is required.

In summary, the power scale of the HPFLs has become a reality within a few decades. It is because of the improvements in the fabrication of each laser component. Fiber-coupled high-power pump diode laser technology, combiner and FBG fabrication, and finally, Yb-doped active fiber manufacturing techniques have made outstanding advancements. On the other hand, this rapid progress brings with a shortcoming while the power increases. These are the non-linear effects that dramatically affect the performance of the laser systems. They will be mentioned in the following chapters, and some solutions will be offered.

2.2 High power fiber Laser systems based on commercial fibers

Based on the information mentioned in the previous section, I have studied the high-power fiber laser systems, mainly divided into two regarding architecture: oscillator and amplifier. In brief, laser oscillators, also called resonators, are the system where the laser signal is generated. On the other hand, the existing laser signal is amplified in the amplifier stage. Some systems contain both, called Master Oscillator Power Amplifier (MOPA). The master signal is produced and then boosted in the amplifier section simultaneously in a monolithic structure with the help of this configuration.

Briefly stated, fiber laser oscillator systems mainly consist of pump sources, pump combiner, and a piece of FBG mirrors to produce the signal with the feedback mechanism. One has high reflectivity, and the other has low reflectivity, also called output coupler. As the name suggests, generated laser signal exits the laser cavity from this port. Considering the high-power laser operation case, MOPA is more advantageous than the laser oscillator systems regarding the power and thermal burden. I also want to note that most of the laser systems mentioned in this thesis are based on the MOPA configuration. However, I have begun this study with a fiber laser oscillator system based on a Nufern branded commercial fiber.

On the other hand, the MOPA system includes both an oscillator and an amplifier stage to boost the signal power coming from the oscillator stage. Afterward, I built a MOPA system based on this commercial fiber beyond the 1.5 kW power level by adjusting the oscillator signal power. The optical spectra change has also been investigated in this study. Details will be given below.

2.2.1 HPFLs based on active LMA fiber

2.2.1.1 Pump-power limited 1 kW fiber laser oscillator system

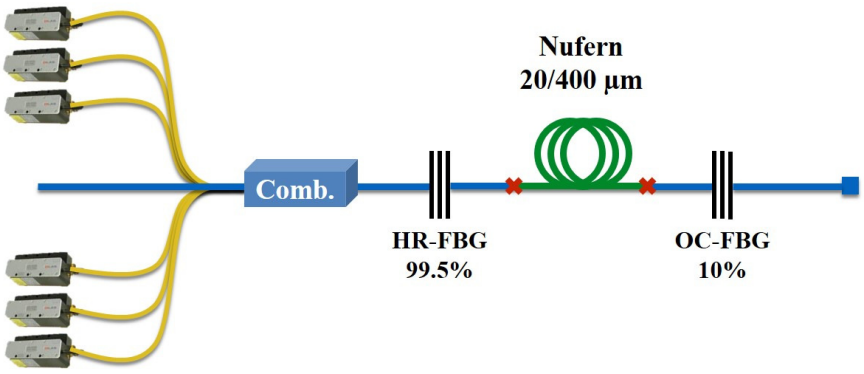

Figure 2.1: The schematic illustration of the 1 kW fiber oscillator system based on the Nufern fiber.

High power fiber oscillator system has been constructed, as briefly mentioned above. Six pieces of Dilas branded high-power pump diode laser has been utilized in this system. Each of them has a 250 W maximum output power capacity with a 976 nm central wavelength. They have been combined with a (6 + 1) x 1 pump combiner into one output signal fiber. Then, a piece of high-reflective and output-coupler FBG with 99.5% and 10% reflectivity, respectively, has been used to complete the laser cavity and produce the 1080 nm laser signal. On the other hand, the active medium, Nufern branded Yb-doped optical fiber, has 20 μm and 400 μm core and cladding diameters. The schematic illustration of the fiber laser oscillator system has been shown in **Fig. 2.1**.

Nufern fiber has a cladding absorption of 1.26 dB/m at 976 nm pump wavelength based on its data-sheet. The optimum fiber length is supposed to be chosen as 16 m for a total of 20 dB cladding absorption regarding this information. However, on the other hand, I have also performed a simulation to prove and support the accuracy of the selected fiber length. I have utilized the RP Fiber Power simulation tool for that purpose, which can simulate fiber laser and

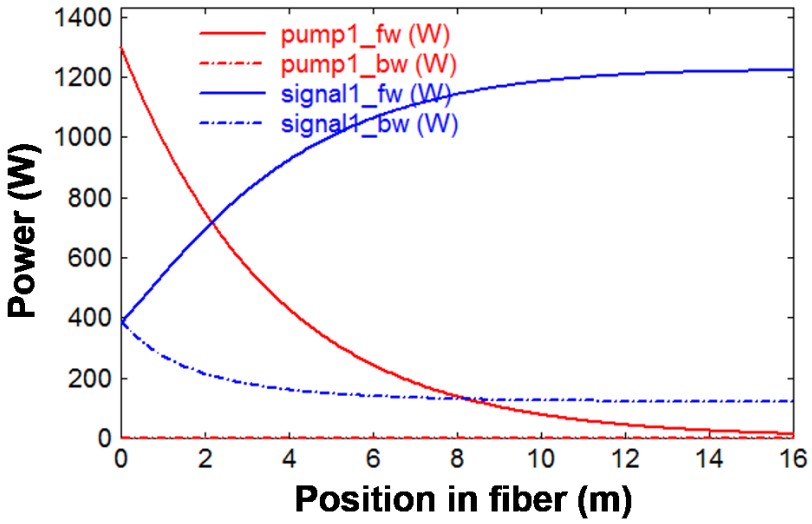

Figure 2.2: Simulation result of 16 m Nufern fiber under 1300 W pump power by RP Fiber Power simulation program.

amplifier systems both in CW and pulsed operation regimes. The temporal dynamics of the laser gain media has been governed by rate equations. However, for ultra-short pulses this software utilizes the popular approach of the split step Fourier method (SSFM) and also the non-linear Schrodinger equation (NLSE) to model the pulse propagation inside the optical fiber. In this case, the fiber laser system operates in CW regime. After the brief information about the software, I have entered the parameters of the fiber oscillator system as planned to be in the actual case, which are the reflectivity ratios of FBGs, pump power and wavelength, spectroscopic data of the active fiber, and the fiber length. The simulation result belonging to the 16 m Nufern fiber under 1300 W pump power has been shown in **Fig. 2.2**. According to the simulation result, signal_fw (forward signal) is 1220 W, and signal_bw (backward signal) is around 120 W. Thus, the output power of this fiber laser system is calculated as signal_fw - signal_bw = 1100 W for 16 m active fiber. Based on the simulation result given above, I have built the fiber laser oscillator system with 16 m-long Nufern fiber. After that, I have performed optical characterization of this system regarding the output power and the optical spectrum at maximum output power. First, I have plotted laser power versus launched pump power graph and obtained 1050 W laser power in return for 1325 W launched pump power.

The slope efficiency of this power characterization data corresponds to approximately 80%. The data belonging has been sketched in **Fig. 2.3a**. These numbers are so close to the simulated ones, although there is a slight difference between them. The possible reason for this situation is that the simulation program assumes that Yb ions absorb the whole launched pump power. On the contrary, some portion of the launched pump power cannot be absorbed by Yb ions and thus comes out with the signal power. This pump power is also called unabsorbed pump power in the laser literature. Additionally, I have taken the optical spectrum of the laser system at 1050 W maximum output power as shown in **Fig. 2.3b**.

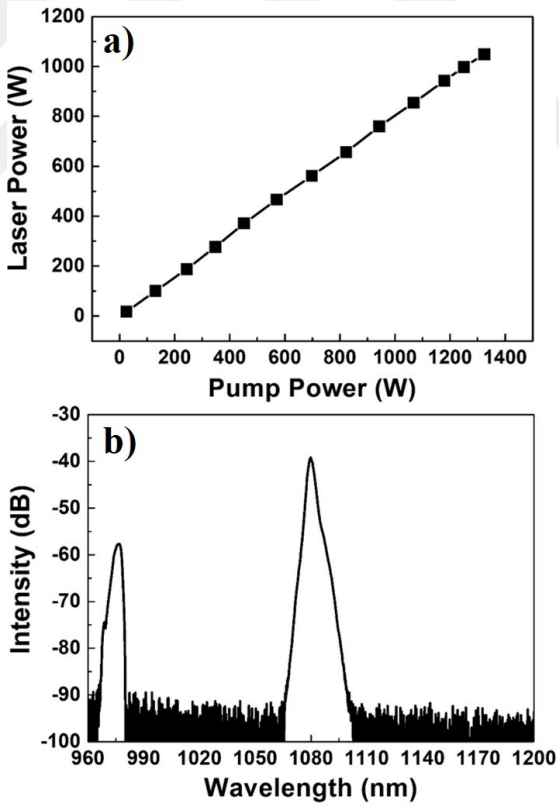

Figure 2.3: (a) The power characterization of the fiber laser oscillator system and (b) the optical spectrum taken at maximum output power level at logarithmic scale.

On the left-hand side of the optical spectrum, we see the 976 nm unabsorbed pump power and 1080 nm laser signal on the right-hand side. In addition, there is no sign of Stimulated Raman Scattering (SRS); however, I have not implemented

a Cladding Light Stripper (CLS) to remove the unabsorbed pump power in this system. Although there is no organic relation between them, SRS gain is directly related to the length of the laser system. Therefore, SRS would be more intense in the system with CLS since the total length increases. The implementation of the CLS will be performed in the subsequent studies.

2.2.1.2 1.65 kW fiber amplifier system

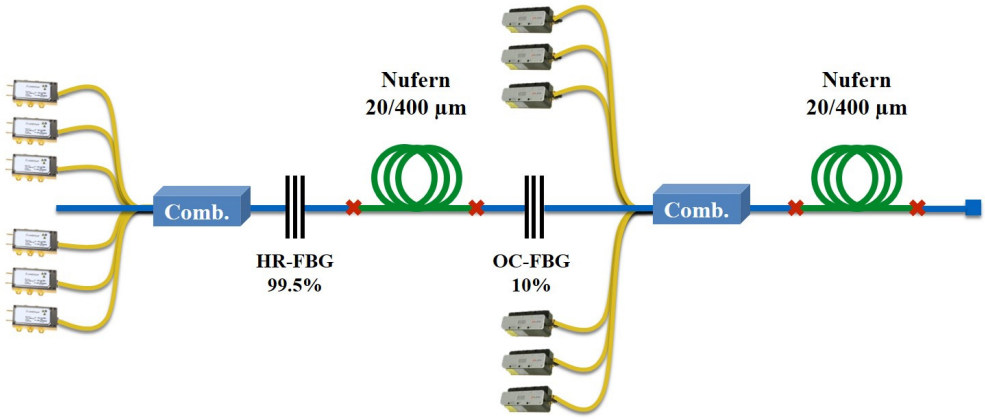

Figure 2.4: The schematic illustration of the MOPA system based on the Nufern fiber.

After completing the fiber oscillator system, I have built an amplifier system in MOPA configuration based on the Nufern fiber. For that purpose, I first built the oscillator part of the MOPA system utilizing 915 nm pump diodes, an FBG pair at 1080 nm, and 38 m Nufern active fiber. The fiber length is increased to 38 m from 16 m since the cladding absorption of the Nufern fiber at 915 nm pump wavelength is 0.45 dB/m. Therefore, total cladding absorption would be around 17 dB, fair enough to absorb the adequate pump power. Afterward, I assembled the MOPA system's amplifier stage with 976 nm high power diode lasers used in the fiber laser oscillator elaborated in the previous subsection. I have a special cylindrical apparatus fabricated for coiling and cooling down the active fiber for that purpose. I have intentionally decided the diameter of this fiber coiling apparatus as 10 cm to get rid of the HOMs inside the fiber since for an LMA fiber, it is close to the optimum bending value. But of course, it depends

on the fiber properties and may vary accordingly. The schematic illustration of the whole MOPA system based on the Nufern fiber has been shown in **Fig. 2.4** for the sake of visualization.

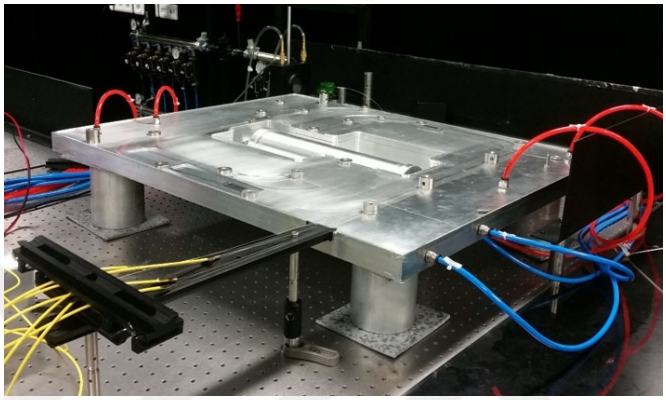

Figure 2.5: The picture of the amplifier part of the MOPA system with cylindrical apparatus to coil the fiber.

The picture of the aluminum cooling block fabricated for the amplifier art of the MOPA system has been shown in **Fig. 2.5**. Although the optimum fiber length has been simulated as in **Fig. 2.2** as 16 m for the oscillator system based on Nufern fiber, its length has been chosen as 18 m for the amplifier stage to sustain more pump absorption since this system also does not contain a CLS to remove the unwanted residual pump power.

Afterward, I have characterized the MOPA system in terms of power and optical spectrum. However, this time I have altered the seed signal power coming from the oscillator part of the system to observe its effect on the system's performance. Therefore, I have picked three different seed power, and then I have characterized the power of the MOPA system by increasing the pump power of the amplifier system. The output power increases linearly at all seed powers, as can be seen from **Fig. 2.6a**. However, I have observed that while seed power and the total output power increase, this linearity starts to degrade due to the thermo-optical effects. Therefore I did not go beyond that point not to harm the laser system. After the power characterization, I have also analyzed the optical spectra of each case, shown at once in **Fig. 2.6b**. From left to right, 915 nm unabsorbed pump light coming from the oscillator part, 976 nm unabsorbed pump

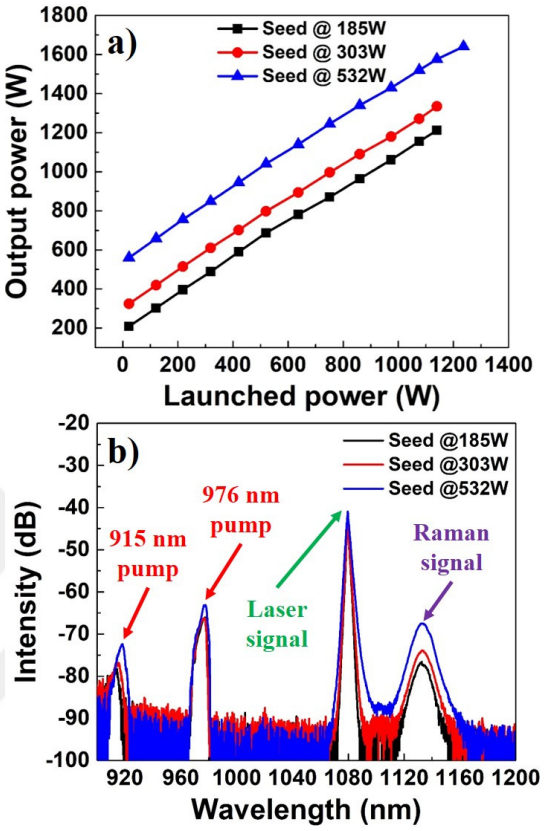

Figure 2.6: (a) Output power characterization and (b) corresponding optical spectra with different seed powers indicating the residual pumps, laser and Raman signals.

light coming from the amplifier part, 1080 nm laser signal, and 1140 nm SRS signal have been sorted. As shown in the figure, while the seed power increases, unabsorbed pump light intensity increases due to the lack of a CLS component. In addition to this, the SRS signal appears here, although it was not present in the fiber laser oscillator system. This reason is the total length of this MOPA system is longer than the fiber oscillator system explained in the previous section, and thus the SRS gain is much higher for this case. Another point is that the SRS signal has also been boosted with the seed laser power, as can be seen from **Fig. 2.6b**.

Finally, the amplifier system's thermal analysis has also been performed to detect the temperature on the fiber and the whole system. Therefore, I have taken a thermal camera image of the amplifier part of the MOPA system at

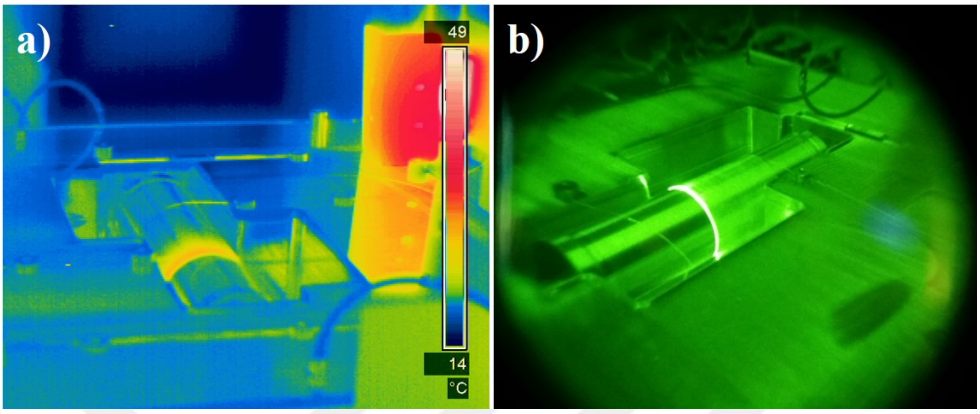

Figure 2.7: (a) Thermal and (b) infrared camera images of the amplifier part of the MOPA system at maximum power level

the maximum power level of the system as shown in **Fig. 2.7a**. It has been observed that the maximum temperature value does not exceed 40°C all over the system. Additionally, an infrared camera image has also been taken for the sake of visualization, as shown in **Fig. 2.7b**. The highest temperature value is recorded at the beginning of the active fiber since the thermal load is higher. At the same time, it also shines most because of the same reasoning in the infrared camera image.

2.2.2 HPFL system based on highly-doped active LMA fiber

2.2.2.1 2 kW fiber laser oscillator system

Besides the MOPA study, I have built a high-power fiber oscillator system based on a highly-doped LMA active fiber, whose product number is Liekki Yb1200-20/400DC. The maximum output power of this system has been planned to be around 2 kW level. First of all, to extract a 2 kW laser signal, at least 2.5 kW pump power is required depending on the fiber and the whole system's efficiency. Therefore, I have utilized 18 laser diodes with 140 W average power and 915 nm central wavelength for this configuration instead of 976 nm pump sources. The

reason for choosing this wavelength is related to the absorption cross-section of the Yb atoms, which have two dominant peaks at 915 nm and 975 nm. Although the absorption cross-section at the 976 nm pump regime is much more than the one at the 915 nm pump region; however, it is narrower than the 915 nm. The broadness of the absorption cross-section at the 915 nm pump region sustains the stable laser operation between the 905 nm and the 925 nm pump wavelength region [115]. The authors studied this situation in detail by building up 1018 nm fiber laser systems used for tandem pump applications. With supporting simulation studies, they have demonstrated experimentally that the 915 nm pumping region sustains stable laser operation covering a total of 20 °C changes in the pump diode's temperature. This feature facilitates the temperature stabilization of the system.

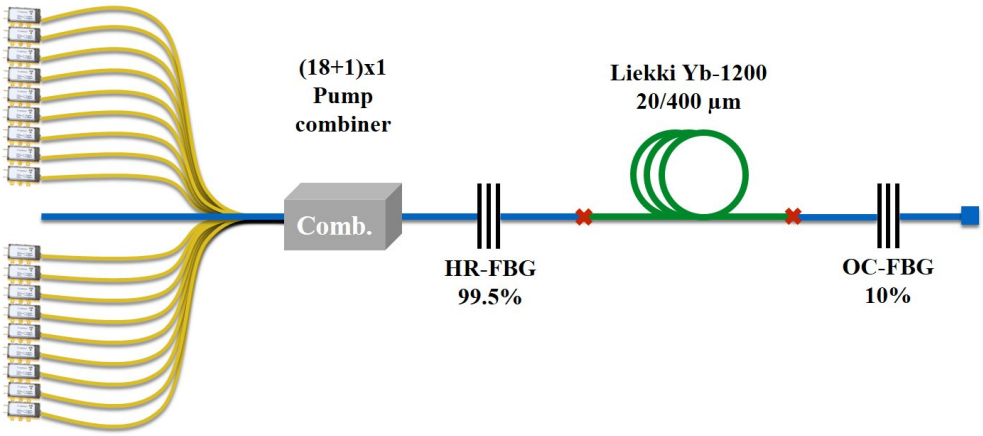

Figure 2.8: The schematic illustration of 2 kW fiber oscillator system based on Liekki fiber

On the contrary, it would be problematic for the 976 nm pumping scheme, especially for the defense applications in which the system is supposed to operate under extreme air conditions. Considering all this information, I have decided to use 915 nm as pump wavelength to control the system more efficiently. The only disadvantage of the 915 nm pumping scheme is that the absorption cross-section at 915 nm is approximately five times less than the 976 nm pumping scheme. Specifically speaking, for the active fiber I have used in this system, the absorption cross-section is around 0.6 dB/m at 915 nm and 3.0 dB/m at the 975 nm wavelength region. This situation brings along the need for the five times longer active fiber. 30 m long commercial highly-doped LMA active fiber with 20

μm and 400 μm core and cladding diameters, respectively, has been implemented for the total 18 dB pump absorption. The schematic illustration of the laser oscillator system is illustrated in **Fig. 2.8**.

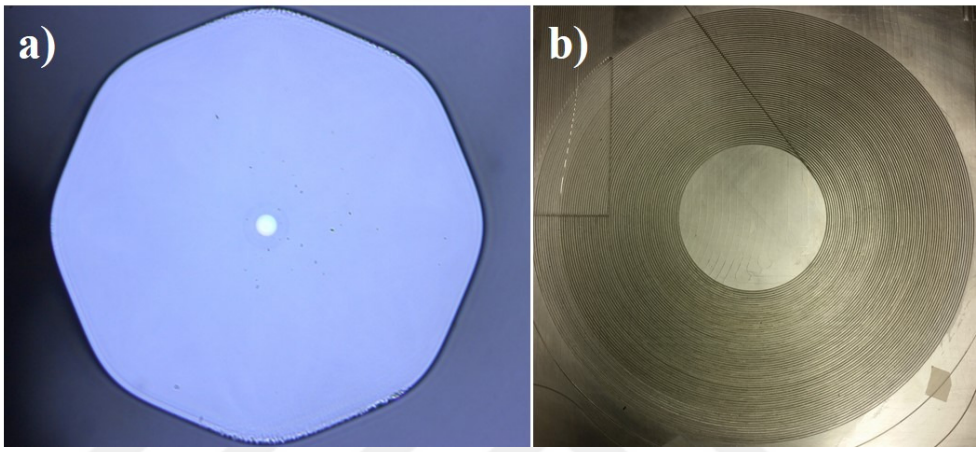

Figure 2.9: (a) Optical microscope image of the cross-section of Liekki Yb-1200 active fiber and (b) the image of specially designed cooling block in helix design

Eighteen pump diodes have been integrated with a pump combiner in (18x1)+1 configuration to gather approximately 2500 W pump power. One pair of high-power FBG mirrors working at 1080 nm central wavelength and having 99.5% (HR-FBG), and 10% (OC-FBG) reflectivity has been used in the laser cavity. Additionally, the fiber of the FBGs, having a numerical aperture (NA) of 0.07, was chosen to be suitable for the active fiber, with an NA of 0.07. As mentioned above, 30 m long active fiber has been implemented in this system, whose optical microscope image of the cross-section is illustrated in **Fig. 2.9a**. However, a special aluminum cooling block in a helix structure, starting from 30 cm diameter and ending at 10 cm diameter, has been designed and fabricated for coiling the active fiber. The motivation was both not to lose from the fundamental mode and to be able to fit these 30 m long active fiber to the system as shown in **Fig. 2.9b**. This varying diameter design is disadvantageous since the active fiber is an LMA fiber, supporting a few higher-order modes and the fundamental mode.

That is to say, to obtain high-quality laser light, higher-order modes have to be suppressed, and to do so, active fiber has to be coiled at a specific diameter. Generally speaking, for 20 μm core diameter LMA active fibers, the optimum

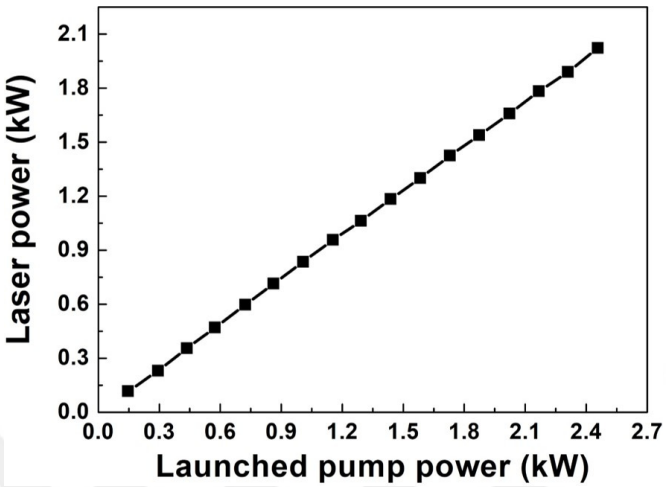

Figure 2.10: Output power characterization of the 2 kW fiber laser oscillator based on Liekki fiber

bending diameter is around 10 cm. However, in this case, for Liekki fiber, the optimum bending diameter is said to be 14 cm by the manufacturer. Based on the information given above, power characterization has been performed up to two kW, which is the system's maximum power level, as shown in **Fig. 2.10**. For that purpose, 18 pieces of pump diodes, each having 140 W average power, have been combined to obtain 2520 W total pump power. Consequently, this much pump power has been launched into the active fiber, and 2020 W output laser power has been attained from the output of the laser system. However, since the system doesn't include a CLS, the output power is the sum of the signal power and the unabsorbed pump power. Due to this situation, calculating the slope efficiency for this laser oscillator system does not make sense. Later on, a CLS will be implemented to the system, and the slope efficiency will be calculated accordingly by getting rid of the unabsorbed pump power.

After the power characterization, the optical spectrum image has been taken from 900 nm to 1200 nm spanning the 300 nm wavelength region at the maximum power level of the laser oscillator system. The unabsorbed pump power, laser signal, and the possible Raman signal are expected to be covered in this interval. The optical spectra have been taken both in logarithmic and linear scales to see the residue pump more apparently, as can be seen from **Fig. 2.11a** and **Fig. 2.11b**, respectively for comparison. Since there is no CLS component embedded

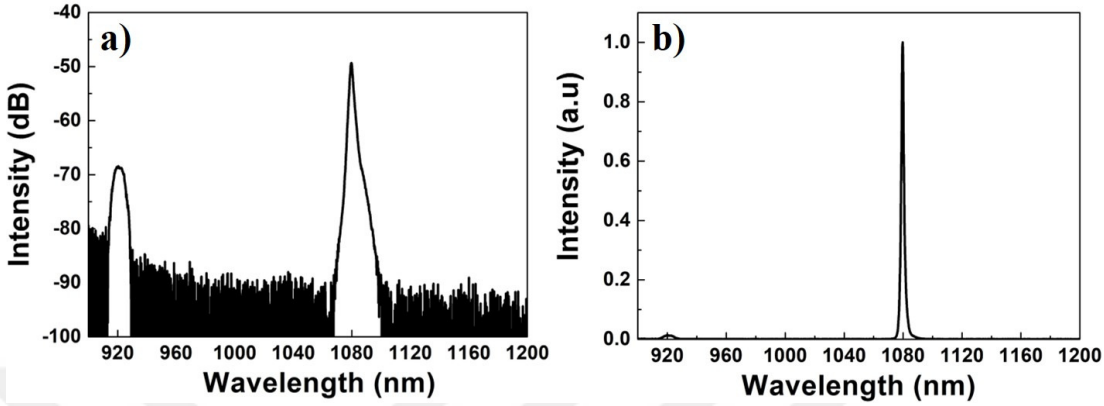

Figure 2.11: The optical spectra taken at maximum power of the fiber laser oscillator system (a) in logarithmic and (b) linear scale

in the system, a considerable amount of unabsorbed pump light has been obtained at the end of the system, as seen from the optical spectrum of the laser taken at the linear scale as shown in **Fig. 2.11b**. It could be added that an active fiber is capable of absorbing 90% of launched pump power at most, and thus 10% of will propagate and comes out along with laser signal if a CLS does not exist. This number may vary depending on the fiber properties specifically. Additionally, there is no sign for SRS signal; thus, this implies that the fiber length has been chosen correctly.

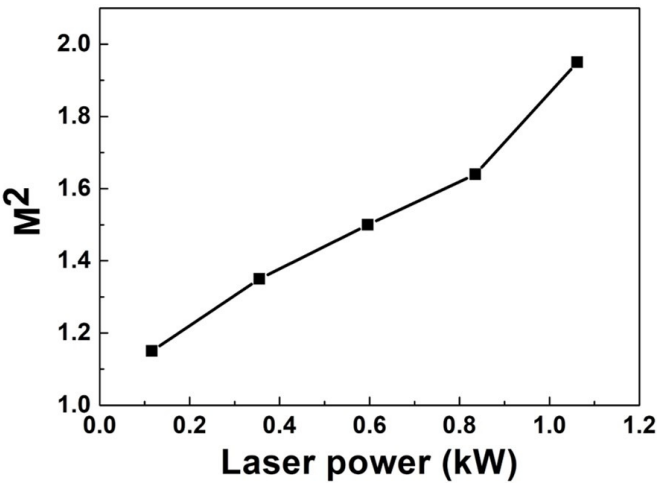

Figure 2.12: Beam quality measurement of the fiber laser oscillator above 1 kW power level

The last and essential feature that has to be considered is that the laser light's

(M^2) beam quality has also been measured up to 1 kW power level. The graph sketched based on the data taken from this measurement is illustrated in **Fig. 2.12**. For a laser system to be named a high-quality laser system, the M^2 value should be close to 1. At 100 W power level, the M^2 value is around 1.15, which is an excellent value for the beam quality parameter, as shown in **Fig. 2.12**. However, while the power keeps increasing, the M^2 value tends to increase accordingly. For a laser system, this situation is undesirable since the output beam profile of laser beam degrades with this increase. The most crucial reason for this beam-quality degradation is believed to be the TMI effect, a relatively new quasi-non-linear phenomenon. This effect will be investigated in the next chapters in detail.

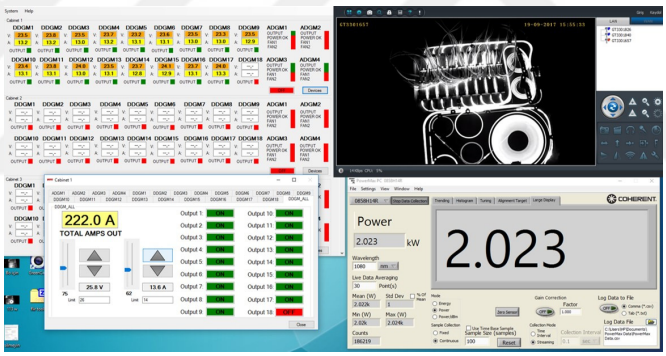

Figure 2.13: The image of the control panel including power monitor, a webcam and diode driver control unit

High power fiber laser systems require great attention during the operation in case of an emergency. They should be constantly monitored to detect any anomaly on the system. For that purpose, I have also built a control panel to monitor the output power, the system itself, and the laser diode driver unit simultaneously. I have combined these three control units with a computer screen, as shown in **Fig. 2.13**. Moreover, we see the software interface on the left-hand side, specially developed to control the applied current for each laser diode. Thermal analysis of the fiber laser systems is also a vital process to perform during the laser operation. Therefore, in addition to the webcam view, I have also monitored the thermal load on the whole system, including pump diodes, active fiber, splice points, and the other components in the system as shown in **Fig. 2.14**. The hottest point has been detected on the active fiber due to the

shortcoming of the cavity design. Nevertheless, the maximum temperature value does not exceed 50 °C at a 2 kW power level. Due to the lack of a CLS component, there is a considerable amount of unabsorbed pump power in the system. This unwanted residue pump power is needed to be removed from the system.

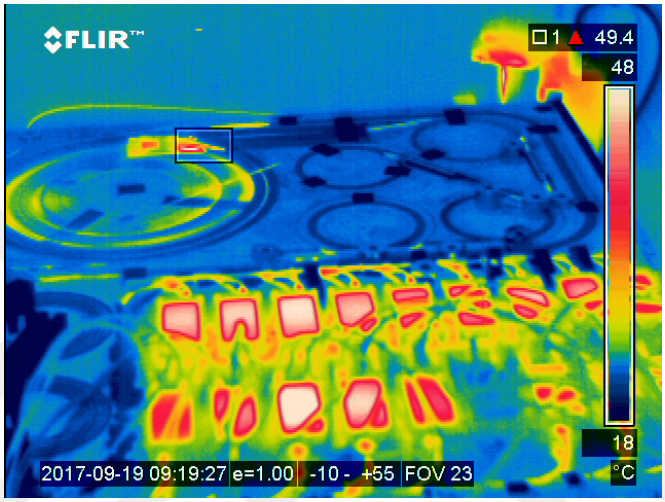

Figure 2.14: Thermal camera image of the fiber laser oscillator system at maximum power level

Cladding light stripper (CLS) is a crucial component for high-power fiber laser systems to remove the unwanted light sources out of the system effectively. The possible unwanted light sources can be classified as amplified spontaneous emission (ASE), residual pump light, and leakage to the cladding from the core due to the fusion splice mismatch between the fibers. When these unwanted light sources, especially the residual pump, cannot be removed from the system, the quality of the laser beam is affected severely. For that purpose, the fabrication of CLS has been investigated for years based on two main approaches. One of them is the etching method, in which the cladding region of the fiber is deformed for the light to escape [116–122]. The other one is the coating method in which the low index polymer of the fiber is removed, and the high index polymer is recoated on top of it [123–126]. The CLS formation based on the recoated polymer has a power scaling issue, whereas the other is more fragile since the fiber is deformed even though they are more capable of handling power. However, I have preferred the etching method since the total power we are dealing with is 2.5 kW.

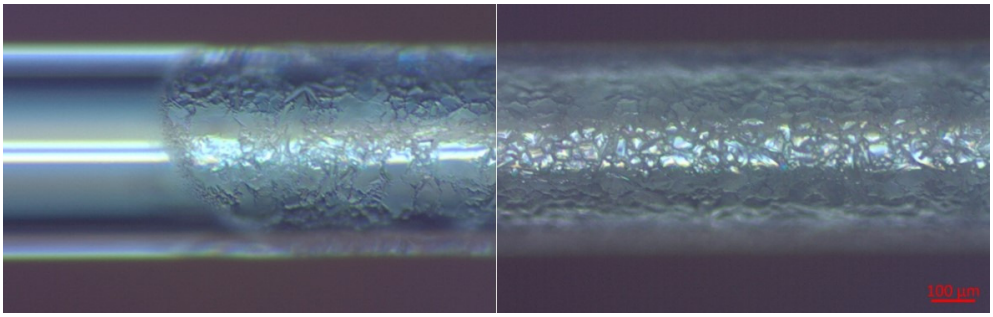

Figure 2.15: Optical microscope image of the side view of CLS component fabricated on passive Liekki fiber

For that purpose, I have used an etching cream and applied it to the surface of the fiber sample was subjected to this chemical etchant cream for half an hour. Then, it was cleaned carefully after this chemical process. The fiber sample was 20 cm long Liekki Passive 20/400DC, selected to prevent NA mismatch between the fibers. The optical microscope image of the fiber surface has been shown in **Fig. 2.15**. The fabrication of a CLS component has solved the unabsorbed pump power situation. However, I had faced another problem with this 2 kW fiber laser oscillator, which is the beam quality degradation problem.

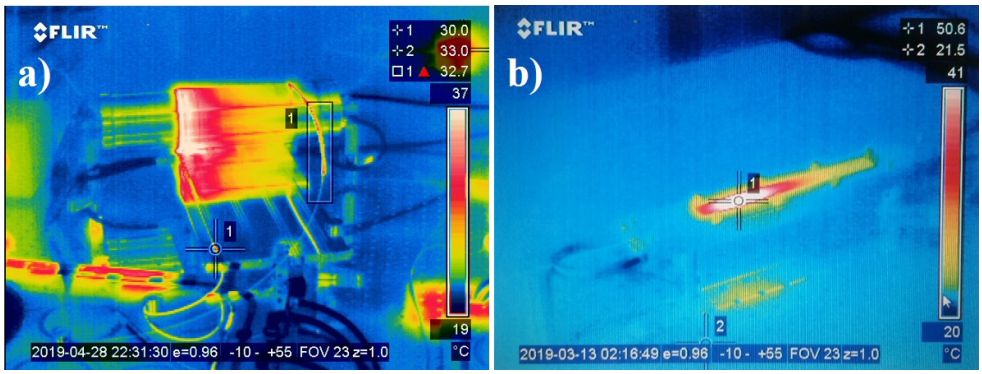

Figure 2.16: Thermal camera images of (a) the active fiber coiled in a cylindrical apparatus and (b) the cooling block of the CLS component at the maximum output power level

As a solution to this problem, I have also revised the cavity design of the fiber laser oscillator by changing the fiber coiling apparatus of the active fiber. I have implemented a cylindrical cooling apparatus with 10 cm diameter instead of the spiral one with varying diameters between 10 cm and 30 cm to eliminate the HOMs inside the fiber by bend-induced loss mechanism. To illustrate, I have

taken thermal camera images of both the active fiber and the cooling apparatus of the CLS component as shown in **Fig. 2.16**. The maximum temperature value on the active fiber has been recorded as 37°C at the maximum power level as shown in **Fig. 2.16a** and this reveals that the fiber has been cooled effectively in this system. On the other hand, the CLS component must also be cooled down to eliminate the heat from the unabsorbed pump power reaching the aluminum cooling block. The maximum temperature value that has been recorded for the CLS component is around 50°C, as shown in **Fig. 2.16b**, corresponding to approximately 300 W unabsorbed pump power.

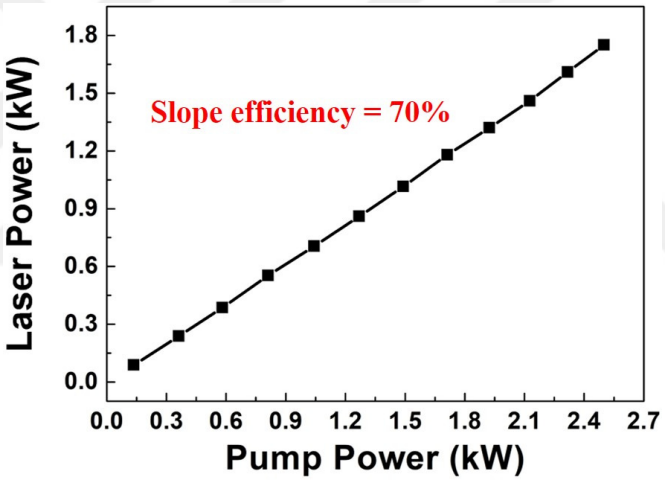

Figure 2.17: Power characterization of the revised fiber laser oscillator system up to 1.75 kW output power level with a CLS component

After coiling the active fiber at 10 cm bending diameter with a cylindrical apparatus, the revised fiber laser resonator system with a cladding light stripper (CLS) has been tested up to 1.75 kW output power level. The corresponding characterization result obtained has been shown in **Fig. 2.17**. The laser oscillator system has been pumped with 2.5 kW pump power; in return, 1.75 kW pure laser power has been obtained. The slope efficiency of the laser system has been calculated by dividing the pure laser power to the total pump power finding the slope efficiency as 70% indicated in the inset of the **Fig. 2.17**. To emphasize the existence of the CLS component in the fiber laser oscillator system, I have taken optical spectra at 1.75 kW power level both with and without the CLS component for comparison. Optical spectra data have been taken at both logarithmic and

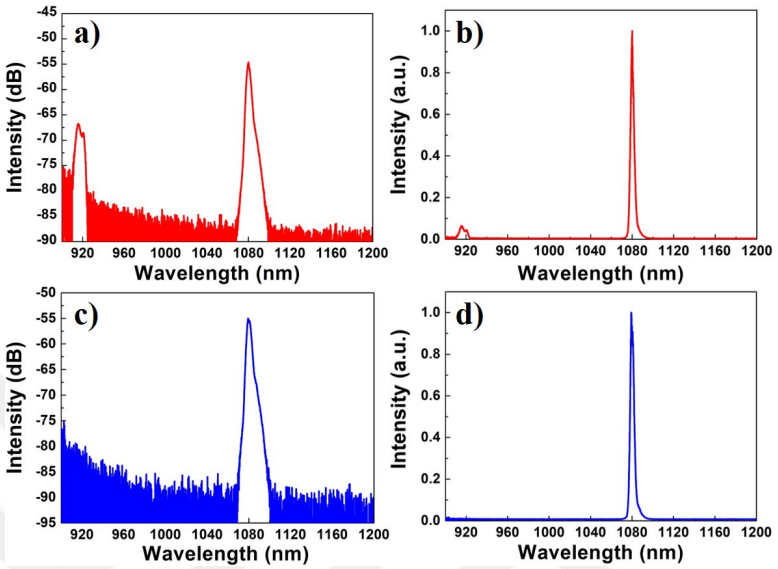

Figure 2.18: The optical spectra of the fiber laser oscillator system at 1.75 kW power level (a) at logarithmic, (b) linear scales without a CLS and at (c) logarithmic, (d) linear scales with a CLS

linear scales from 900 nm to 1200 nm spanning the 300 nm wavelength region as shown in **Fig. 2.18**. Specifically speaking, there exists a considerable amount of unabsorbed pump power, as can be seen from the **Fig. 2.18a** and **Fig. 2.18b** in logarithmic and linear scales, respectively, belonging to the laser system without the CLS case. After implementing it to the system, the optical spectra in both logarithmic and linear scales have been retaken, and the corresponding results have been shown in **Fig. 2.18c** and **Fig. 2.18d**, respectively. There is almost no residual pump left in the system, thanks to the CLS as expected. Moreover, Stimulated Raman Scattering (SRS) signal have not been observed during this characterization, implying that it has been suppressed effectively.

After the power characterization of the revised fiber oscillator system, the laser beam quality has also been measured up to maximum power level to investigate the effect of the cavity modification on the laser beam quality (M^2). The M^2 value had started with 1.2 and reached up to 2.1 at 1 kW power level in the previous case. However, I have not observed such an increase in this case. Thus it can quickly be concluded that by coiling the active fiber on a 10 cm diameter cylindrical apparatus HOMs have been successfully suppressed.

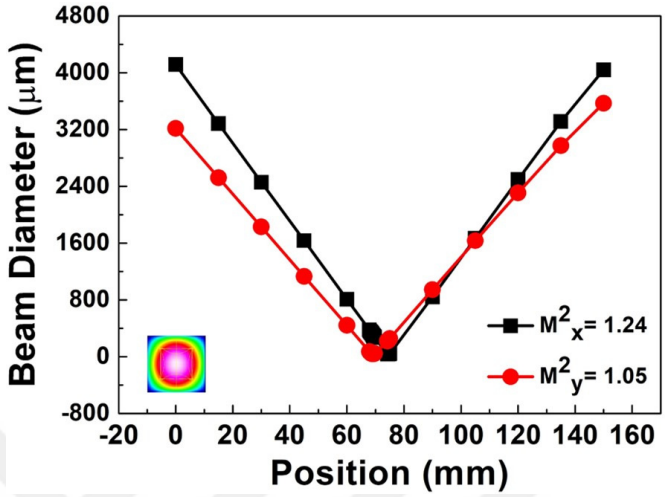

Figure 2.19: Beam quality (M^2) measurement result of the fiber laser oscillator system at 1.75 kW power level

As a result, the TMI effect has not been observed with this configuration. Thus, at the 1.75 kW power level, high-quality laser light has been obtained with M^2 values of 1.24 and 1.05 in x and y directions. The laser beam profile has also been shown in **Fig. 2.19** at the maximum power level of the system.

2.3 HPFLs based on home-made active LMA fibers

Apart from the high-power fiber laser system based on commercial fibers, I have also built fiber laser systems in MOPA configuration based on homemade self-fabricated Yb-doped active fibers. The sample fibers have been fabricated using the MCVD system with different doping concentrations for the main elements such as Ytterbium, Aluminum, and Phosphorus. All elements have different duties inside the matrix and have an impact on the fiber properties. I have altered the doping concentration of the so-called elements to observe this difference. After an intense work, I have fabricated two different 87# and 105# preforms with different Yb doping concentrations. First, the preform properties will be given, and then the optical characterization of the fibers will be explained below. Finally,

both fibers will be implemented into a MOPA system to see the high power performance. The detailed results will be shared belonging to these fibers in this chapter.

2.3.1 MOPA system based on 87# fiber

2.3.1.1 Preform properties

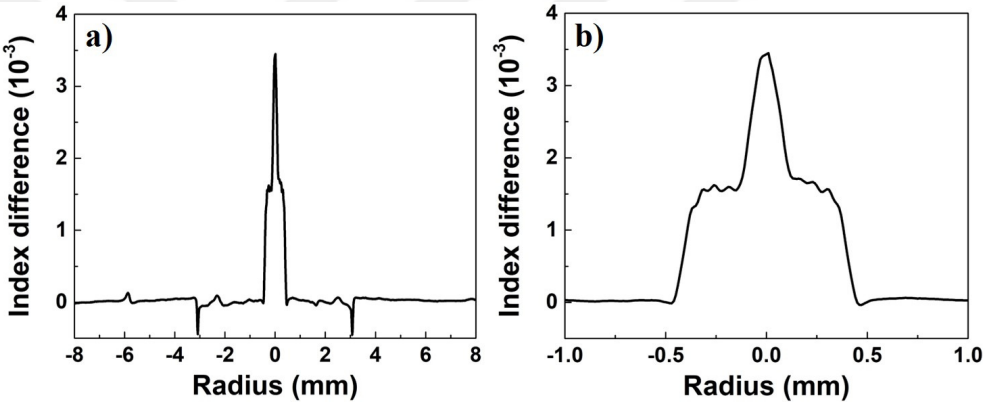

Figure 2.20: The refractive index profile (RIP) of (a) the whole 87# preform and (b) just the core region zoomed in.

As stated above, the preform fabrication has been performed with an MCVD system having a complex structure. The preform fabrication process will also be explained in more detail in the 3^{rd} chapter. But briefly, it starts with a Heraeus branded F300 quartz substrate tube whose inner diameter is 24 mm and the outer one is 28 mm, which was used for the deposition at 1930 °C via a H_2/O_2 torch. Then, the substrate tube was collapsed at 2050 °C by a furnace. Upon obtaining the preform, the core/clad ratio was adjusted by post-processes such as stretching and jacketing using the MCVD system. After the manufacturing process, the RIP of manufactured preform has been measured by the preform analyzer system, a P102 Photon Kinetics preform analyzer operating at 633 nm wavelength range. For that purpose, a preform slice with a thickness of less than 4 mm was used in this measurement. The sketched RIP data of the whole 87# preform with 17.2 mm diameter has been shown in **Fig. 2.20a**. Additionally, to

visualize better core region has been zoomed in as shown in **Fig. 2.20b**. The average index difference can be read as 1.6x10^{-3} from the graph corresponding to 0.068 preform NA. However, contrary to our intention, an undesired peak at the center of the preform's core region was created during the collapse pass of the preform manufacturing process.

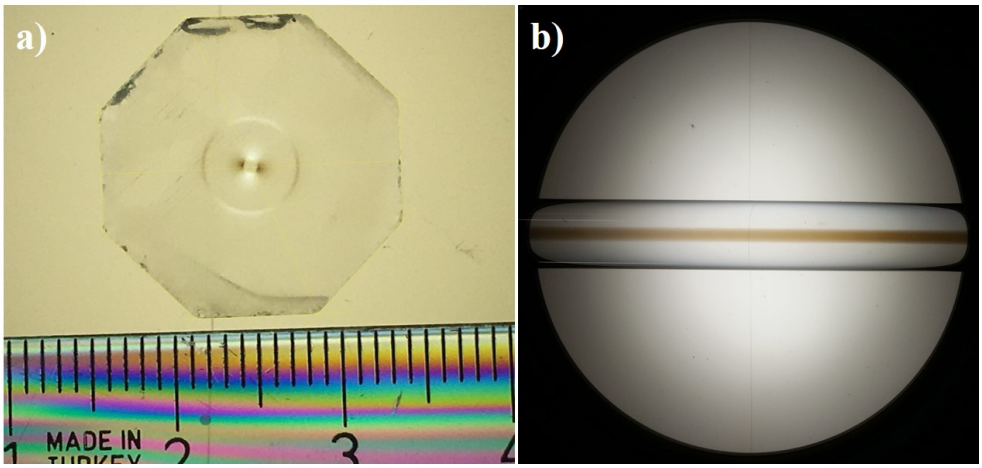

Figure 2.21: (a) The cross-section image a 87# preform slice after hexagonal cutting and (b) the polariscope image of the preform.

After the RIP measurement, the final preform has been checked using an Optacore POL-02 polariscope system to observe any discrepancies in the core region, which appears brownish by this system, and the homogeneity of the doping region can be visualized as shown in **Fig. 2.21b**. It could be noted that the core region appears darker with an increased Yb doping concentration, which will be realized in the next section by comparing the polariscope images of 87# and 105# preforms. The diameter of the magnifier of the polariscope is around 10 cm, and the total length of the preform is usually around 30 cm. Then the preform has been cut in hexagonal shape before the fiber draw as shown in **Fig. 2.21a** with a ruler showing the diameter as well. This cut is crucial for the fiber's centralization; otherwise, there is an offset between the fiber's core and cladding centers after the drawing. As a result, this offset causes an integration problem for the fiber to other fibers.

After the physical examination, the preform's elemental composition has been measured to observe the difference between the desired values and the actual

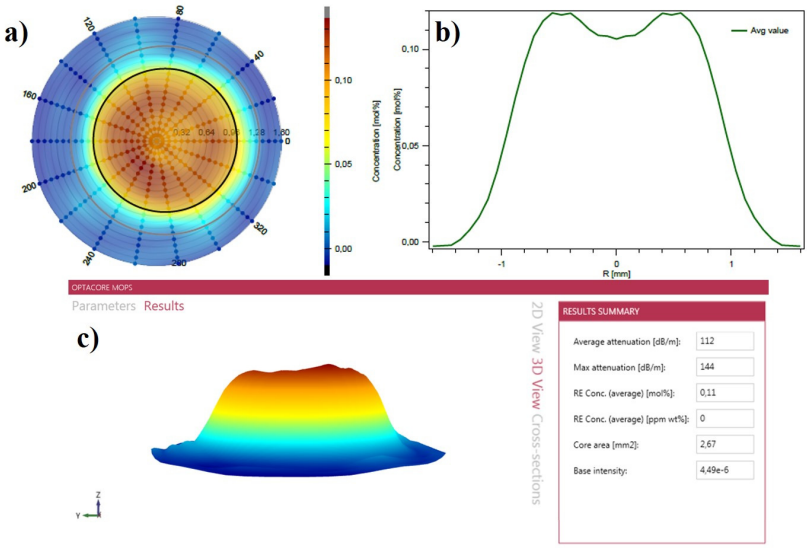

Figure 2.22: (a) MOPS image of the 87# preform in 2D and (b) the corresponding data sketched and (c) the 3D version

ones. Yb element has a priority in this measurement since it turns an optical fiber into an active fiber. For that purpose, a system with the same brand as the polariscope; Optacore came with the MCVD system to our fiber fabrication facility. First, I have measured the rare-earth doping concentration by this so-called system, the Optacore Measurement of Optical Preform Slice (MOPS) system. It has embedded software that enables us to map the Yb ion distribution in 2D and 3D; additionally, it sketches the graph belonging to the 2D mapping. Based on this explanation, the 2D image of the preform's core region has been shown in **Fig. 2.22a** and the corresponding graph has been sketched in **Fig. 2.22b** by the software. Additionally, it allows us to take an image of the 3D version of the Yb ion distribution mapping as shown in **Fig. 2.22c**. The average rare-earth concentration of this preform has been read as 0.11 mol% in the oxide version.

Finally, to detect the doping concentration of the other elements with the Yb itself, a more precise method, Wavelength-dispersive spectroscopy (WDS), attached to a Scanning electron microscope (SEM) system, has been applied. The reason for this situation is that MOPS can measure only the rare-earth element's doping concentration. Therefore, WDS is required to detect the whole elements' doping concentrations inside the matrix, Al_2O_3, P_2O_5 and Yb_2O_3 in

Table 2.1: Elemental compositions of the 87# preform.

Material		Mol% Oxide
Yb_2O_3	MOPS	0.11
	WDS	0.12
Al_2O_3		3.18
P_2O_5		1.4
Al/P		2.27
Excess		1.78 in Al_2O_3

this case. According to the WDS measurement, the doping concentrations are detected as 0.12 mol%, 3.18 mol% and 1.4 mol% for Yb_2O_3, Al_2O_3 and P_2O_5, respectively, as shown in **Table 2.1**. For this preform, Al_2O_3 has been doped more than P_2O_5 intentionally to decrease the Photodarkening effect. Also, MOPS and WDS results for the doping concentrations of the Yb_2O_3 are so close to each other. And, these two measurements are performed at the same time to support each other.

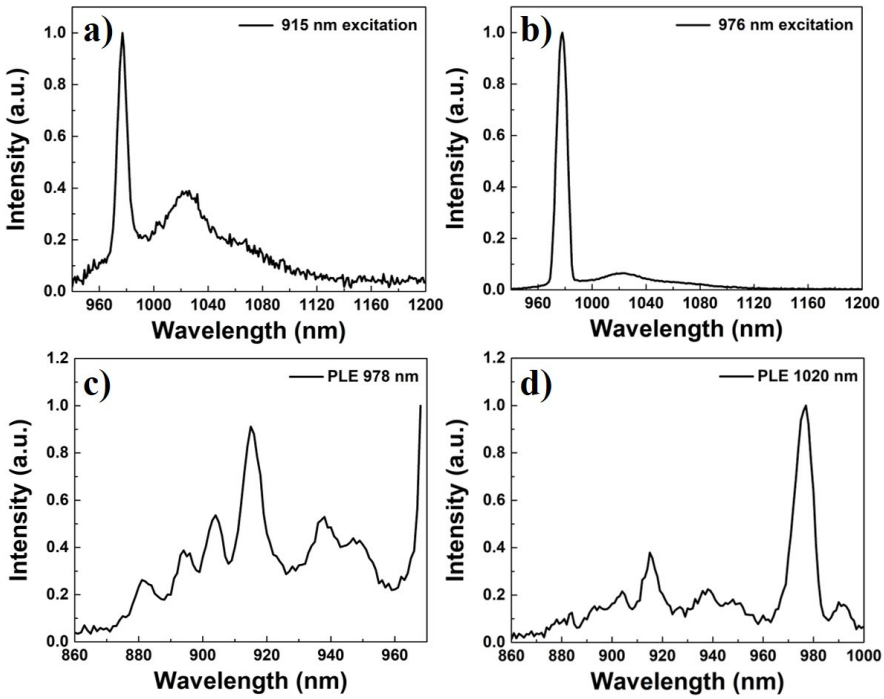

Figure 2.23: Photo-luminescence measurement of the preform a) at 915 nm and b) at 976 nm excitation, and PLE data c) for 978 nm and d) 1020 nm emissions.

After examining this preform's elemental composition and physical properties, the optical behaviors, namely the absorption and emission capability, have also been investigated. For that purpose, I have utilized a Time-Resolved Fluorescence (TRF) Spectrophotometry system. Knowing that the two most dominant absorption cross-sections of a Yb ion are around 915 and 976 nm, I have chosen them as the excitation wavelengths. Under 915 nm excitation wavelength, the dominant and narrower emission occurs around 976 nm, whereas the second and broader one is approximately 1025 nm wavelength region as sketched in **Fig. 2.23a**. On the other hand, under 976 nm excitation, I have obtained the emission peaks at 978 nm and 1024 nm wavelengths, respectively, as can be seen in **Fig. 2.23b**.

For comparison, the intensity difference between the emissions for the 976 nm and 915 nm excitations give a clue about the absorption cross-sections for these wavelengths. This data is consistent with the information given above, which is the absorption cross-section of Yb ion at 976 nm is larger than 915 nm. Additionally, I have also performed photo-luminescence excitation (PLE) measurements to investigate the possible pump wavelengths to obtain 978 nm and 1020 nm emissions by this preform as sketched in **Fig. 2.23c** and **Fig. 2.23d** respectively. The most dominant excitation wavelength peaks for 978 nm emission have been obtained as 976 nm, 915 nm, 904 nm, 938 nm, 947 nm, 894 nm, and 881 nm in descending order. Similarly, for 1020 nm emission, the most dominant excitation wavelengths are 977 nm, 915 nm, 939 nm, 904 nm, 990 nm, and 884 nm in descending order again. All of these emission and excitation wavelengths correspond to the required energies between the three levels of $^2F_{5/2}$ and the ground state of $^2F_{7/2}$ of Yb atom as discussed in chapter 1 of this thesis.

2.3.1.2 Fiber properties

The active fiber has been drawn out of the 87# preform fabricated by the MCVD system mentioned above. The manufactured home-built LMA active fiber has 21 μm and 416 μm core and cladding diameters, respectively, and the optical microscope image of the fiber's cross-section is shown in **Fig. 2.24**.

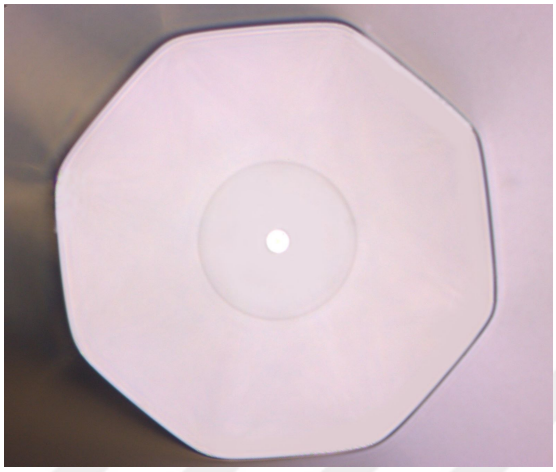

Figure 2.24: Optical microscope image of the 87# fiber's cross section.

Additionally, the numerical aperture (NA) of this fiber has been found experimentally as 0.052. On the other hand, the preform NA had been calculated as 0.068 based on the RIP data in the previous section. Fiber drawing might be the reason for this situation since the temperature rises to 2000 °C in the oven part of the fiber tower. Therefore, the material distribution might be altered since high temperature decreases the preform NA while passing to the fiber version. I have also analyzed the mode content of the fiber utilizing the RIP data of the preform since we can't measure the RIP of the fiber itself due to the lack of a measurement facility. To investigate the mode properties of this fiber, I have utilized the OptiFiber 2.2.0 version simulation program based on the RIP data of the preform as stated above.

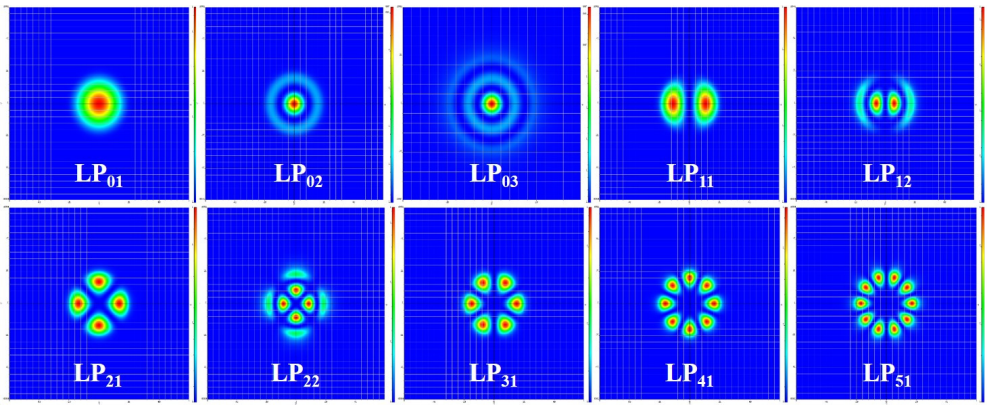

Figure 2.25: Simulation result of the 87# fiber's mode content based on the RIP data of the preform version.

The resultant mode distribution of this fiber contains LP_{01}, LP_{02}, LP_{03}, LP_{11}, LP_{12}, LP_{21}, LP_{22}, LP_{31}, LP_{41}, and LP_{51} as shown in **Fig. 2.25**. This fiber has 10 LP modes based on the 0.068 preform NA; however, the actual fiber has an NA of 0.052. Therefore, it can easily be concluded that the number of modes that this fiber supports should be lower than 10. Moreover, it can be estimated based on the ratio of the preform and the fiber NA values using the equation below:

$$Mode\# \approx \frac{V^2}{2} \tag{2.1}$$

Since the V number is directly related to the NA, it can also be related to the mode number with its square. By a simple calculation, the estimated mode number of the 87# fiber would be 6 instead of 10.

2.3.1.3 Laser characterization

A setup has been constructed in a MOPA configuration which consists of an oscillator and amplifier part to test the active fiber's high power performance. MOPA system has not been sketched this time due to the resemblance of the **Fig. 2.5**. The only difference is that I have used three pieces of high power pump diode module in the oscillator stage of this system, operating at 976 nm central wavelength. Then, the remaining three pump ports have been dumped with the help of an aluminum block. The oscillator stage has been designed to operate at a power level of 100 W, although it has a higher power capacity since it will be enough to more than 1 kW output power level. In the amplifier stage, on the other hand, I have used six pieces of high power pump diode modules, the same as the ones in the oscillator stage, which again operate at a 976 nm central wavelength. They have been combined with the same (6x1)+1 pump combiner, and the output signal port of the combiner has been spliced to the 87# active fiber. The doping concentration of the active fiber is slightly lower than the commercial ones; therefore, the length of the fiber that I have to use for effective absorption is a bit longer. Therefore, the length of the fiber has been chosen as 37 m, and it has been coiled at 10 cm diameter. As explained in

the previous section, I have also implemented the same CLS component, which can handle hundreds of watt pump power and 1 kW signal power. With the help of our group members, I have succeeded in producing this CLS benefiting from chemical methods, and I have tested its performance. The CLS was able to suppress approximately 340 W pump power at a 23 dB extinction ratio. After these successful tests, I implemented the CLS to the 1 kW MOPA system and integrated it to the active fiber to eliminate the unwanted unabsorbed residue pump light. QBH cable consisting of an endcap and a quartz blockhead inside has been integrated into the CLS output.

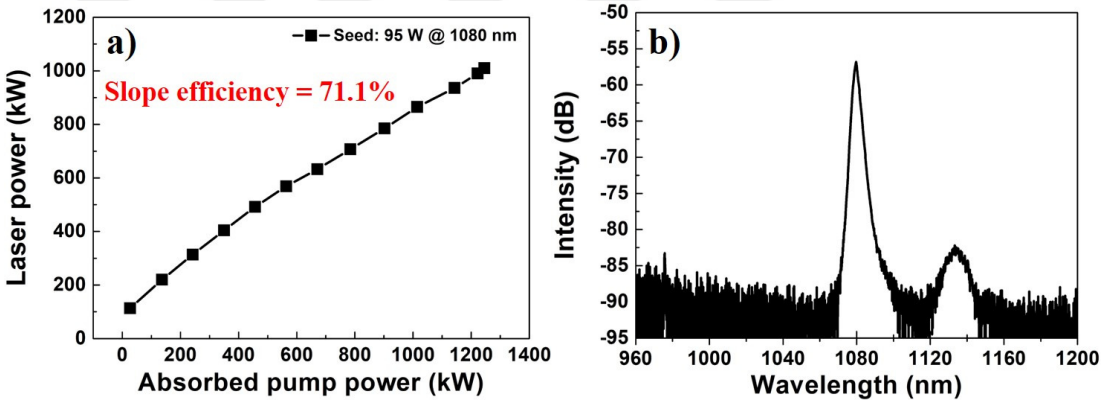

Figure 2.26: (a) Output power characterization of the MOPA system based on 87# fiber up to 1 kW power level and (b) the optical spectrum taken at maximum power level.

After integrating the QBH cable, the laser system is ready for any specific application, such as material processing. After completing the construction of the whole MOPA system, while the seed signal power is around 95 W, the system has been characterized up to 1 kW power level, which is the maximum power level of this system. The power characterization result of the MOPA system based on the 87# fiber has been shown in **Fig. 2.26a**. the slope efficiency of this graph has been calculated as 71.1% by Origin Pro 2015 software with linear fitting. This number can be verified by assuming that an active fiber can utmost absorb 90% of the launched pump power regardless of its length. I have implemented more than enough fiber in the system, and thus I also can assume that 37 m long active fiber has absorbed 90% of the launched pump power.

Knowing that the total launched pump power is 1440 W, and thus the absorbed pump power can be calculated as 1290 W. The output power from the system has been recorded as 1010 W, including a 95 W seed signal, which should be abstracted from the total power to calculate the slope efficiency of the system, which can be calculated as 71% by dividing the amplified pure laser power to the absorbed pump power. This number is close to the one calculated by the software, proving that the fiber length has been chosen effectively. After the characterization of the power capacity of the fiber amplifier system, an optical spectrum has been taken in logarithmic scale as shown in **Fig. 2.26b**.

Since a CLS has been implemented in this system, residual unabsorbed pump power has been decreased substantially compared to a system without a CLS. Moreover, the residual pump power suppression is around 30 dB according to the logarithmic scale; additionally, there is a Raman signal due to the SRS, yet with more than 25 dB suppression in the logarithmic scale as well.

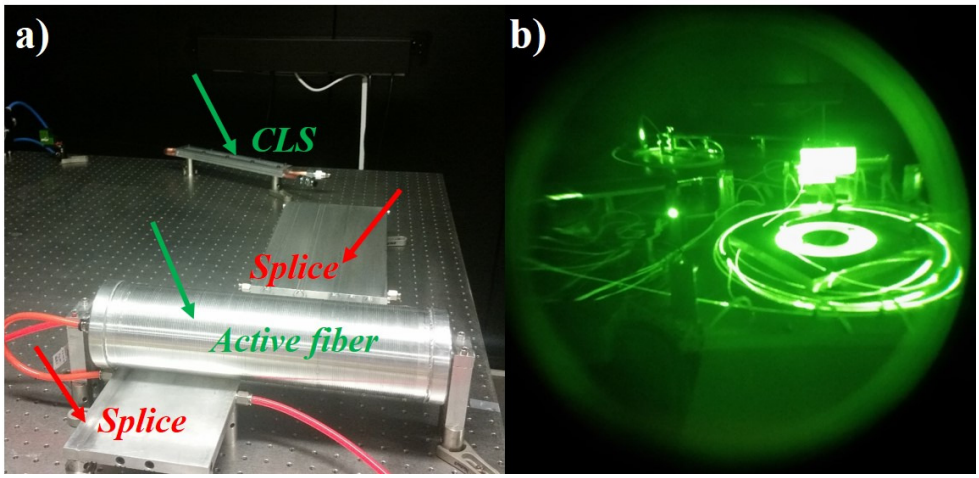

Figure 2.27: (a) The image of the amplifier part of the MOPA system indicating the splice points, active fiber and the CLS and (b) the infrared camera image of the whole system while operating.

Afterward, I took a photograph of the amplifier system, including the active fiber, splice points, and the CLS component inside a cooling plate as shown in **Fig. 2.27a**. In addition to this, an infrared camera image of the whole system while working relatively at low power has been taken just to visualize the system, as shown in **Fig. 2.27b**. I have mentioned the CLS component fabrication

method in the previous section, fabricated on a Liekki Passive-20/400DC fiber with a chemical process. Thus, the fiber's surface would have a certain roughness, which breaks the total internal reflection (TIR) rule. Therefore, the light cannot pass through the cladding at this CLS region and be expelled from the fiber. For the sake of visualization of the CLS region, an infrared camera image has been taken while operating at low power, as shown in **Fig. 2.28a**. After that, the high power performance of the CLS also has been tested under the 1 kW power burden. The thermal camera image was shown as in **Fig. 2.28b**, and as can be seen from the figure, the highest temperature does not exceed 55 °C.

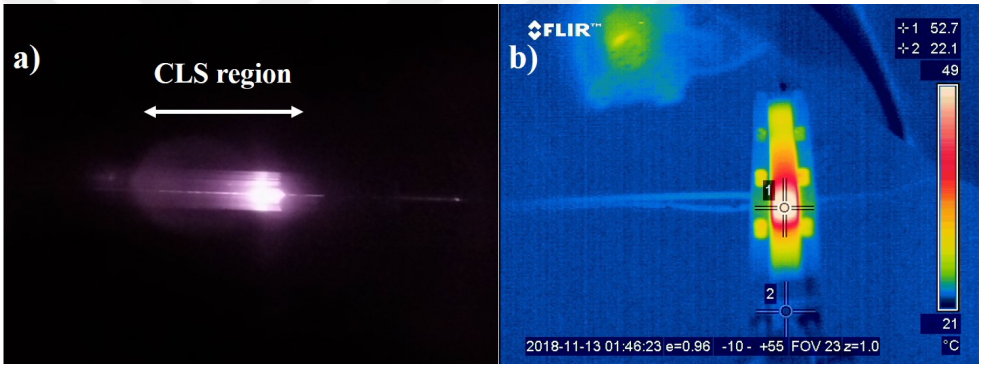

Figure 2.28: (a) Infrared camera image of the CLS component taken while operating at a low power level b) and thermal camera image taken at the maximum power level.

2.3.2 MOPA System based on 105# Fiber

In the previous section, 87# self-fabricated active fiber had been examined in detail. It has been tested up to 1 kW power level in a MOPA configuration implementing 37 m long active fiber in the amplifier stage to sustain adequate pump absorption. The pump wavelength selected for this system was 976 nm, and so the absorption cross-section of this fiber would be experimentally around 0.6 dB/m for the 976 nm pump wavelength. Compared to active commercial fibers with absorption cross-sections around 1.2 dB/m, the Yb doping concentration of the 87# active fiber was lower than the commercial ones. Besides, the numerical aperture of the 87# active fiber is around 0.05, while the commercial ones are in the 0.06 and 0.07 range. Therefore, two parameters need to be enhanced to

obtain such an active fiber similar to the commercial ones. For that purpose, a new 105# fiber preform has been manufactured hoping to have a higher Yb doping concentration and a numerical aperture.

2.3.2.1 Preform properties

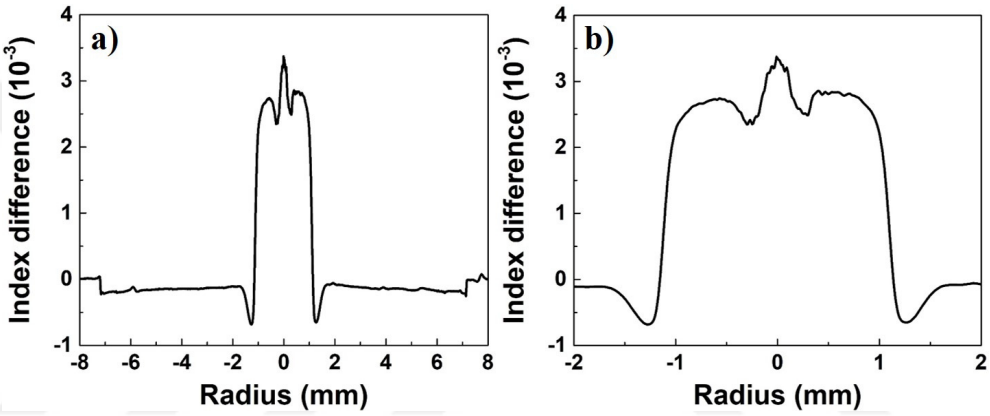

Figure 2.29: Refractive index profile of(a) the whole 105# preform and b) just the core region zoomed in.

As mentioned in the previous section, it has been aimed to manufacture a revised preform with enhanced Yb doping concentration compared to 87# preform to achieve an NA of 0.06 or greater. For that purpose, a new recipe has been created with greater Yb_2O_3 decreasing the concentration of Al_2O_3 to balance the NA of the fiber to attain the desired value. The refractive index profile of the whole stretched preform has been shown in **Fig. 2.29a**and the zoom in version has also been shown in **Fig. 2.29b** for better visualization of the core region. The average refractive index difference has been measured as 0.0027, corresponding to a 0.089 preform NA.

Besides this intentional increase, the RIP distribution has also been engineered more homogeneously than the previous one, 87# fiber preform. After that, this fiber preform was analyzed under the Optacore POL-2 polariscope system, whose photograph has been shown in **Fig. 2.30a** to observe the possible defects on the preform's core region. Additionally, the polariscope image of the 10-cm segment of the preform has been shown in **Fig. 2.30b** without any defect inside. The

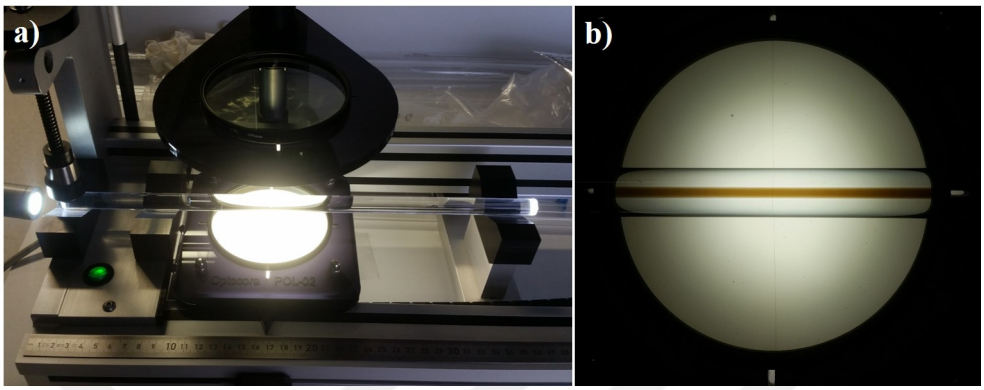

Figure 2.30: (a) Optacore POL-02 polariscope system and b) the polariscope image of the 105# preform.

polariscope system provides a piece of comparative information about the Yb doping concentration for the preforms.

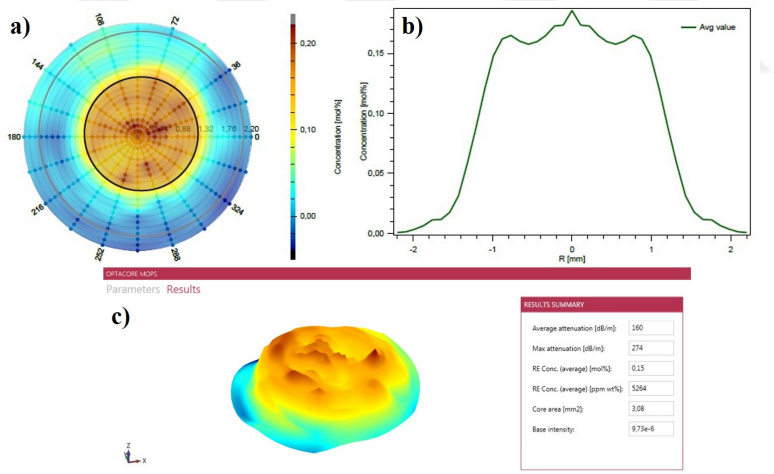

Figure 2.31: a) MOPS image of the 105# preform in 2D and (b) the corresponding data sketched and (c) the 3D version

As in this case, the 105# preform's core region appears darker compared to the one of 87# preform (**Fig. 2.21b**). In this context, this analysis system confirms the increase in the doping concentration of this preform. After polariscope analysis of the preform, I have performed elemental composition measurement utilizing the MOPS system embedded in the MCVD as elaborated in the previous sections. Before the measurement, the sample needs to be sandpapered to

attain an accurate result. MOPS are capable of extracting both 2D and 3D mapping of the preform. Additionally, the software comes out with the concentration (mol%) vs. radius (mm) plot in 2D. Eventually, I have also obtained a 2D image of the preform sample as shown in **Fig. 2.31a** and the corresponding concentration plot as in **Fig. 2.31b**. According to this plot, the 105# preform's average Yb doping concentration has been attained as 0.15 mol% by the MOPS measurement. Consequently, the MOPS data resembles the RIP analysis due to the high-quality grinding of the preform sample, as can easily be realized. Moreover, the 3D elemental mapping of the preform has also been shown in **Fig. 2.31c**.

Table 2.2: Elemental compositions of the 105# preform.

Material		**Mol% Oxide**
Yb_2O_3	MOPS	0.15
	WDS	0.16
Al_2O_3		2.65
P_2O_5		1.43
Al/P		1.85
Excess		1.45 in Al_2O_3

As a summary, the elemental composition of this preform has been tabulated as in **Table 2.2**. The MOPS and WDS data belonging to the Yb element have been given for comparison. Besides, other materials such as Al_2O_3, P_2O_5 and their elemental composition ratio have also been given thanks to the WDS measurement. The doping concentrations are detected as 0.16 mol%, 2.65 mol% and 1.43 mol% for Yb_2O_3, Al_2O_3 and P_2O_5, respectively. In this case, the Al_2O_3's doping concentration has been lowered while the one for Yb_2O_3 increased to achieve the desired preform NA.

After examining this preform's elemental composition and physical properties, the absorption and emission capability have also been investigated utilizing a Time-Resolved Fluorescence (TRF) Spectrophotometry system. The two most dominant absorption cross-sections of the Yb ion are 915 nm and 976 nm. Under 915 nm excitation wavelength, the dominant and narrower emission occurs around 976 nm, whereas the second and broader one is approximately 1030 nm

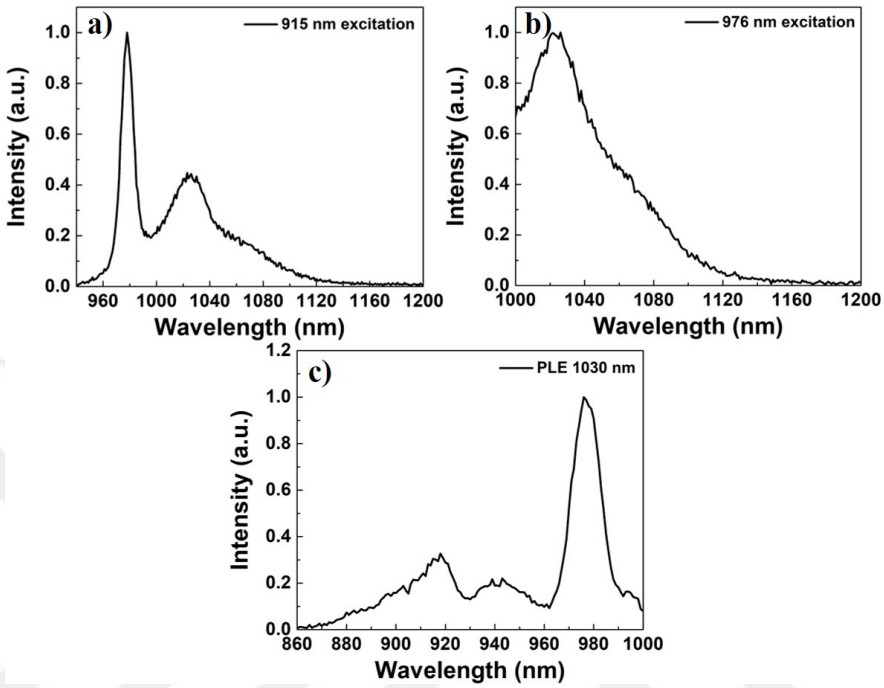

Figure 2.32: Photo-luminescence measurement of the preform a) at 915 nm, b) at 976 nm excitation, and PLE data c) for 1030 nm emission.

wavelength region as sketched in **Fig. 2.32a**. On the other hand, under 976 nm excitation, I have obtained the emission peak around 1030 nm wavelength as can be seen in **Fig. 2.32b**. Additionally, I have also performed photo-luminescence excitation (PLE) measurements to investigate the possible pump wavelengths to obtain 1030 nm emission by this preform as sketched in **Fig. 2.32c**. In descending order, the most dominant excitation wavelength peaks for 1030 nm emission are 976 nm, 915 nm, and 940 nm.

2.3.2.2 Fiber properties

After all these fiber preform analyses, I will elaborate on the optical fiber version of this preform in this section. First of all, it should be noted that the transition from the optical preform to an optical fiber occurs with the help of a fiber draw tower. It consists of a preform feeding mechanism, a furnace, fiber diameter measurement devices, a polymer coating apparatus, UV curing light source, a

capstan, and a take-up spool from top to bottom. The working mechanism of the draw tower can be mentioned shortly that the preform is heated up to its melting point, around 1900 °C by the furnace. The vertical tension applied to the preform is controlled by the temperature of the furnace. The pulling speed arranges the desired cladding diameter of the fiber. Then, low index acrylic polymer is coated on the fiber as a primary coating which endures the total internal reflection inside the optical fiber as a wave-guide. After that, a high refractive index secondary polymer is coated on the primary one to sustain the flexibility of the fiber.

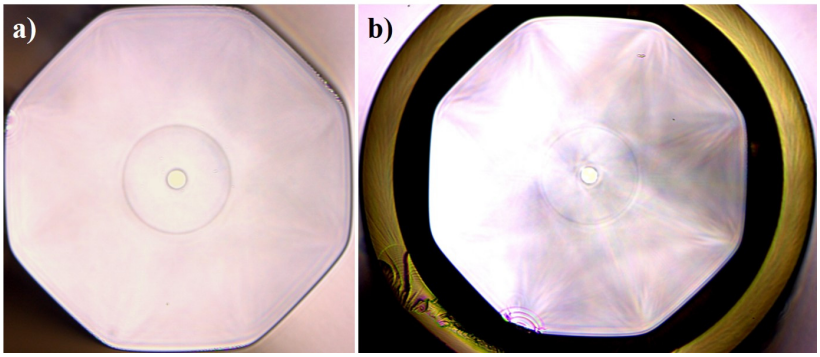

Figure 2.33: The optical microscope image of the active fiber drawn out of 105# preform b) and its polymer coated version

The length of the preform sample may vary between 30 cm to 100 cm, and hundreds of meters or a few kms long fiber could be drawn depending on the diameter of the fiber. In our case, the average length of the preforms manufactured by the MCVD system would be around 40 cm, and approximately 300 m optical fiber has been drawn out of them. In the same manner, 105# fiber preform has been fabricated with these specifications yet altered the furnace temperature to observe the impact on the optical performance of the corresponding fibers. Afterward, the successfully manufactured fiber preforms have been shaped octagonally and drawn to form its optical fiber version with a 20.3 μm/406 μm core and cladding diameters, respectively. The optical microscope of a 105# optical fiber's cross-section without polymer coatings has been shown in **Fig. 2.33a** and with polymer coatings in **Fig. 2.33b**. Moreover, the fiber reaches up to 550 μm in diameter with its polymer coatings.

After that, I would like to investigate the modal content of this fiber, utilizing

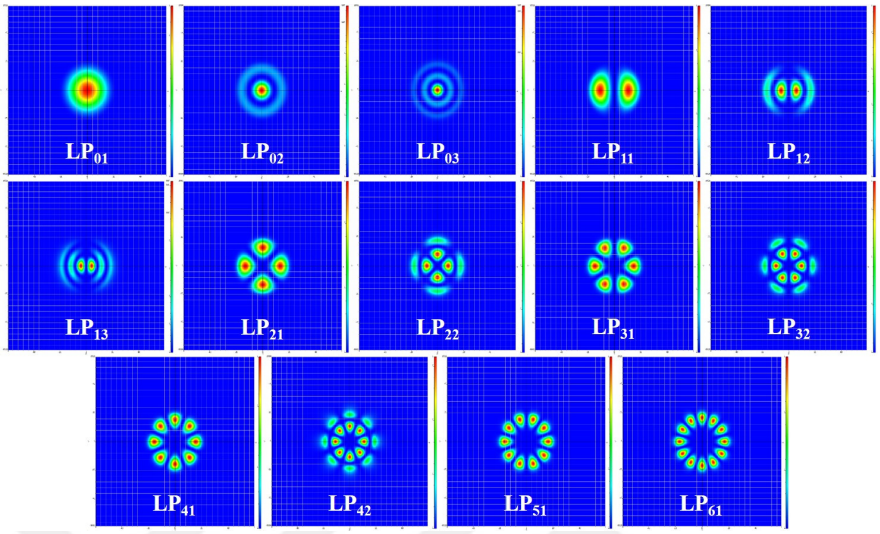

Figure 2.34: Simulation result of the 105# fiber's mode content based on the RIP data of the preform version.

the OptiFiber 2.2.0 version simulation program based on the RIP data of the preform due to the lack of the capability to measure the fiber's modal content directly. As a result, according to the simulation the fiber contains LP_{01}, LP_{02}, LP_{03}, LP_{11}, LP_{12}, LP_{13} LP_{21}, LP_{22}, LP_{31}, LP_{32}, LP_{41}, LP_{42}, LP_{51} and LP_{61} modes as shown in **Fig. 2.34**. This fiber has 14 LP modes based on the 0.089 preform NA; however, the actual fiber has an average NA of 0.06. Therefore, it can easily be concluded that the number of modes that this fiber supports should be lower than 14. Moreover, it can be estimated using the **Eqn. 2.1**.

Since the V number is directly related to the NA, it can also be related to the mode number with its square. Therefore, the estimated one of the 105# fiber would be 8 instead of 14. After estimating the fiber's modal content, I have measured its actual NA utilizing Thorlabs BP109-IR Beam Profiler. I have performed this test at two different conditions: unbent and 10 cm bending diameter to see the change of the fiber NA concerning the bending diameter. For the first case, the fiber was unbent and ensured that only the fiber's Gaussian mode had been excited, and then divergence measurement was performed. The values 7.452° and 7.276° have been obtained with a perfect Gaussian beam profile in x and y directions, respectively, as shown in **Fig. 2.35a**. These divergence angles correspond to 0.064 NA value approximately, calculated using **Eqn. 3.6** for the unbent case.

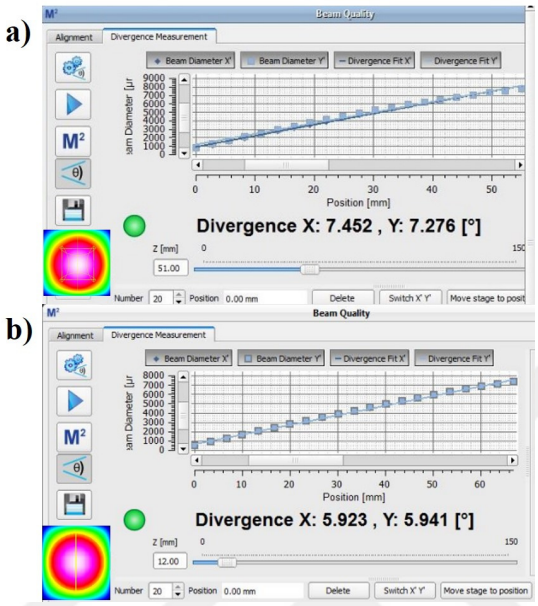

Figure 2.35: Numerical aperture measurement of the fiber (a) unbent and (b) 10 cm bending diameter.

On the other hand, when the fiber was bent in a 10 cm diameter, the divergence angles were obtained as 5.923° and 5.941° in x and y directions, respectively, as shown in **Fig. 2.35b**. Based on this information, the corresponding NA this time would be around 0.052. Consequently, it can easily be said that the NA of this fiber is 0.06 ± 0.005. Another conclusion that could be drawn is that the optimum bending diameter for this fiber is slightly above 10 cm.

2.3.2.3 Laser characterization

After the fiber characterization, it has been tested at a 1 kW output power level in a MOPA configuration. As mentioned briefly above, 105# fiber preform has been drawn at three different temperatures, 1870 °C, 1885 °C and 1880 °C. I have aimed a comparative study to see the impact of the furnace temperature on the optical performance of the fiber version. The drawn fibers will be named from now on in this section as 'Fiber 1', 'Fiber 2' and 'Fiber 3', respectively.

First, Fiber 1 has been tested in a MOPA system similar to the one utilized in

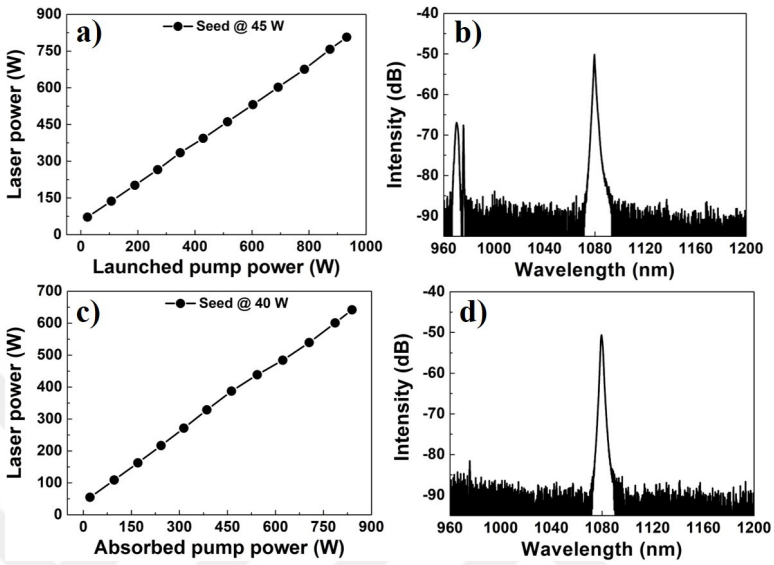

Figure 2.36: (a) The power characterization result of 25 m-long 'Fiber 1' without a CLS, and (b) the corresponding optical spectrum, and (c) with a CLS and (d) its optical spectrum at the maximum power level.

87# fiber. In this amplifier system, 25 m-long Fiber 1 has been implemented in the system considering the Yb concentration of this fiber. In the previous case, 37 m-long 87# fiber had been utilized corresponding to 0.6 dB/m absorption cross-section for 976 nm pump wavelength. Based on this information, the absorption cross-section of 105# fiber would be estimated as around 0.8 dB/m with the help of the ratio of the Yb doping concentration of the 87# and 105# fiber preform. Therefore, I have decided to implement a 25 m-long fiber for a high power test of Fiber 1 considering 20 dB total pump absorption.

The power characterization of 'Fiber 1' has been performed first without a CLS up to 800 W power level as shown in **Fig. 2.36a**. 45 W laser signal power has been amplified up to 800 W in MOPA configuration utilizing 25 m-long active fiber as explained above. The corresponding spectrum at this power level has also been shown in **Fig. 2.36b** with considerable amount of unabsorbed pump power. On the contrary, the same measurement has been reiterated with a CLS component to attain the pure signal power with calculated slope efficiency. This power characterization, however, has been shown in **Fig. 2.36c** up to 650 W power level with 71.2% slope efficiency concerning the absorbed pump power,

which has been assumed that the active fiber has absorbed 90% of the launched pump power. The corresponding optical spectrum has also been shown in **Fig. 2.36d** suppressing nearly the whole unabsorbed pump power.

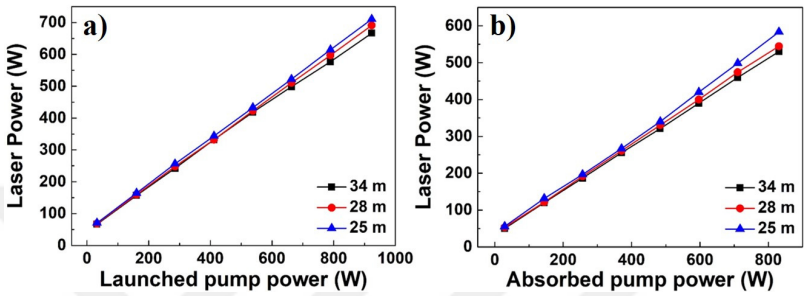

Figure 2.37: The power characterization of the 'Fiber 2' at different fiber lengths (a) without and (b) with a CLS.

After the power characterization of 'Fiber 1', I have decided to confirm the optimum fiber length by the cut-back method during the characterization of 'Fiber 2'. For comparison, I have chosen three different fiber lengths, 34 m, 28 m, and 25 m, to observe the effect on the optical performance of the fiber. In the same manner, two subsequent power characterization of 'Fiber 2' has been performed with and without CLS component whose results have been shared as in **Fig. 2.37a** and **Fig. 2.37b**, respectively. The slope efficiencies obtained are 67.2%, 69.8%, and 71.6%, indirectly related to the fiber length for the launched pump power for without CLS case as in the **Fig. 2.37a**.

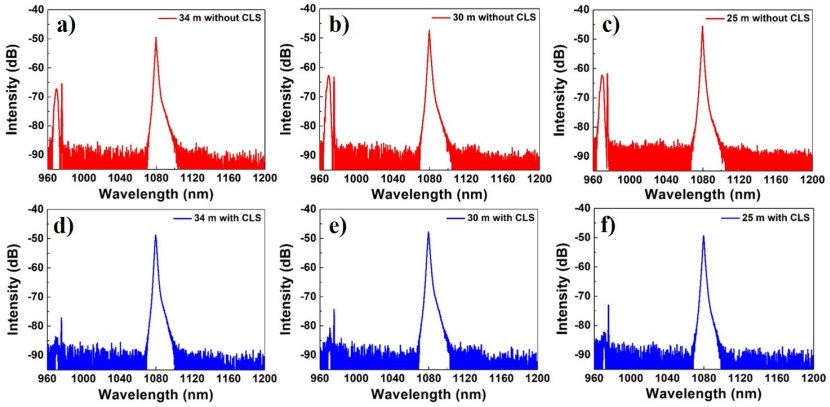

Figure 2.38: The optical spectra belonging to 'Fiber 2' (a) at 34 m, (b) at 30 m, (c) at 25 m without a CLS, and (d) at 34 m, (e) at 30 m, (f) at 25 m with a CLS for comparison.

Therefore, it can easily be concluded that the best slope efficiency belonged to the 25 m fiber length. The optical spectra obtained for different fiber lengths have been shown with and without the CLS component as shown in **Fig. 2.38**. As expected, as the fiber length shortens, the intensity of the unabsorbed pump power slightly increases.

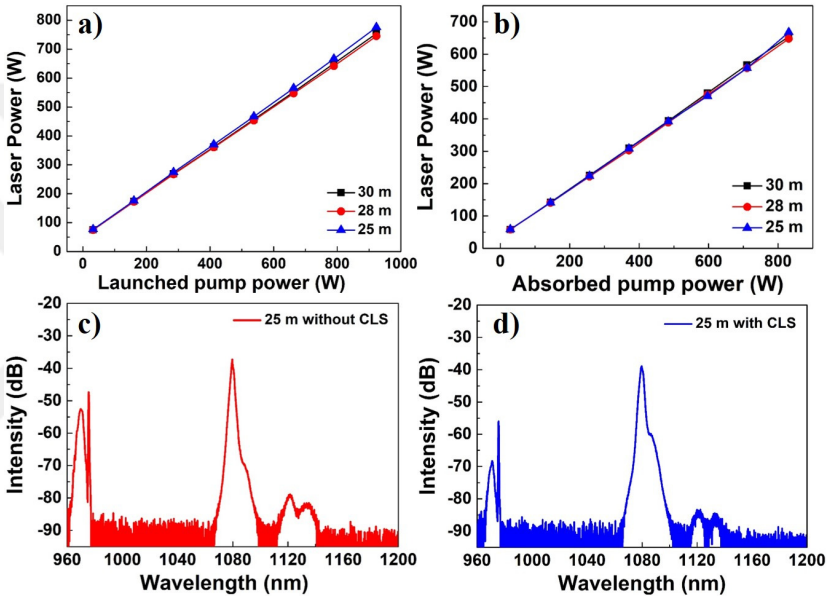

Figure 2.39: The power characterization of the 'Fiber 3' at different fiber lengths (a) without and (b) with a CLS, and the optical spectra (c) at 25 m without and (d) with a CLS utilizing six pieces of pump diodes.

Similarly, 'Fiber 3' has also been tested with three different fiber lengths in the same setup to observe the same effect on the optical performance of this fiber. For this experiment, 30 m, 28 m, and 25 m fiber lengths have been iterated. It should be noted that all of the high power tests mentioned until this time have been conducted with six pieces of pump diodes. Each pump diode has a 250 W maximum capacity; however, each diode has been operated at an average of 154 W and a total of 922 W pump power. Therefore, although the pump diodes have VBG stabilization system, the parasitic pump wavelength region appears more dominantly in the low power regime. Similarly, I have also tested 'Fiber 3', and the corresponding results with and without CLS have been shown in **Fig. 2.39a** and **Fig. 2.39b**, respectively.

The so-called situation mentioned above about pump wavelength would be seen in the optical spectra of 'Fiber 3' on the left side of the 976 nm pump wavelength as shown in **Fig. 2.39c** and **Fig. 2.39d** belonging to 25 m fiber length. The slope efficiencies of the three different fiber lengths were similar, and that is to say, the average slope efficiency can be said that 74% for 'Fiber 3'. One possible reason for this situation would be the chosen fiber lengths are close to each other. However, the best slope efficiency has been attained with 'Fiber 3' in the same configuration. Though there is a slight difference between them, this fiber behaved the most reliable and efficient.

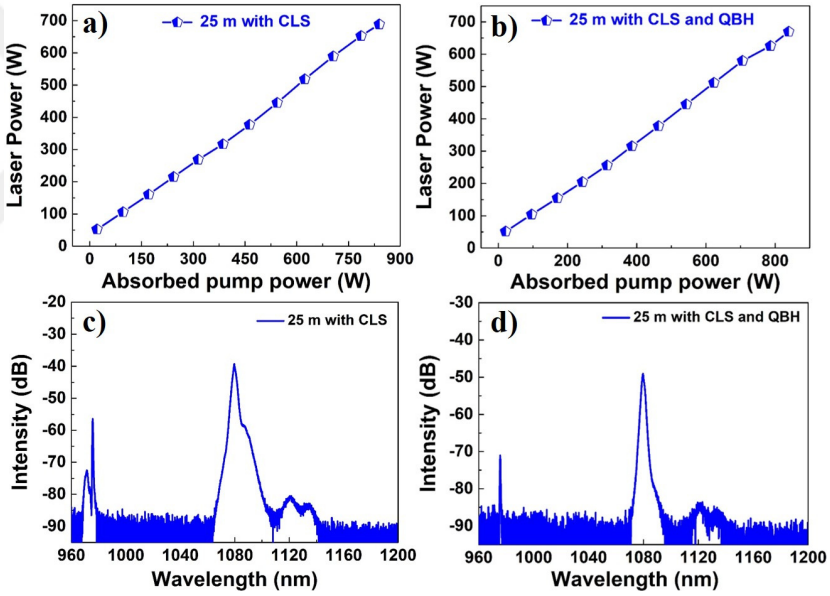

Figure 2.40: The power characterization of the 'Fiber 3' (a) at 25 m with CLS, and b) with CLS and QBH, (c), and (d) the corresponding optical spectra utilizing four pieces of pump diodes.

After that, I slightly changed the test setup, decreasing the number of the pump diodes from six to four to explore the situation about the pump wavelength mentioned above. In this configuration, the operating power of each diode has been increased to the 233 W power level, and thus the total pump power reaches up to 932 W power level. The characterization has been performed again to observe the difference between these two pumping conditions. The results obtained have been shown in **Fig. 2.40a** and **Fig. 2.40b** for with CLS and also a QBH cable for 25 m fiber length, respectively. For this case, red-shift of the

pump wavelength increased pump absorption and gain saturation, and thus the slope efficiency was enhanced up to 76% based on absorbed pump power. The corresponding optical spectra have been shown in **Fig. 2.40c** and **Fig. 2.40d** for the CLS and QBH cases, respectively. As can be seen from the figures, with CLS, the parasitic pump wavelength region has been suppressed better, yet on the other hand, with CLS and QBH, this region has been suppressed even better.

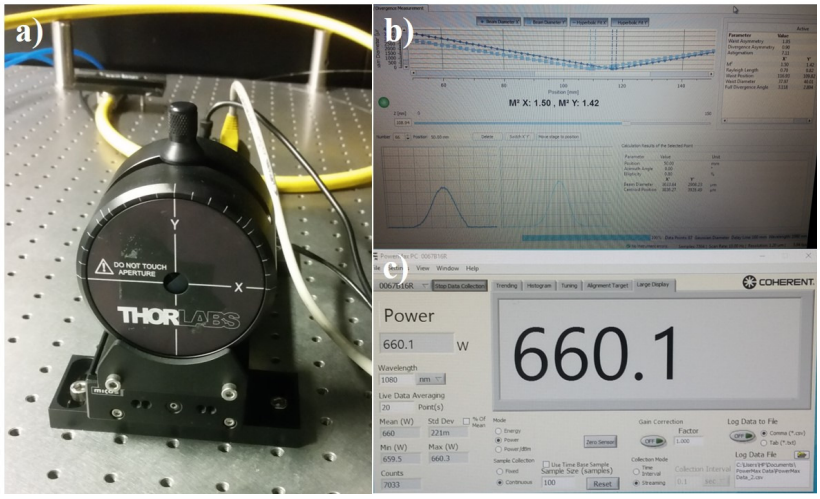

Figure 2.41: (a) The picture of Thorlabs BP109-IR Beam profiler, and b) the beam quality measurement result for 'Fiber 3' (c) at 660 W power level.

Finally, the beam quality of the fiber has been tested using Thorlabs BP109-IR beam profiler whose photograph has been shown in **Fig. 2.41a**. The obtained data has been shown in **Fig. 2.41b** with 1.50 and 1.42 in x and y coordinates, respectively. The beam quality measurement has been conducted at the 660 W maximum power level as shown in **Fig. 2.41c**.

As a brief summary to this section, I have managed to fabricate Yb-doped active fibers having similar properties and efficiencies compared to the counterparts demonstrated in the literature. Optical characterization results presented above have confirmed this fact.

Chapter 3

Ultra-low NA Home-Made Active Fiber

3.1 Introduction

Fiber lasers have been widely used in the industry besides the health and defense applications due to their critical features such as robustness, compactness, and directionality. It has been possible to achieve kW class fiber laser systems after the developments in the optical fiber technology introducing the generation of Large Mode Area (LMA) fibers with low numerical aperture (NA) values 0.06 [127–130]. This breakthrough has provided the use of fiber lasers in the defense industry as well. The fabrication of these silica glass-based LMA optical fibers can be performed with the use of the Modified Chemical Vapor Deposition (MCVD) technique [131, 132]. High purity and high-quality preforms can easily be manufactured using this technique since the chemicals have a purity level of 5N or 6N. Therefore, the LMA fibers used in defense application in the multi-kW power levels have been preferred to be manufactured with this method since the impurity level gains importance when the power scales up. Moreover, it is possible to monitor and control both the amount and flow of the chemicals, which is an important fact to lower the difference between the refractive indices of the

core and inner cladding regions for the fabrication of low NA optical fibers [133]. Since MCVD is a complex system, precise controlling the doping concentration of each element is very challenging. The main reason is that the precursors used in the system, namely silicon tetrachloride ($SiCl_4$), aluminum chloride ($AlCl_3$), and phosphorous oxychloride ($POCl_3$) with different deposition efficiencies, get in a competition within the silica host matrix. Therefore, it requires a great effort to successfully place different dopants in the host matrix to adjust the desired refractive index profile (RIP). As mentioned above, multi kW fiber laser systems have been accessible with LMA fibers since they have larger core diameters than those of intrinsically single-mode fibers with corresponding higher optical power damage and non-linear effect thresholds. Depending on how large the core diameter is, LMA fibers supporting more than one mode are also called few-mode optical fibers, which imply that, in addition to the fundamental mode (LP_{01}), higher-order modes (HOMs) also survive inside the optical fiber. The beam quality of a laser system scales with the proportion of the fundamental mode. Therefore, the quality of the laser output beam decreases dramatically with the presence of HOMs inside the fiber. Besides, the presence of HOMs can cause other non-linear effects over certain pump power threshold levels. One of them is named Transverse Modal Instability (TMI) which has a thermal origin and is said to be caused by the Stimulated Thermal Rayleigh Scattering (STRS) or by thermal mode coupling processes alternatively [134, 135].

This phenomenon will be discussed further in the next chapter; however, some basic information will be given briefly. According to the mode-coupling theory, fundamental and HOMs interfere, so a modal interference pattern (MIP) is created as a result. This MIP then causes the fiber's refractive index profile (RIP) has been modified periodically to form refractive index grating (RIG) structures. Due to the presence of them inside the fiber, the total energy in the fundamental mode couples to the HOMs and then return to the fundamental mode in a repeating manner [136, 137]. Therefore, HOMs should be suppressed inside the fiber to survive only the fundamental mode, not to confront such an undesirable situation. The most basic and essential method to getting rid of the HOMs is the bend-induced loss mechanism. The fiber is bent at a specific diameter so that

HOMs cannot propagate inside the fiber anymore. However, the bend-induced mechanism is a temporal solution since when the fiber is back to the initial position, HOMs presents again. In that respect, a permanent approach is to lower the NA of fiber which can be achieved in two possible ways. The first method is decreasing the refractive index of the core region by lowering the rare earth dopant concentration or doping Fluorine and Boron atoms. On the other hand, the other one is increasing the refractive index of the cladding region by doping Germanium atoms.

In this work, I have chosen to decrease the doping concentration of the Yb atoms in a controlled manner to design and fabricate a new type of large core active fiber to stop the intrinsic formation and propagation of HOMs inside the fiber. With the help of lowering the NA of fiber, this new approach can only support the propagation of fundamental mode even with a larger core size depending on its V number.

In the literature, an active fiber having an NA value <0.05 and 40 μm core diameter was demonstrated firstly in 2004 above 1 kW with an $M^2 = 1.4$ [138], and another one having an NA value of 0.038 and 35 μm core diameter was proposed in 2015 with an average $M^2 = 1.08$ but just about 50 W power level [139]. Additionally, systematic numeric studies were performed to simulate the laser output characteristics by varying the NA (0.025–0.05), core diameter (20 μm–100 μm), and the bending diameter (0.4 m–1.6 m) of the fiber by authors of [140]. Afterward, a 3 kW output power level was achieved by designing a new low NA fiber with an NA value of 0.048 and $M^2 = 1.15$ [141]. Yet another active fiber has been proposed with an NA value ≈ 0.04 and $M^2 = 1.3$ with 3 kW output power [142]. Having upgraded this work, the highest power level in the literature, which is 4.3 kW, had finally been achieved by Tünnermann's group with an active fiber having an NA value again ≈ 0.04 and 23 μm core diameter resulting in an average M^2 value of 1.24 [143]. However, all of these works are based on free space orientation; that is to say, pump light is coupled to the active fiber via free space with the help of several lens and objective combinations. On the other hand, recently, all-fiber ultra-low NA fiber laser studies started to be published in a resonator configuration [144]. Also, it has been implemented in the

oscillator part of an amplifier system, [145]. However, I demonstrate a monolithic all-fiber high-power Master Oscillator Power Amplifier (MOPA) system based on an ultra-low NA Yb-doped active fiber in this work. It has 26 μm core and 410 μm cladding diameters, respectively, with an average NA value of 0.034, experimentally verified. The details of this study will be given in the subsections below.

3.2 Preform Fabrication and Characterization

In this section, properties of the preform version of the ultra-low NA fiber are going to be presented. Besides, all of the analysis that has been done to characterize the preform are going to be elaborated. However, at first the fabrication of fiber preform is going to be mentioned briefly. All starting raw chemicals used in MCVD system were purchased with high purity levels of 5N (99.999%) and 6N (99.9999%) to manufacture ultra-low NA fiber preform. A Heraeus branded F300 quartz substrate tube whose inner diameter is 24 mm and the outer one is 28 mm, was used for the deposition at 1930 ℃ via an H_2/O_2 torch. Then, the substrate tube was collapsed at 2050 ℃ by a furnace. Upon obtaining the preform, core/clad ratio was adjusted by the post-processes such as stretching and jacketing using the MCVD system as well. After manufacturing process, characterizations of the final preform were conducted using a Polariscope to observe the discrepancies if exists any in the core region, an optical microscope Zeiss Axio Vert A1 to see the cross-section, a P102 Photon Kinetics preform analyzer to measure the refractive index profile (RIP). Then it was drawn by an OptoGear branded fiber drawing tower and the drawn fiber was coated with primary and secondary polymers to make it bendable. The data belonging to these characterizations are going to be shared below subsequently.

$$\begin{aligned} SiCl_4 + O_2 &= SiO_2 + 2Cl_2 \\ 2POCl_3 + \frac{3}{2}O_2 &= P_2O_5 + 3Cl_2 \end{aligned} \tag{3.1}$$

The production of preform has been initiated with the help of precursors to build the cladding and core regions subsequently. And since the type of fibers that have been fabricated are Yb-doped aluminophosphosilicate (APS) [Al_2O_3-P_2O_5-SiO_2] fiber, the precursors namely $SiCl_4$ and $POCl_3$,$Yb(thd)_3$ [Yb-(tetramethylheptanedione)] and $Al(acac)_3$ [Al-(acetylacetonate)]. The formation of SiO_2 and P_2O_5 occurs via oxidation reactions as stated in **Eqn. 3.1** above. The liquid precursors, $SiCl_4$ and $POCl_3$ are heated up to a specific temperature around 35°C and oxygen (O_2) carrier gas and vaporized precursors flow from the bubblers to interior part of the high-purity glass tube where the so-called oxidation reaction will take place. On the other hand, $Yb(thd)_3$ and $Al(acac)_3$ precursors are in solid phase unlike others and they have been sent to the system in gas phase via sublimation reaction by applying heat around 130°C – 140°C for $Al(acac)_3$ and 190°C – 200°C for $Yb(thd)_3$. Additionally, Helium flows through this furnace and other parts are also heated up to 200 °C to prevent the formation of condensation in the system.

For the fabrication of this specific preform, I have aimed to decrease the doping concentration of Yb_2O_3 for the sake of lowering the NA of preform whose RIP has been shown in **Fig. 3.1**. The RIP of manufactured preform has been measured by the preform analyzer system stated above operating at 633 nm wavelength range. For that purpose, a preform slice with a thickness less than 4 mm was used in this measurement. The RIP of nearly whole preform (17.4 mm) was shown in **Fig. 3.1a** in which the core region was pointed out. To investigate it deeply, the zoomed-in version of **Fig. 3.1a** was sketched as in **Fig. 3.1b**. It is a well-known fact that Yb^{3+}, Al^{3+} and P^{5+} ions lead to increase the refractive index individually. However, in the case of APS fiber,Al^{3+} and P^{5+} ions can yield to formation of $AlPO_4$ structural units within the silica host matrix. Thus, the individual refractive index additive effect of these elements has been neutralized automatically.

From benefiting this fact, it has been aimed to dope the silica glass with equimolar amounts of Al_2O_3 and P_2O_5 so that the $AlPO_4$ formation help to reduce the refractive index [146, 147]. Therefore, this implies that the formation of $AlPO_4$ could be utilized to decrease the NA of fibers.

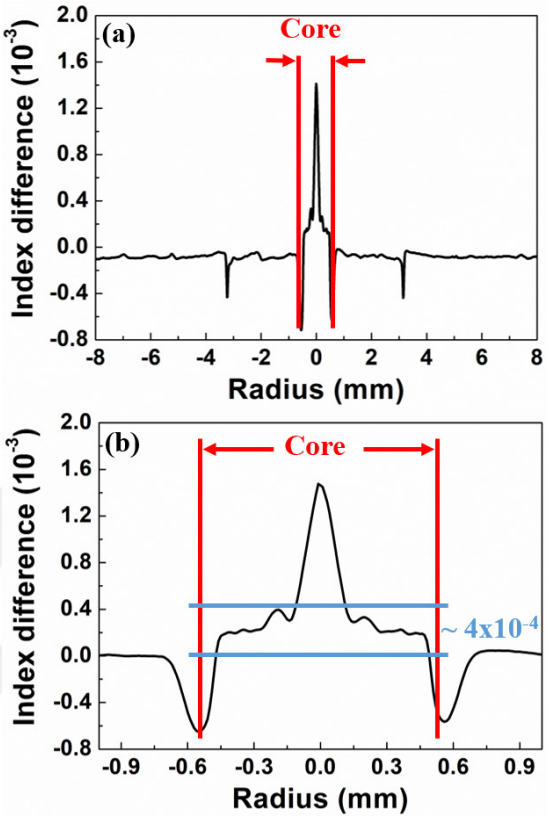

Figure 3.1: (a) Refractive index profile (RIP) of the nearly whole preform and (b) just the core region.

However, in our case I have chosen to decrease the doping concentration of Yb_2O_3 to alter the NA of preform and since Al^{3+} plays critical role for Yb^{3+} to find place in the core region instead of doping Al^{3+} and P^{5+} ions as equal as possible, I have aimed to dope Al^{3+} more than P^{5+} intentionally in a controlled manner. However; in the contrary to our intention there existed an undesired peak at the center of the core region of the preform, which has been created during the collapse pass of the manufacturing process of the preform. Since the homogeneity of preform's RIP has been deteriorated by peak at the center, taking into consideration of this fact, I have predicted and claimed that the average index difference of the whole core region might be calculated as $4x10^{-4}$ as indicated in Figure **Fig. 3.1b**.

$$NA = \sqrt{n_{core}^2 - n_{clad}^2} = \sqrt{(n_{core} - n_{clad}) \times (n_{core} + n_{clad})} \tag{3.2}$$

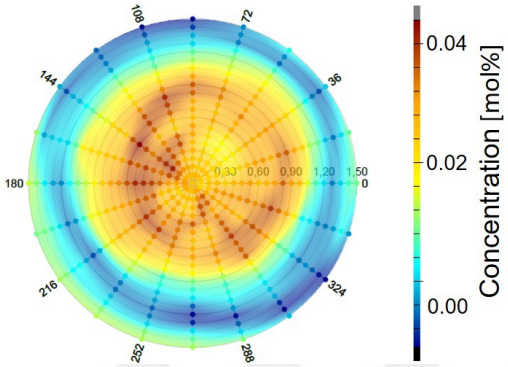

Figure 3.2: MOPS data of the preform version of the ultra-low NA fiber.

Having utilized the **Eqn. 3.2**, such index difference would correspond to an NA value of 0.034 theoretically, where the average refractive indices of the core and cladding region of the fiber are 1.4480 and 1.4476 respectively. As mentioned briefly above, preforms have also been characterized in terms of their elemental composition in order to determine the doping concentrations of individual elements before the drawn. There are two analysis systems at UNAM for rare-earth element, which is Ytterbium in our case, that I have implemented for the preform analysis. One of them is called as MOPS (Measurement of Optical Preform Slice) by the manufacturer company of the MCVD system, capable of mapping the elemental composition of the preform in addition to the percentage of them based on the emission technique.

MOPS data of the ultra-low NA fiber preform has been shown as in **Fig. 3.2**.The distribution and concentration of Yb atoms within the core region has been plotted. According to the MOPS data doping concentration of the Yb_2O_3 lies between 0.03mol% and 0.04mol% all over the core region of the preform. This data has been verified with another technique, Wavelength-dispersive spectroscopy (WDS), a measurement method integrated to a Scanning electron microscope (SEM) system. Contrary to MOPS technique, WDS is capable of measuring the doping concentration of all elements inside the preform. Therefore, we will find out the doing concentrations of Al_2O_3 and P_2O_5 in addition to Yb_2O_3 with this technique. For that measurement, I have taken a polished ultra-low NA fiber preform piece with a 4 mm thickness and 2 mm total core diameter. As a comparison I have taken measurements at selected points in both cladding and

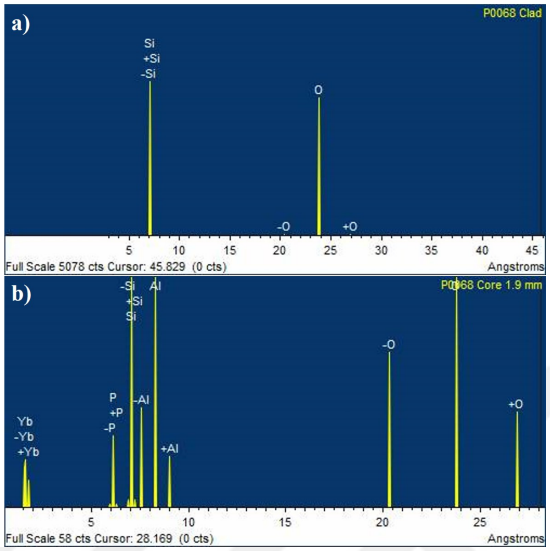

Figure 3.3: Wavelength-dispersive spectra of the selected points in a) clad and b) core region of the preform.

core regions to illustrate the material composition difference between them as can be seen in **Fig. 3.3**. The cladding region of preform contains only Silicon and Oxygen atoms as expected and can be seen in **Fig. 3.3a** whereas the core region contains Yb^{3+}, Al^{3+} and P^{5+} as well as the Silicon and Oxygen as can be seen from the **Fig. 3.3b**. After the verification of presence of all these elements inside the cladding and core regions of the preform, we are supposed to quantify the doping concentration of these elements.

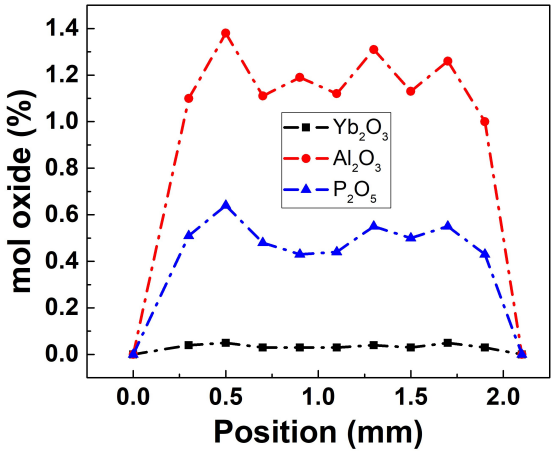

Figure 3.4: Mapping data of the elements which are Yb_2O_3, Al_2O_3 and P_2O_5 over the core region of the preform via WDS measurement technique.

For that purpose, whole core region has been scanned with 0.2 mm steps and a single measurement has been at each step and recorded. As a result, the obtained data has been plotted for the elements Al_2O_3 and P_2O_5 and Yb_2O_3 as shown in **Fig. 3.4**. The average doping concentrations for Al_2O_3 and P_2O_5 and Yb_2O_3 are **1.178 mol%**, **0.503 mol%** and **0.037 mol%**. Consequently, it can be concluded that WDS and MOPS data for doping concentration of Yb_2O_3 are in good agreement with each other. In addition to this, as the number suggests our intention has been fulfilled with this much low Yb ion doping concentration and thus we would be able to achieve ultra-low NA fiber out of this preform.

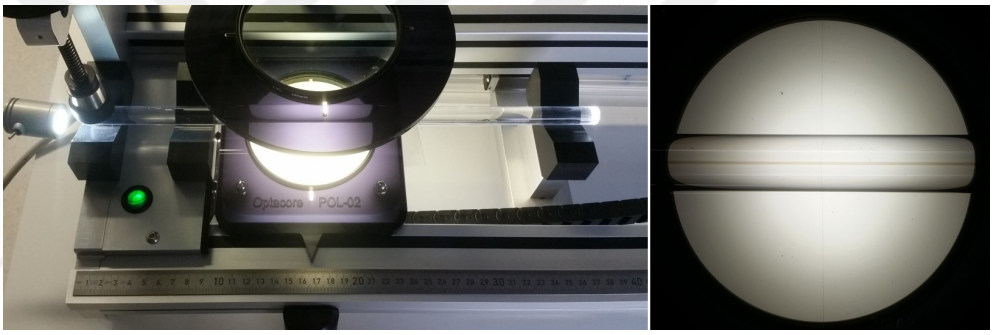

Figure 3.5: a) Optacore POL-02 polariscope system and b) the image of P0068 preform taken by this polariscope.

In addition to the MOPS and WDS measurements, the physical properties of the core region of the preform has also been investigated by Optacore POL-02 polariscope system to monitor any discrepancy in the core region if there is any, as can be seen from the **Fig. 3.5**. To make it clear, the working principle of this system is so simple that a white light source is coupled to one end of the preform and with the help of two crossed polarized lenses, and thus core region could be monitored from benefiting the refractive index difference between the cladding and core regions on which the contrast of image is strongly depends on. This implies that there is a direct relation between the contrast of image and NA of preform. In this case, since P0068 (Ultra-low NA fiber preform) has a smaller NA value due to low doping concentration of Yb_2O_3, the image contrast is relatively small compared to the ones of P0087 an P0105 which has been elaborated in Chapter 2 of this thesis.

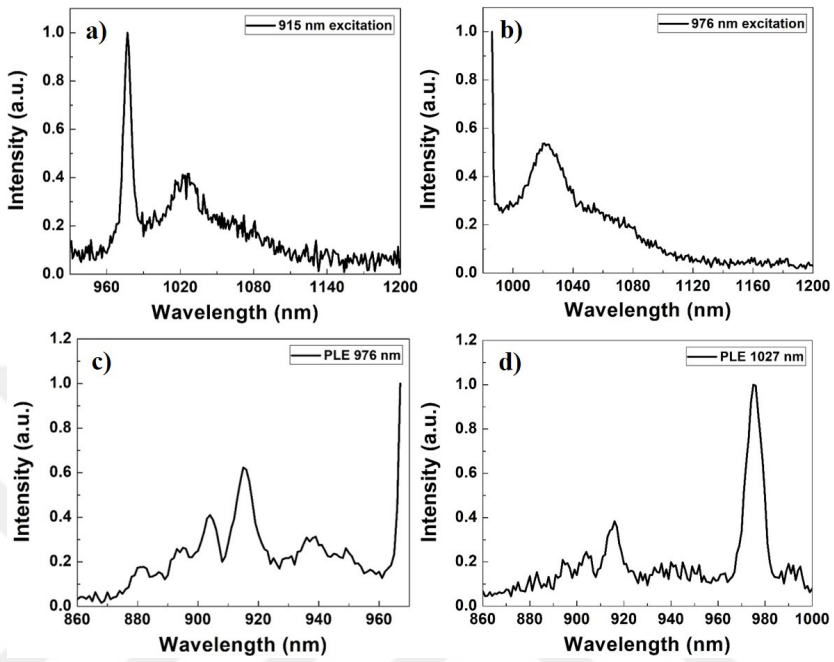

Figure 3.6: Photo-luminescence measurement of the preform a) at 915 nm and b) at 976 nm excitation, and PLE data c) for 976 nm and d) 1027 nm emission.

After examining the elemental composition and physical properties of this preform, the optical behaviors namely the absorption and emission capability, have also been investigated. For that purpose, I have utilized Time Resolved Fluorescence (TRF) Spectrophotometry system located at the 2^{nd} floor of UNAM building whose results have been shown in **Fig. 3.6**. Having known that, the two most dominant absorption cross section of the Yb ion are around 915 and 976 nm, I have chosen them as the excitation wavelengths. Under 915 nm excitation wavelength, the dominant and narrower emission occurs around 976 nm whereas the second and broader one is approximately 1030 nm wavelength region as sketched in **Fig. 3.6a**. On the other hand, under 976 nm excitation I have obtained the emission peaks at 976 nm and 1030 nm wavelengths respectively as can be seen in **Fig. 3.6b**. For a comparison, the 1030 nm emission from 976 nm excitation seems to be higher than the one from 915 nm excitation as can be clearly seen from the **Fig. 3.6a** and **Fig. 3.6b**. This data is consistent with the information given above which is the absorption cross section of Yb ion at 976 nm is larger than 915 nm.

Additionally, I have also performed photo-luminescence excitation (PLE) measurements to investigate the possible pump wavelengths to obtain 976 and 1027 nm emissions by this preform as sketched in **Fig. 3.6c** and **Fig. 3.6d** respectively. The most dominant excitation wavelength peaks for 976 nm emission have been obtained as 915 nm, 904 nm and 939 nm in descending order as can be seen from **Fig. 3.6c**. In the same manner, for 1027 nm emission the most dominant excitation wavelengths are 976 nm, 916 nm, 904 nm, 894 nm and 940 nm in descending order again. All of these emission and excitation wavelengths correspond to the required energies between the three levels of $^2F_{5/2}$ and the ground state of $^2F_{7/2}$ of Yb atom as discussed in the chapter 1 of this thesis.

3.3 Fiber Properties

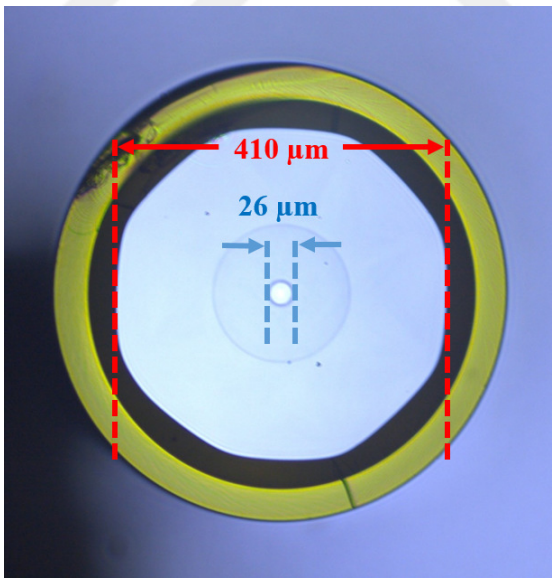

Figure 3.7: Optical microscope image of the cross section of the drawn fiber.

When the procedure of fabrication of preform has been carried out, the following step would be drawing the preform out of the fiber. The details of fiber drawing process has been elaborated in the introduction section of Chapter 2 and so the explanation of this process will be skipped in this section. Having completed the preform fabrication and characterization section, properties of fiber

version of the preform are going to be elaborated in this section. First of all, the physical properties of fiber is going to be shared. Therefore, a piece of the fiber was cleaved at an angle close to zero with its polymer coating onside, and an optical microscope image of the cross-section of the drawn fiber has been taken and illustrated as shown in **Fig. 3.7**. The core and the cladding diameters of the ultra-low NA active fiber have been measured as 26 μm and 410 μm respectively. Additionally, the diameter of the fiber reaches up to 550 μm with its polymer coating. Since I have a predicted NA value on hand, I can also calculate the V number of the fiber easily just for the sake of getting an idea about the modal content of this fiber. V number depends on the NA and the core radius of the fiber.

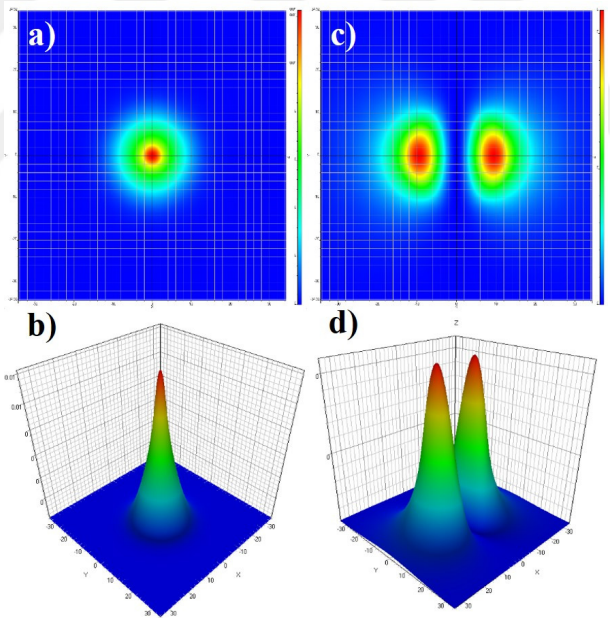

Figure 3.8: Simulation results of the mode content of the ultra-low NA active fiber.

It is general fact that when the V number of a fiber is smaller than the threshold value of **2.405** then this fiber is said to be intrinsically single mode which means that there can be no HOMs to survive in this fiber. When I calculate the V number of this fiber according to the equation above, with a predicted NA value of 0.034, the core radius of 13 μm and finally assuming the wavelength is 1.08 μm, we come up with a number of **2.57** which is relatively a bit larger but still very close to the threshold value. Therefore, I can easily conclude that the fiber

reported in this study is considered to be not an intrinsically single-mode one. Nevertheless, HOMs can be eliminated even with a large bending diameter for this special fiber. To investigate the mode properties of this unique fiber, I have utilized OptiFiber 2.2.0 version simulation program. The refractive index profile (RIP) of the fiber is the input for this program. For that purpose, I have used the RIP data obtained from the preform version of this fiber to see the resemblance. I have fitted the RIP of the preform to the fiber version with 26 μm/410 μm core/cladding diameters, respectively, as shown in **Fig. 3.7**. Since the V-number of this close to the single-mode threshold value, it can be expected that just a few HOMs to appear along with the fundamental mode. Parallel to this expectation, I have obtained the result as shown in **Fig. 3.8**. Therefore, according to the simulation this fiber includes just LP_{11} as HOM with the fundamental mode (LP_{01}). In addition to the 2D images of the modes shown in **Fig. 3.8a** and **Fig. 3.8c**, 3D images of the both modes have also been illustrated in **Fig. 3.8b** and **Fig. 3.8d**, respectively.

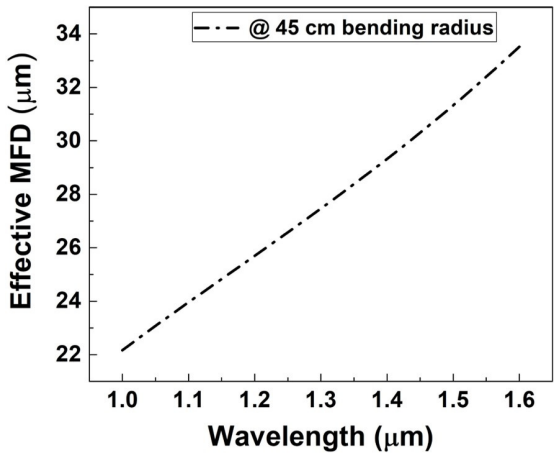

Figure 3.9: Simulation results of the effective mode diameter of the ultra-low NA active fiber versus wavelength with 45 cm bending radius.

Besides, I have also calculated the mode field diameter (MFD) of this fiber with the same simulation program. I have entered the similar parameters such as core radius, the RIP same as the one above. In return, I have obtained the result shown in **Fig. 3.9**. The MFD of the fiber starts around 22 μm corresponding to 1 μm wavelength region and climbs up to 34 μm corresponding to 1.6 μm wavelength.

In the previous section it has been explained that preform of this fiber has been manufactured by decreasing the doping concentration of Yb_2O_3 in a controlled manner to achieve the ultra-low NA fiber. It is reminder that the RIP of so-called preform has been shown in **Fig. 3.1** and based on this data the average RIP of the preform had been calculated as $4x10^{-4}$ which corresponds to a NA of 0.034 theoretically. However, this number needs to be verified experimentally in the fiber version as a comparison. For this purpose, I have built an experimental setup to measure the NA of fiber directly which consisted of a laser source operating at 1200 nm central wavelength. The reason why this one has been chosen specifically is due to the less absorption of Yb atoms at that wavelength region.Then, a Thorlabs F230APC-1064 fiber-coupled collimator having an NA of 0.50 and focal length of 4.56 mm has been used in this system to collimate the outgoing laser light.

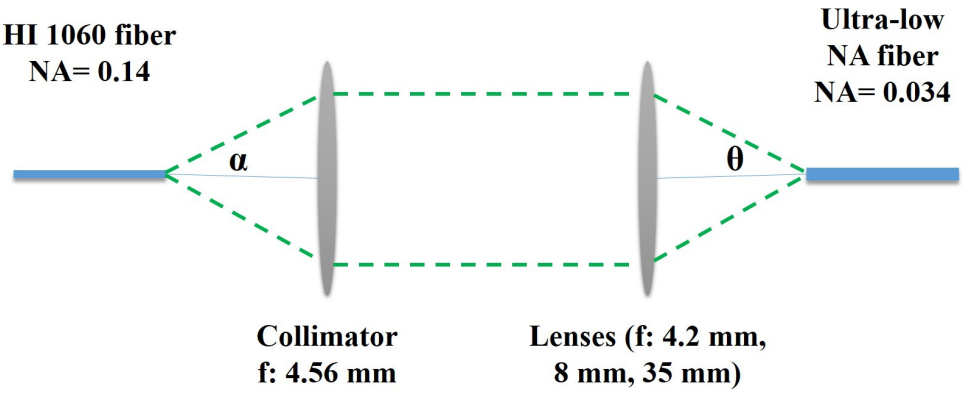

Figure 3.10: Schematic illustration of the beam divergence measurement setup based on the change in excitation NA of the source.

Finally, an aspheric lens, which helps to get rid of the spherical aberration, has been utilized to focus the laser light into fiber. At the end of setup, a Thorlabs BP109-IR beam profiler has been operated to measure the beam divergence data of ultra-low NA fiber so that the NA value of the fiber could be calculated accordingly. For the sake of this measurement, I have aimed to demonstrate the fiber NA invariance with respect to the different excitation NA and the bending diameters.

To start with, I have examined the effect of excitation NA on the fiber NA itself.

To illustrate, the schematic representation of the beam divergence measurement of the fiber under different excitation NA of the source has been sketched as in **Fig. 3.10** which has been altered by changing the aspheric lens just before the 8 m-long ultra-low NA fiber piece. Since we know the fiber NA of the laser source we can easily calculate the tangent of out going angle of the laser beam based on the **Eqn. 3.3**.

$$\sin(2\alpha) = 0.14 \Rightarrow \tan(\alpha) = 0.07035 \tag{3.3}$$

$$\tan(\theta) = \frac{f_{collimator}}{f_{lens}} \times \tan(\alpha) = \frac{4.56mm}{f_{lens}} \times (0.07035) \tag{3.4}$$

$$(ExcitationNA) \equiv \sin(2\theta) \tag{3.5}$$

We had 3 pieces of aspheric lenses having 4.2 mm, 8 mm and 35 mm focal lengths to alter the excitation NA of the laser source. Based on the values of each lens, the excitation NAs have been calculated as 0.152, 0.080 and 0.018 respectively according to the **Eqns. 3.4 and 3.5** below.

At these three different scenarios, the beam divergence measurement has been repeated and the results are as in **Fig. 3.11a**. The divergence angles corresponding to each excitation NA are 3.784°, 3.899°, and 3.669° respectively. Then, the corresponding fiber NA values have been calculated as 0.0329, 0.034 and 0.032 as shown in **Fig. 3.11b** from benefiting the **Eqn. 3.6**. Consequently, the average NA value based on these different excitation NAs can easily be found as 0.0335± 0.00055. Based on this information that I have obtained from all of these three measurements, it can be concluded that no matter how the excitation NA was changed the NA of this fiber is indeed around 0.034.

$$NA = \sin\left(\frac{\theta}{2}\right) \tag{3.6}$$

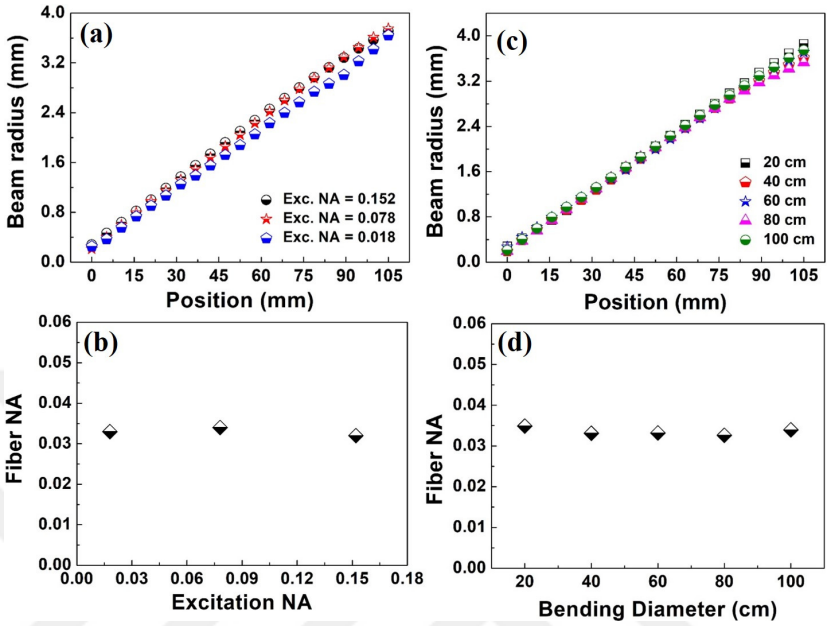

Figure 3.11: (a) Beam divergence measurement of the fiber with respect to the excitation NA and (b) the corresponding NA values, (c) the same measurement this time with respect to the bending diameter and (d) the corresponding NA values again.

After that, I have performed the NA measurement this time by changing the bending diameter of the fiber from 100 cm to 20 cm in order to observe the bending effect on the NA of fiber while the excitation NA is fixed at 0.080 by implementing an aspheric lens having 8 mm focal length right after the collimator. The reason why excitation NA was chosen larger than our prediction of the fiber NA is to make sure that the whole fiber was fulfilled so that to be able to measure directly the NA of fiber rather than the divergence of the light passing through. Under these circumstances, the divergence data that I have obtained from the beam profiler are as in **Fig. 3.11c**. The acceptance angles corresponding to each bending diameter are 3.989°, 3.794°, 3.805°, 3.736°, and 3.885° respectively. By taking the sine of the half of these divergence angles for each bending diameter, I have obtained the fiber NA values as shown in **Fig. 3.11d** by using the **Eqn. 3.6**. The fiber NA values obtained with respect to the bending diameters of the fiber are 0.0348, 0.0331, 0.0332, 0.0326 and 0.0339 correspondingly. The average NA value of these 5 different NA values is then found as 0.0337± 0.0011. In summary, it has been proven that neither the bending diameter of the fiber nor

excitation NA of the source can not affect the NA of fiber and it has been verified that the actual NA of the fiber is around 0.034 as claimed in the previous section.

In addition to the NA verification measurement, the fundamental mode loss of the fiber has also been studied to investigate the effect of bending diameter of the fiber on fundamental mode propagation inside. This information is critical for bend-sensitive fibers such as ultra-low NA ones which is of concern in this study. The data which is going to be extracted here will give a clue about the critical bending diameter of the fiber which means that if the fiber is bent beyond this point the guiding of fundamental mode will be damaged drastically.

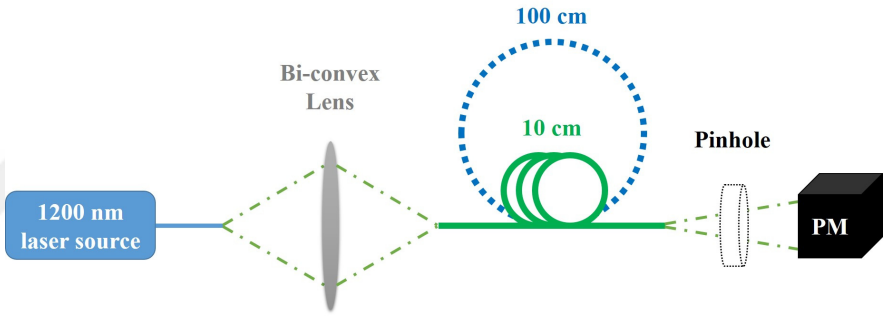

Figure 3.12: Schematic illustration of the fundamental mode loss measurement of the fiber.

For that purpose, I have installed a simple setup consisting of a laser source again operating at 1200 nm wavelength range with the same motivation mentioned above.But this time a bi-convex lens to focus the light directly into the fiber and a pinhole to prevent the light coming from the cladding region of the fiber as shown in **Fig. 3.12**. After the free-space alignment of the optical elements has been completed, the laser source has been kept constant during the whole measurement and the lens has not been touched after the optimal coupling condition has been satisfied to ensure that the only variable in this measurement would be the bending diameter of the fiber which has been altered from 100 cm to 10 cm in order to observe the loss of fundamental mode of the fiber precisely. The data obtained from this measurement has been plotted as shown in **Fig. 3.13**. Based on this data, the fundamental mode loss dramatically increases beyond the 50 cm bending diameter. Therefore, it can easily be concluded that the critical bending diameter for this fiber is around 50 cm.

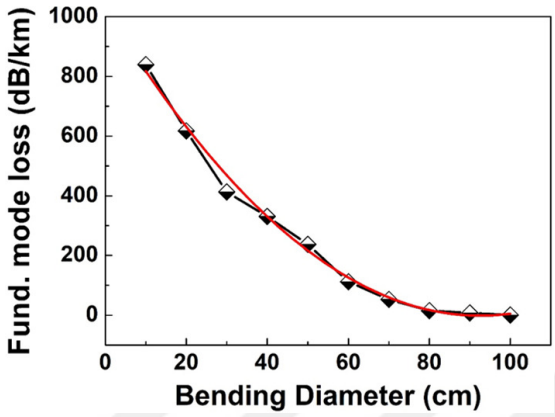

Figure 3.13: Fundamental mode loss measurement of the fiber.

3.4 High Power Test Results of the Fiber

In this section, high power performance of the ultra-low NA fiber has been tested in a monolithic Master Oscillator Power Amplifier (MOPA) configuration. However, all of the possible loss sources such as the integration loss caused by the NA mismatch between the ultra-low NA active fiber and the output fiber of the pump combiner. Thus, I have intended to measure the mode field diameter (MFD) mismatch between the ultra-low NA fiber and the signal port of the pump combiner. Therefore, it can be said that the integration of these fibers is the most crucial part of this work since due to the NA mismatch between them some portion of the signal would be coupled to the cladding and hereby is lost in the Cladding Light Stripper (CLS). Theoretically, the ratio of power coupled to the cladding would be estimated based on the mode overlap between these two fibers and modal power distribution in them. In this case, the fibers have 0.034/0.06 NA values and 26 μm/20 μm core diameters respectively. To accomplish this, I have built a far-field measurement setup using angular scanning technique to estimate the MFD of fibers as shown in **Fig. 3.14**.

Based on the definition of MFD under Gaussian approximation, I have measured the angles at which the maximum intensity drops to the e^{-2} for both fibers and obtained 3.5° and 4.8° respectively. Thus the coupling ratio can be estimated as 72.9% by the small angle approximation; $\tan(\theta) \sim \theta$. In real case, I have 110

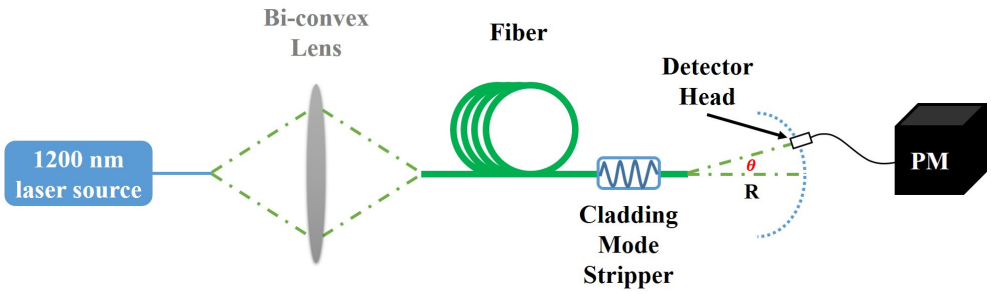

Figure 3.14: Schematic illustration of the mode field diameter measurement setup.

W signal power reaching to the power meter after the ultra-low NA active fiber. With the help of a CLS integrated to the end of this fiber I have measured the power as 80 W. Thus, the measured ratio would be 72.7% which is fairly close to the estimated one. Thereby, the signal power is going to be amplified in the amplifier stage is said to be 80 W. For that reason, since to build a laser oscillator system out of this fiber would be problematic and due to this fact, the experimental setup has been installed based on a MOPA system as sketched in **Fig. 3.15**.

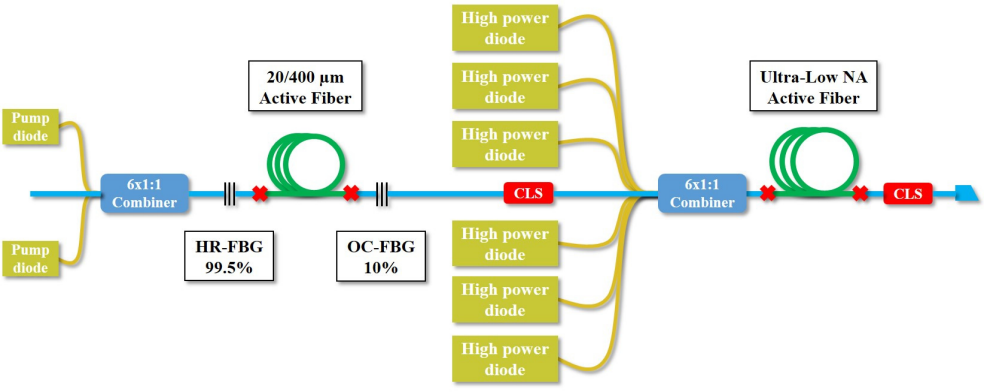

Figure 3.15: Schematic representation of the fiber MOPA system, HR-FBG, high reflective fiber Bragg grating; OC-FBG, output coupler fiber Bragg grating; CLS, cladding light stripper.

The system includes mainly two stages; one of them is oscillator in which the seed signal is produced and the other one is amplifier stage in which the signal coming from the seed is amplified to the high power levels. Firstly, the oscillator has been installed based on an Yb-doped active fiber having core and

cladding diameters of 20 μm and 400 μm, respectively. The oscillator stage has been completed with an FBG pair consisting of a high reflective FBG having a reflectivity of 99.5% and output coupler FBG having a reflectivity of 10%. Two pump diodes have been utilized in the oscillator stage as a pump source, and it has been integrated to a 6x1:1 pump combiner having 20 μm/400 μm fiber output. The total signal power produced at the end of oscillator after the CLS is $\approx$ 150 W. However, having passed through the 40 m long low NA active fiber, 110 W of this power is launched to the amplifier stage to be amplified. In this stage, the signal coming from the oscillator is amplified to the higher power levels by our 40 m long piece of fiber which has been pumped by six pieces of high power laser diode modules which are combined with a 6x1:1 pump combiner having an output fiber with core/cladding diameters of 20 μm/400 μm respectively.

Figure 3.16: The photograph of fiber coiling system, having 1 m diameter, taken with a cell phone while the laser is on showing the fluorescence in blue region.

For the sake visualization, the special coiling system designed for ultra-low NA fiber with 1 m bending diameter has also been shown as in **Fig. 3.16**. It should be noted that the photograph has been taken with a cell-phone and the emission is due to the fluorescence of Yb ions under high power 976 nm pump light. The average power of each high power diode module in the amplifier stage is around 250 W and so we had the total pump power of 1.5 kW. However, the unabsorbed pump power is around 180 W at this pump power level. This corresponds to the 88% pump absorption approximately by 40 m long active fiber and this suggests that fiber length would be enough to absorb adequate pump power.

Hereby, absorbed pump power can be calculated as 1320 W. Since the pure

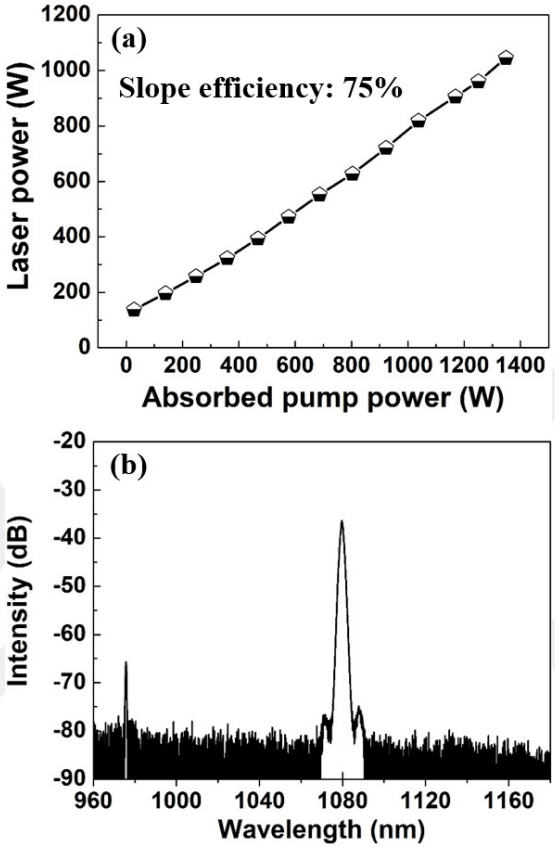

Figure 3.17: The power characterization of the ultra-low NA MOPA system up to 1.05 kW power level and (b) the optical spectrum at this power level.

laser power obtained after the CLS is 1050 W, the slope efficiency of this laser system based on the absorbed pump power might be calculated as 75%. According to the power characterization of the system 1.05 kW laser power is extracted in return for 1.32 kW absorbed pump power with a slope efficiency of 75% as sketched in **Fig. 3.17a**. With the help of CLS, the unabsorbed pump power level is dramatically decreased, and as shown in **Fig. 3.17b**, nearly 30 dB unabsorbed pump suppression is obtained. It should be also be added that the signal laser centered at 1079.66 nm was presented with a full width half at maximum (FWHM) of 1.64 nm. As can be seen, there is also no sign for Raman signal at this power level.

Additionally, I have also studied the output performance of our laser system in terms of temporal evolution, and no TMI occurs at this output power level as

well. In this system, I have altered the bending diameter of the fiber from 1 m to 2 m with 50 cm steps but no significant change observed in the performance of laser system. Therefore, I have decided to bend the fiber in 1 m diameter and all of the data presented above belongs to this bending diameter as shown in **Fig. 3.16**. After completing high power performance test of the fiber, finally, I have measured the quality of the laser at the maximum power level, which is 1.05 kW, by Thorlabs BP109-IR beam profiler and the data related is shown in **Fig. 3.18**. In addition to this, while the fiber is bent in 1 m diameter the beam profile image has been taken by using WincamD-UCD12-CCD beam profiler camera as shown in the inset of **Fig. 3.18**. The beam profile of the laser and the M^2 result, which is 1.11 in x-coordinate and 1.16 in y-coordinate, proves that the laser output has a good beam quality even at this large bending diameter.

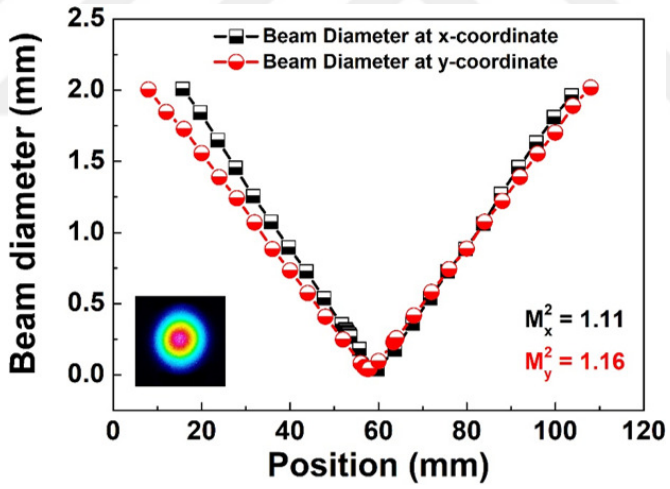

Figure 3.18: Beam quality measurement of the ultra-low NA fiber MOPA system above 1 kW power level. Beam profile image of the laser output (inset).

To conclude, in this study it has been showed that ultra-low NA fibers are promising for multi-kW excellent beam quality fiber laser systems and this goal can even be achieved in a monolithic fiber laser system as this whole work suggests. Though, the fabrication process of them is challenging since they are one of the most prominent solution to problem of the presence of non-linear effects specifically, TMI can be surpassed and the high-power high-quality fiber laser systems might be achieved based on these special type of fibers in near future.

Chapter 4

Color Center Observation in the presence of TMI

4.1 Introduction

Transverse mode instability (TMI) is another non-linear effect that dramatically affects the beam quality of the fiber laser systems. Unlike the others, the SRS and the SBS, TMI is a thermally driven effect inside the core region of the active fiber. However, on the other hand, TMI is also believed to be excited by another scattering-type, Stimulated Thermal Rayleigh scattering (STRS) [148, 149], resembling the SRS and SBS effects. There is no exact power threshold value for the TMI effect as in the case of the SRS and the SBS effect. On the contrary, this effect might be triggered at even low power levels depending on the birefringence and fiber design. TMI has recently been the critical power scaling limitation of the fiber laser systems. Therefore, the fiber laser community has focused on this new emerging effect, researching its origin and working on mitigating it. The primary mechanism of this effect can be summarized as in the following: the fundamental mode and the higher-order modes interfere with each other. Therefore, the energy switches between the modes, thus deteriorating the beam quality of the laser system. Non-linear coupled equations can also be performed to model

the interaction between these modes mathematically. To make a long story short, I have given detailed information on the literature survey for the TMI effect in the introduction section of this thesis.

4.1.1 Color Centers in Optical Fibers

To begin with, a conventional MCVD system has been utilized to fabricate Yb-doped active fibers. During the preform fabrication process, many chemical reactions take place between the elements inside the matrix; in our case, they are Silica (SiO_2), Aluminum (Al), Phosphorus (P), and Ytterbium (Yb). However, all of these chemical reactions do not end up with success within this complex system. The target reaction would be different than the achieved one depending on the content of the elements inside the chamber and the gas flow rate feeding up the system. Additionally, Alumino-Phospho-Silicate (APS) fibers, which have been fabricated, are based on the dominant material, SiO_2 inside the matrix in weight. Therefore, most of the defects are related to the interaction between the Silicon and Oxygen element. For example, some of the Si atoms do not interact with the oxygen atom to produce SiO_2 due to lack of inadequate oxygen flow in the system. Therefore, there have been oxygen deficiency defects as a result.

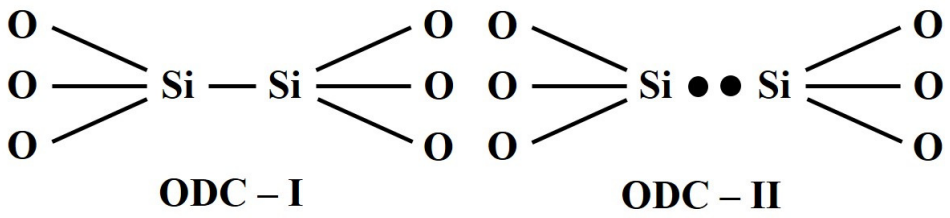

Figure 4.1: Schematic illustration of the chemical representations for ODC–I and ODC–II color centers.

These defects are called Oxygen Deficiency Centers (ODCs), and they are divided into two sections depending on the interactions. The possible defects resulting from the deficiency of the Oxygen atom have been illustrated in **Fig. 4.1**. There are two scenarios regarding the interaction between the Silicon and Oxygen atoms. The first one is that Silicon atoms can make bonds with each

other instead of Oxygen atoms. This defect is called ODC–I type color center. Another one is ODC–II, in which Silicon atoms cannot find any Oxygen atoms to form stable SiO_2 structure and thus resulting in two unpaired electrons, i.e., two dangling bonds for Silicon atoms [150–159].

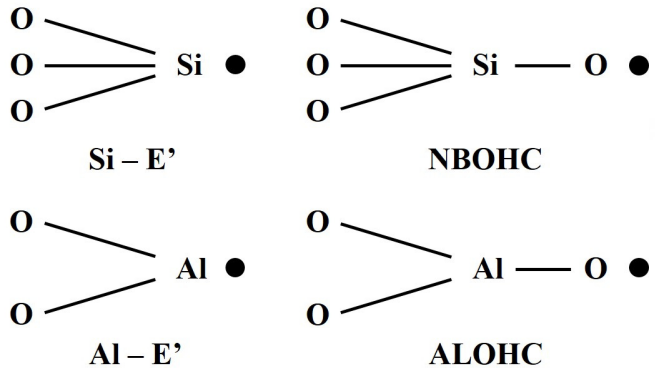

Figure 4.2: Schematic illustration of the chemical representations for E', NBOHC and ALOHC color centers.

Although the vast majority of APS fibers contain mostly SiO_2 inside and the other elements are the minority, there are also other color centers because of the defects resulting from the chemical bonds between them. Besides ODC, they can be classified as E centers (E'), Aluminum oxygen-hole center (AL-OHC) and non-bridging oxygen-hole center (NBOHC) [160–163]. The schematic illustration of the color centers, Si–E', Al–E', ALOHC, and NBOHC has been shown in **Fig. 4.2**. In brief, E' centers are the defects caused by the bonds established between the Silicon and insufficient Oxygen atoms. On the other hand, ALOHC appears when the weakly bonded electrons of the Oxygen atom are broken, and then the replacement of Al atoms with Si atoms occurs. Finally, NBOHC is one of the most popular types of the color center whose chemical representation has been shown in **Fig. 4.2**. It is a defect that Hydrogen atom in the construction of Hydroxyl turns into an ion. In the chemical representation, lines represent bonding Silicon atom to three Oxygens, and the black dot represents an unpaired electron, i.e., a dangling bond. These centers are highly localized, are optically active, and have luminescence near 1.9 eV and 2.0 eV corresponding to approximately 620 nm and 650 nm emission wavelengths, also known as R-centers or red centers [164–170].

$$Yb^{3+} + e^{-} = Yb^{2+} \tag{4.1}$$

There is another crucial phenomenon called photo-darkening, which inhibits the laser performance of the fiber dramatically. Photodarkening would affect the fiber severely depending on the concentration of the color centers formed inside the fiber. These so-called color centers have been created due to the electrons and holes excited inside the fiber. This process is purely related to the Yb^{3+} atom itself, in which it captures an electron and transforms to the Yb^{2+} ion as stated in **Eqn. 4.1**. This process is called Charge Transfer (CT), and it is believed to be the main reason for the photo-darkening effect. Because of this transformation, the active fiber loses the ability of absorbing the pump light and emit a laser signal. Instead, the energy is released as heat with a non-radiative transition rather than laser radiation [171–177]. I have intended to investigate the color center formation inside homemade self-fabricated LMA Yb-doped active fibers in the light of this information. Furthermore, I have also questioned the relationship between the TMI effect and the color center formation mechanism inside the fiber with a unique setup sustaining the TMI effect.

4.2 TMI Analysis of the Fiber Laser System

As explained in the previous section, I have built a special amplifier system to guarantee the presence of the TMI effect. To do this, I have benefited from the higher-order-mode content of the LMA fiber. The fiber laser system was rebuilt by implementing a different fiber cooling system with varying bending diameters from 36 cm to 14 cm with a helix design instead of a cylindrical one. The real image of this helical fiber cooling system is shown as in **Fig. 4.3**.

The reason behind this is to present the onset of the TMI effect benefiting from the fact that LMA fibers could transmit a few modes depending on their V numbers. Therefore, they need to be bent to suppress the higher-order modes

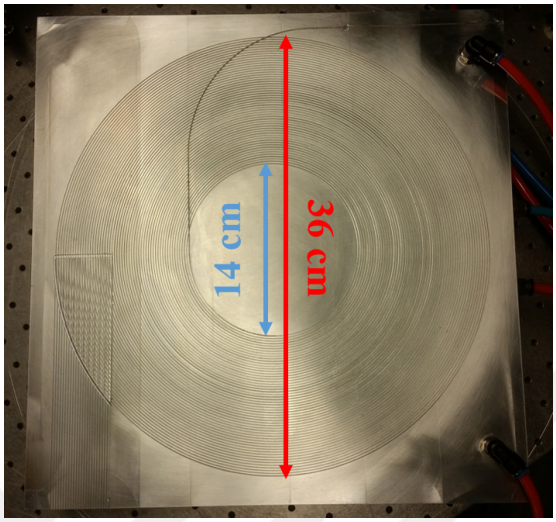

Figure 4.3: The picture of the fiber cooling system having helical design.

to sustain the fundamental mode operation of the fiber for the sake of the high-quality laser output. It means that if the fiber is not bent enough, higher-order modes survive in the system. And thus, after a particular pump power threshold value, interference between the fundamental mode and the higher-order modes occurs to cause the so-called TMI effect and degradation of the beam quality and beam profile of the laser output.

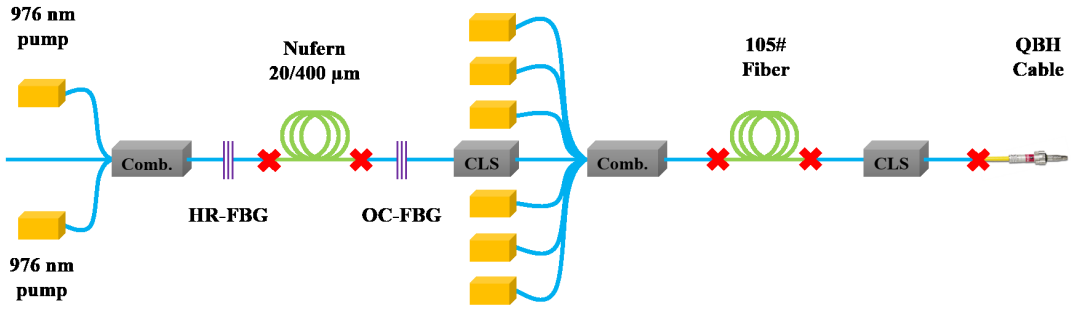

Figure 4.4: The schematic illustration of the laser system in the MOPA configuration, Comb., Combiner; HR-FBG, High reflective fiber Bragg grating; OC-FBG, Output coupler fiber Bragg grating; CLS, Cladding light stripper; QBH, Quartz block head.

The fiber laser system has again been configured as Master Oscillator Power Amplifier (MOPA) design as illustrated in the **Fig. 4.4**. Two pump diodes have been utilized in the oscillator section, based on a commercial active fiber with

20 μm/400 μm core/cladding diameters. In contrast, six pieces of them have been utilized in the main amplifier section of the system. The oscillator has been operated at 1080 nm central wavelength with the help of the fiber Bragg grating (FBG) pairs. However, in the main amplifier section, 25 m-long self-fabricated 105# fiber has been utilized to amplify the signal coming from the oscillator section of the laser system. I have first characterized the laser system in terms of the power, optical spectrum, and beam quality, which will give us information about the TMI effect.

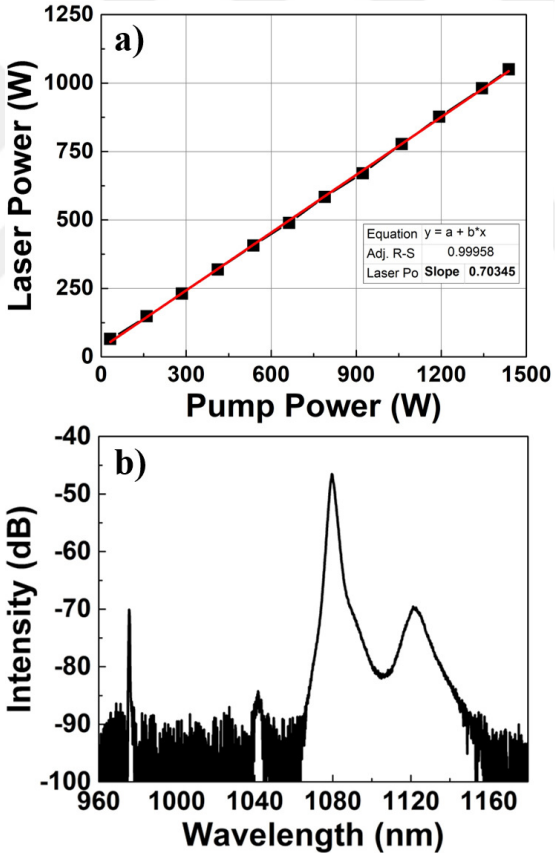

Figure 4.5: (a) The power characterization of the laser system at up to 1 kW power level and (b) the optical spectrum of the laser system at 1 kW power level at logarithmic scale.

To begin with, power characterization of this MOPA laser system has been performed up to nearly 1 kW power level with a slope efficiency of 70%, as shown in **Fig. 4.5a**. The oscillator of this system has a 45 W power level, and this much of the power has been amplified to a 960 W power level by pump sources with

1400 W pump power. The optical spectra of the laser system have also been taken while the system has been operating at its maximum power level, which is 960 W in both logarithmic and linear scales, as sketched in **Fig. 4.5b**. As can be seen clearly from **Fig. 4.5b**, both the unabsorbed pump and the Raman suppression are above 20 dB, and thus this proves optimum fiber length has been utilized in this system. The beam quality measurement, which is the most important one in this specific study, has also been performed at different power levels of this laser system to monitor the change in the M^2 values, so to speak, the beam quality. Based on the design of the fiber coiling system, the TMI effect initiates after 700 W pump power level, and the M^2 values of the laser system start from 1.2 and reach up to nearly two at the maximum power level of the system, as can be seen clearly from the **Fig. 4.6a**.

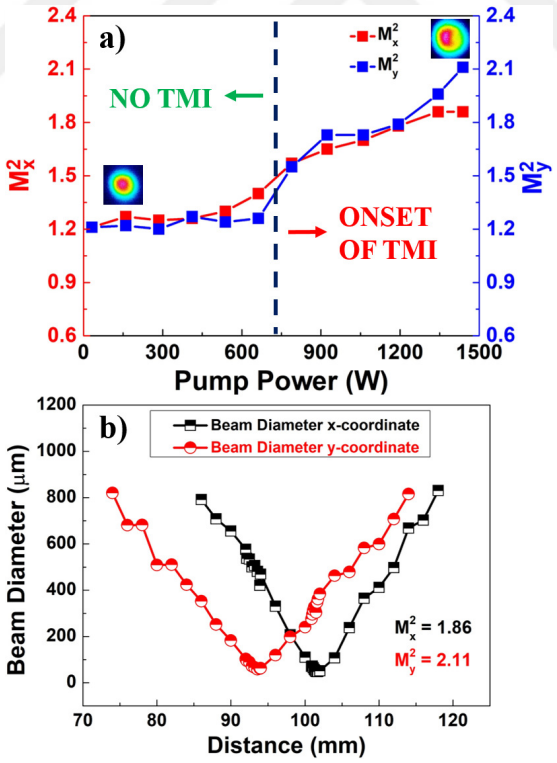

Figure 4.6: (a) The beam quality (M^2) values of the system versus pump power level at both x and y coordinates with the beam profiles (inset) and (b) the beam quality (M^2) measurement data at the maximum power level of the system at both x and y coordinates.

As an illustrative example, the change in the beam profile of the laser system

at both 200 W and 1400 W pump power levels can easily be seen comparatively in the inset of **Fig. 4.6a**. Not only the M^2 value but also the beam profile of the laser system degrades when the TMI presents. As mentioned above, the presence of HOMs and interaction with the fundamental mode is the main factor to trigger the TMI effect. The M^2 values of the laser system start with 1.2 and continue at this level up to a certain point. After achieving the threshold of the TMI effect, it keeps increasing up to 2.1 as an average, as illustrated in **Fig. 4.6a**. The comparison of the beam profiles of the laser system at both 200 W and 1400 W pump power levels respectively inset of the figure. As can be seen clearly, the beam profile has also been distorted due to the onset of the TMI. What it means is that the presence of the HOMs has increased in a considerable amount in time. I have taken M^2 measurement at the maximum power level of the system to quantify this distortion and obtained 1.86 and 2.11 at x and y coordinates, respectively, as shown in **Fig. 4.6b**.

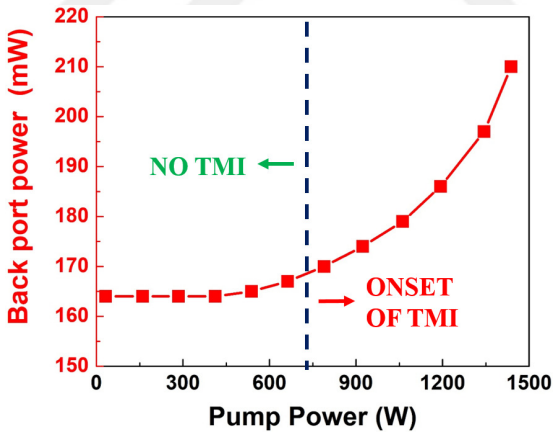

Figure 4.7: The power characterization of the back port of the laser system versus pump power.

The onset of the TMI can also be observed from the back output port of the laser system due to the nonlinear interaction between the fundamental (LP_{01}) and higher-order modes, especially (LP_{11}) by the interference of the counter-propagating mode pairs [166]. Similarly, I have also characterized the back-port output of this laser system to monitor the effect and the onset of the TMI. In the normal condition, the back-port of a laser system is supposed to be constant for a stable laser operation. Around 700 pump power level, back-port output

power starts to increase exponentially up to a certain level depending on the laser system itself as shown in **Fig. 4.7**. This data also agrees well with the M^2 values since the degradation of the M^2 values starts to degrade around 700 W pump power level as well.

4.3 Red Probe Laser Experiment in the Presence of the TMI

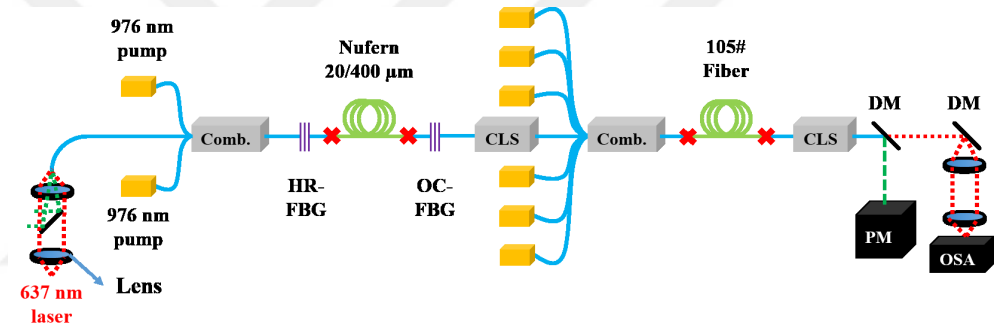

Figure 4.8: The schematic illustration of the laser system in the MOPA configuration with red probe laser, Comb., Combiner; HR-FBG, High reflective fiber Bragg grating; OC-FBG, Output coupler fiber Bragg grating; CLS, Cladding light stripper; DM, Dichroic mirror; PM, Power meter; OSA, Optical spectrum analyzer.

After TMI analysis of the laser system, I have intended to benefit from the refractive index change (RIC) of the self-fabricated active fiber during the high power operation indirectly by measuring the intensity change of a laser probe signal. The purpose and motivation of this experiment are to monitor this change all over the laser power change. Therefore, I would establish a relation between this RIC to the TMI effect based on the data. Having motivated, I have utilized a laser source as a probe signal with a free space orientation for coupling to the system for that purpose. The laser probe used in this system is Thorlabs S1FC635 operating around 637 nm wavelength range with a maximum output power of 2.5 mW. A lens pair has been used to collimate and focus the 637 nm laser signal into the fiber, as shown in **Fig. 4.8**. Besides, a laser mirror operating around 1070 nm has been utilized in the middle of this system to prevent back-scattered

210 mW, 1080 nm laser signal as plotted in **Fig. 4.7**. On the other hand, I have implemented another free space-oriented part to eliminate the 1 kW 1080 nm laser light and extract to 637 nm laser signal at the end of the laser system. For that purpose, a high-power mirror having 99.9% reflectivity has been used, as sketched in **Fig. 4.8**. Then, a lens pair again has been used to couple the 637 nm laser light into the fiber input of the Ocean Optics HR4000CG-UV-NIR high-resolution spectrometer working between 200 nm and 1100 nm wavelength range.

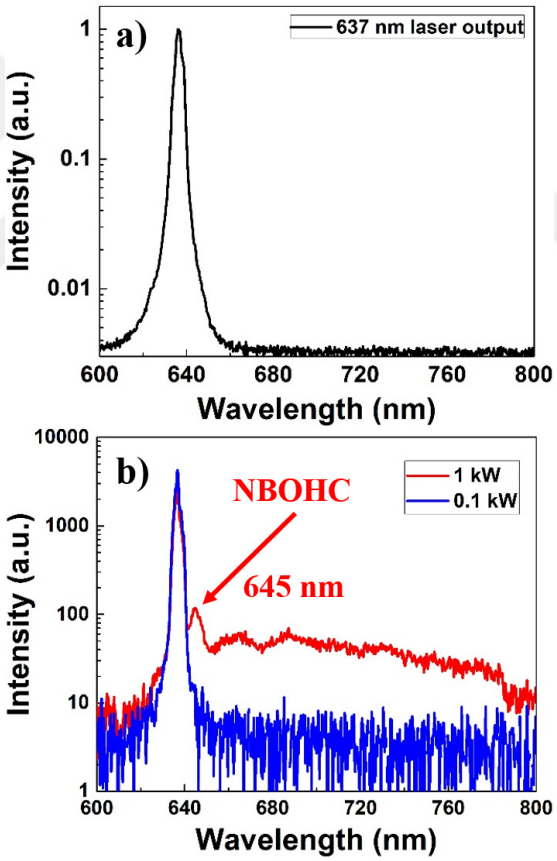

Figure 4.9: (a) The optical spectrum of the 637 nm laser source from direct output and (b) the optical spectra from the output of the laser system taken with spectrometer at two different power levels.

In this study, the motivation is to monitor the change in the spectrum of the 637 nm laser signal throughout the pump power change, and based on this data, the difference in the RIC of the self-fabricated fiber would be estimated especially on the TMI zone to establish a relation between them. First of all, I have taken

the optical spectrum of the 637 nm laser source as a reference, and the data obtained has been shown in **Fig. 4.9a** in the logarithmic scale.

On the other hand, I have also recorded the intensity change of the red probe laser versus pump power. As a comparison, the plot of optical spectra, in the range between 600 nm and 800 nm as the same as the spectrum of the laser source, at two different laser power levels, namely 100 W and 1 kW, is shown in **Fig. 4.9b**. I have chosen these two power values; one is nearly minimum the other is the maximum power of the laser system to show the optical spectra difference better. The relation between the laser power and the optical spectrum change is linear, so to speak, the optical spectrum keeps changing increasingly while the laser power increases. Additionally, I have also observed one of the so-called color centers formed inside the fiber, none bridging oxygen-hole centers (NBOHCs), corresponding to the emission of 645 nm wavelength as indicated in **Fig. 4.9b**.

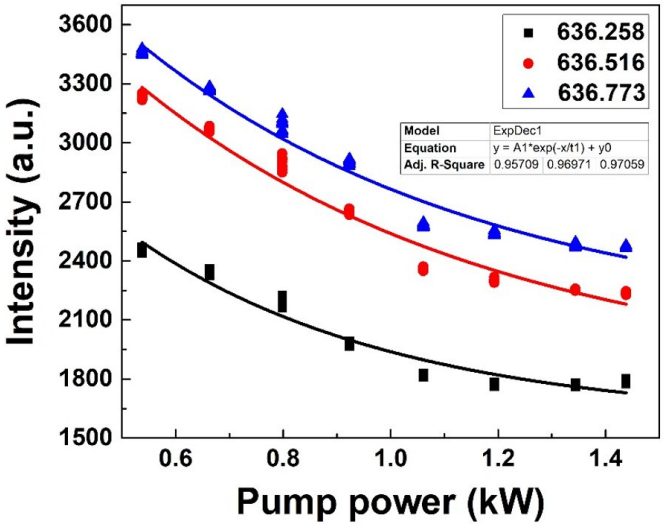

Figure 4.10: The intensity change of three different chosen wavelength of the 637 nm laser source versus pump power.

From benefiting the spectrum change shown in this figure, three wavelengths have been explicitly examined to illustrate the intensity change in the probe laser throughout the laser system's pump power change, including the TMI zone. These three wavelengths have been chosen near the central wavelength of the 637 nm laser probe signal. As a result, I have observed an exponential relation between

the intensity of the probe signal and the power of the laser system, as shown in **Fig. 4.10**. I propose that the exponential decay is related to the RIC of the fiber, caused by an increase in the temperature of the fiber core area. This process is called thermal lensing in the literature. Due to this temperature change, the index of the central part increases at a rate higher than the other parts, resulting in a non-uniform change in the fiber's refractive index. This thermal-optic effect is introduced by **Eqn. 4.2** below:

$$n(r) = n_0(r) + k_T \Delta T(r) \tag{4.2}$$

where refractive index profile n, initial refractive index profile n_0 and change in temperature ΔT are expressed in cylindrical coordinates, and $k_T = 1.1 \times 10^{-5}\mathrm{K}^{-1}$ is the thermal-optic coefficient for silica [100, 164].

4.4 Green probe laser experiment

After examining the intensity change of the red probe laser, I have decided to repeat the same experiment with a different probe laser source to prove the independence of this behavior from the probe laser wavelength. For that purpose, I have utilized a green laser source operating at a 520 nm central wavelength region with a 300 mW maximum output power. However, this time the source is more powerful but has multi-mode output. This multi-mode behavior will bring extra transmission loss due to the long and complex structure of the high power amplifier system. Still benefiting from the power of the probe laser with a suitable free-space arrangement, this shortcoming can be compensated.

4.4.1 GPL experiment in the presence of the TMI effect

As mentioned above, I have utilized an Elite Optoelectronics RG-600FC branded green probe laser operating at 520 nm central wavelength for this experiment.

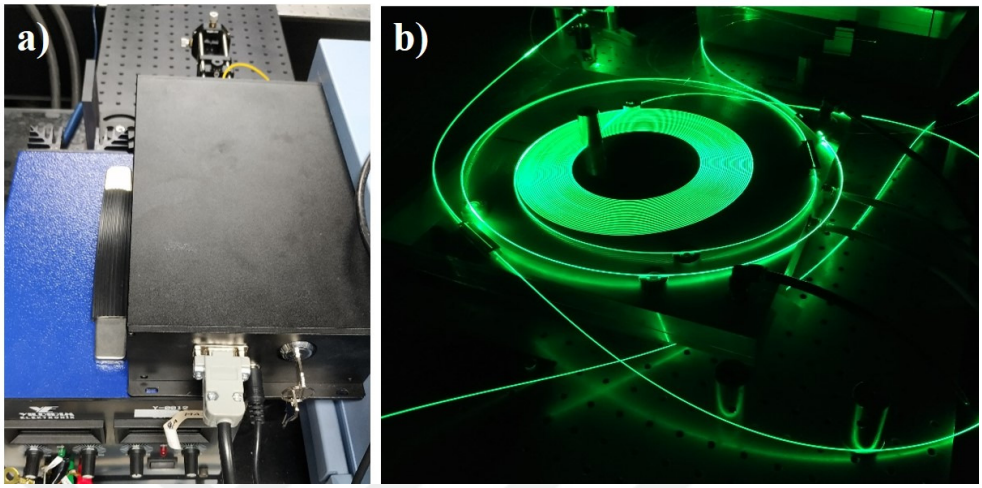

Figure 4.11: (a) The photograph of the green laser source and (b) the picture of the fiber while transmitting the green probe laser.

The photograph of this probe laser has been shown in **Fig. 4.11a**. Additionally, after certain free-space alignment, including two lenses, explained in detail in the previous section, I have coupled the probe light into the fiber laser system. To illustrate, I have taken a picture of the fiber laser system while the probe laser propagates inside as shown in **Fig. 4.11b**. Before the experiment, I have first characterized the green probe laser to examine the external effects on the intensity change, such as the cooling water's temperature of the fiber laser system.

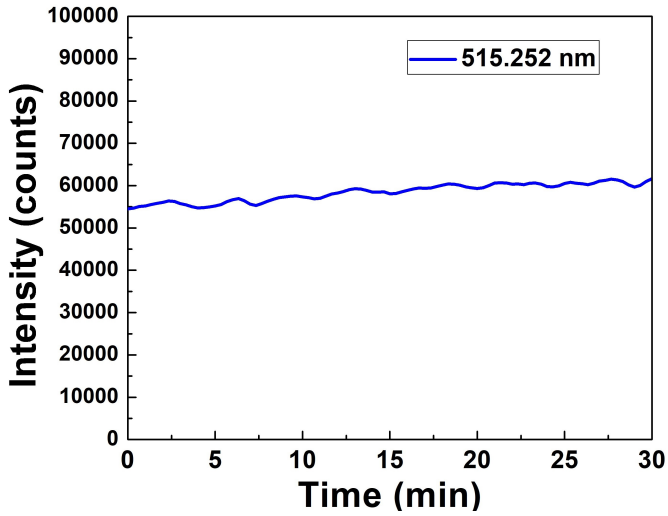

Figure 4.12: Power stability characterization of the green probe laser during 30 minutes.

For that purpose, I have observed the impact of the temperature change of the cooling water varying between 18°C to 22°C. In between these temperatures, the probe laser has behaved the most stable in the gap between 21°C to 22°C. Therefore, this experiment has been conducted for over 30 minutes while the cooling water temperature rose from 21°C to 22°C. During this period, the green laser's intensity slightly increased from 55000 to 60000 counts. Thus, the light intensity is 57500 ± 2500 between these temperatures. The data belonging to this experiment has been plotted in **Fig. 4.12**.

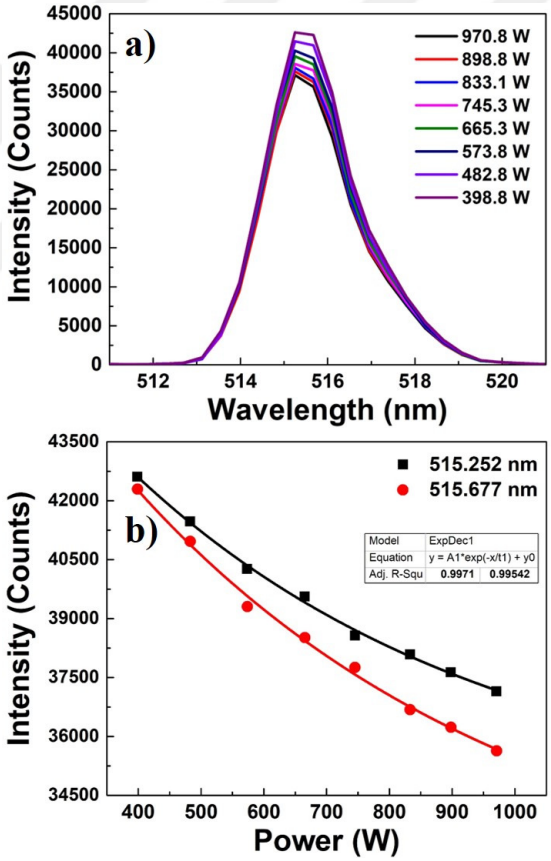

Figure 4.13: (a) The optical spectra of the green probe laser and (b) the intensity change graph of two selected wavelengths vs. laser power in the TMI region.

Considering this information, I have decided to conduct the green probe laser's intensity change experiment in this interval to minimize the error in the experimental data. After this stability test, I have performed this experiment by increasing the laser power from 0 to maximum power level, 1 kW, and plotted the

optical spectra, especially on the TMI region, as shown in **Fig. 4.13a**. Additionally, the intensity change of the two-wavelength selected with maximum intensity has been plotted versus the laser power, as shown in **Fig. 4.13b**. In summary, I have observed the same trend as the one in the previous report for the red probe laser. The exponential decay fit has been applied to this data, and 0.9971 and 0.99582 of the R^2 values have been obtained, respectively.

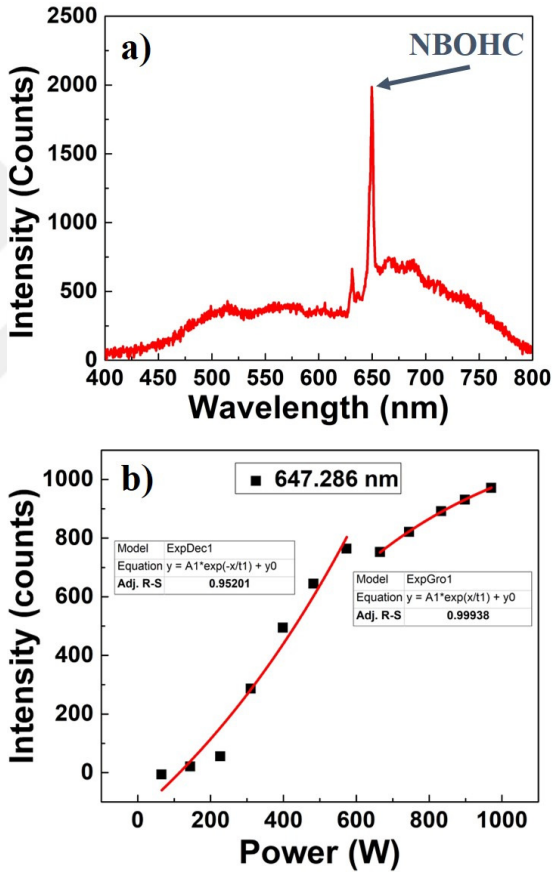

Figure 4.14: (a) The optical spectrum showing NBOHC color center formation inside the fiber at 1 kW output power level and (b) the intensity change in the NBOHC signal versus laser power.

Just as a reminder, a phenomenon called color center is created inside the fiber's core region due to the formation or breaking up of the chemical bonds between the SiO_2, Al, P, and Yb elements in this case. As explained in the previous section, I have observed one of them: none bridging oxygen-hole centers (NBOHCs), whose emission corresponds to the wavelength around 645 nm, most dominantly. The optical spectrum belonging to the NBOHC color center has

been taken while the laser operates at the maximum output level, 1 kW, as shown in **Fig. 4.14a**. I am supposed to note that this spectrum belongs to the fiber operated for tens of hours and thus exhibits a cumulative behavior. This fiber will be compared with a new fiber to elaborate on the difference in the next section. I have also recorded the NBOHC signal intensity in return for the laser output power and plot the graph, as shown in **Fig. 4.14b**.

There is an exponential growth trend up to 600 W power level, corresponding to the beginning of the TMI effect for this laser system. After the TMI threshold, the signal follows a different exponential growth pattern with an R^2 value close to 1. This information is a clue for the connection between the TMI effect and the color center formation mechanism. However, this data needs to be verified with a scheme without the TMI effect. This experiment will also be done in the next section.

4.4.2 GPL experiment without the TMI effect

In the previous case, I had coiled a 25 m piece of 105# homemade self-fabricated active fiber with helical structure cooling apparatus with a larger bending diameter to sustain the existence of the TMI effect due to the survival of the higher-order modes (HOMs). Additionally, several optical characterizations have been performed, including beam quality measurement, to support the existence of the TMI effect.

After that, I studied the relation between the TMI effect and the color center formation under the high-power laser operation. The results obtained belonging to the experiments with the TMI effect have been shared above. However, in this case, I have coiled a 25 m piece of pristine 105# active fiber and repeated the same experiments without the TMI effect to explore any difference between these two cases. The real photograph of the cylindrical cooling system, utilized with a 10 cm bending diameter to get rid of the TMI effect, has been shown in **Fig. 4.15a**. In addition, the thermal camera image of the cylindrical cooling system has been taken during the laser operating at its maximum power level, 1 kW, as

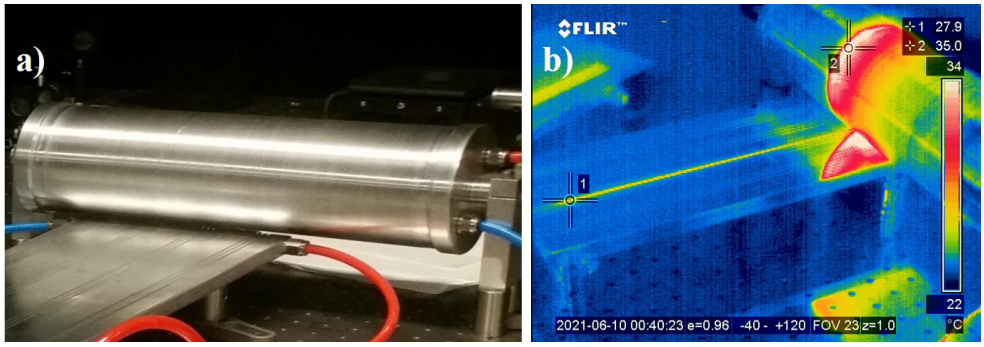

Figure 4.15: (a) The real photograph and (b) the thermal camera image of the active fiber coiled at 10 cm diameter with a cylindrical cooling system to get rid of the TMI effect at 1 kW power level.

shown in **Fig. 4.15b**. In the picture, there is also a flat cooling plate to cool both the splicing point and the first part of the active fiber. Finally, the maximum temperature on the fiber is recorded as 35.5°C at the 1 kW output power level.

After the characterization of the revised system without the TMI effect, the optical spectra of the Green probe laser have been recorded and plotted versus laser power, as shown in **Fig. 4.16a**. The intensity of the probe laser decreases as the laser power increases, as shown in **Fig. 4.16b** as in the previous case. For comparison, I have plotted the two wavelengths, 515.252 nm and 515.677 nm, versus the laser power with R^2 values of 0.99688 and 0.99632. Although they exhibit the same behavior, the rate of the total intensity change for without the TMI effect case is more than the other one. The reason behind this tighter bending diameter (10 cm) of the active fiber is the refractive index distortion of the fiber with this bending. That situation, thus, provides additional transmission loss for the green probe laser. It can be concluded from this study that there is no direct relation between the TMI effect and the intensity change of the probe laser. In other words, no direct impact of the TMI effect had been observed on the refractive index change of the fiber since similar results have been obtained from the two experiments based on with and without the TMI effect configurations.

After the green probe laser experiment, I have measured the signals coming from the color centers in this new configuration for comparison. I have taken the optical spectrum of the NBOHC color center with this new piece of fiber, and the

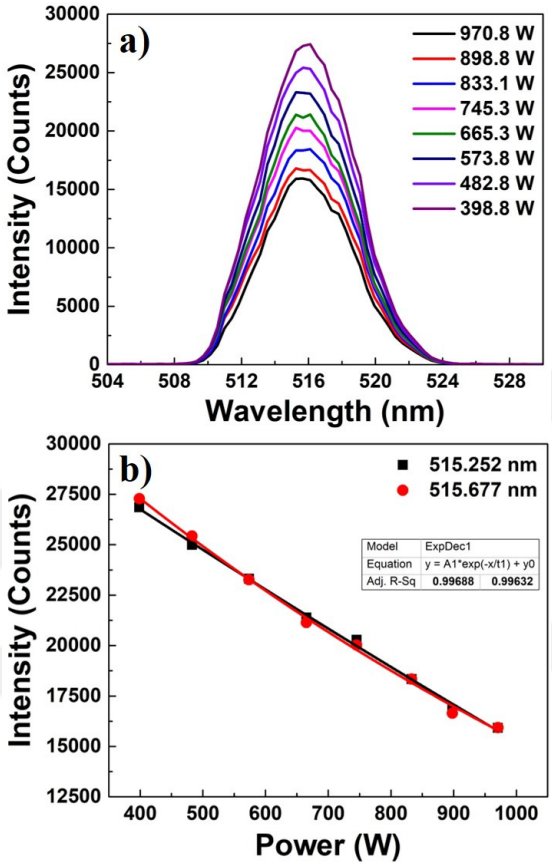

Figure 4.16: (a) The optical spectra of the green probe laser and (b) the intensity change graph of two selected wavelengths vs. laser power for comparison.

spectrum has been sketched for without the TMI effect case, as shown in **Fig. 4.17a**.

For comparison, the peak wavelength of the NBOHC color center has also been detected as 647.286 nm with an Ocean Insight Flame Miniature model spectrometer. The intensity change of this wavelength has been recorded versus laser power and plotted as in **Fig. 4.17b**. The graph shows a gap around the 500 W power level, which resembles the graph obtained in the previous case. Likewise, the slope of the graph also changes beyond this power level. However, this situation is also most probably due to temperature-driven effects. Therefore, I have attained the same trend from two experiments with and without the TMI effect cases. And thus, the gap created around 500-600 W power level is not due to the TMI effect.

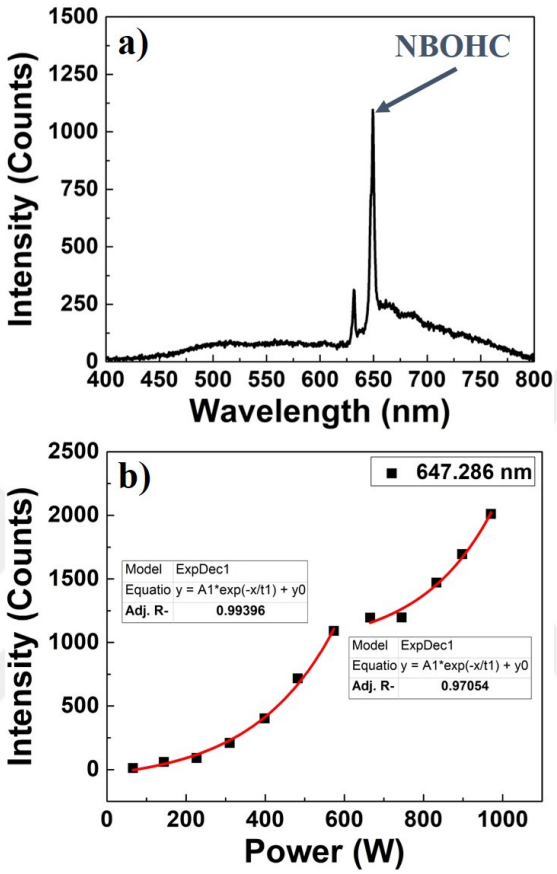

Figure 4.17: (a) The optical spectrum showing NBOHC color center formation inside the fiber at 1 kW output power level and (b) the intensity change in the NBOHC signal versus laser power for the pristine fiber.

Besides NBOHC color center, I have also observed the cooperative luminescence (CL) phenomenon during the experiments. Just as a reminder, the background of green luminescence of Yb^{3+} around 500 nm was explored in 1970 and determined as photon emission by a pair of excited ions in cooperation. Another vital piece of information about CL is that it could contribute to the Photodarkening (PD) effect through the color center formation [177]. CL could be influenced by the increase in Yb^{2+} and provide insight into the PD mechanism as explained in the previous section in detail. To emphasize the impact of the laser operation time on the color center intensity change, I have plotted both spectra belonging to both cases on top of each other for comparison.

In brief, I have observed an obvious difference between the used fiber and the

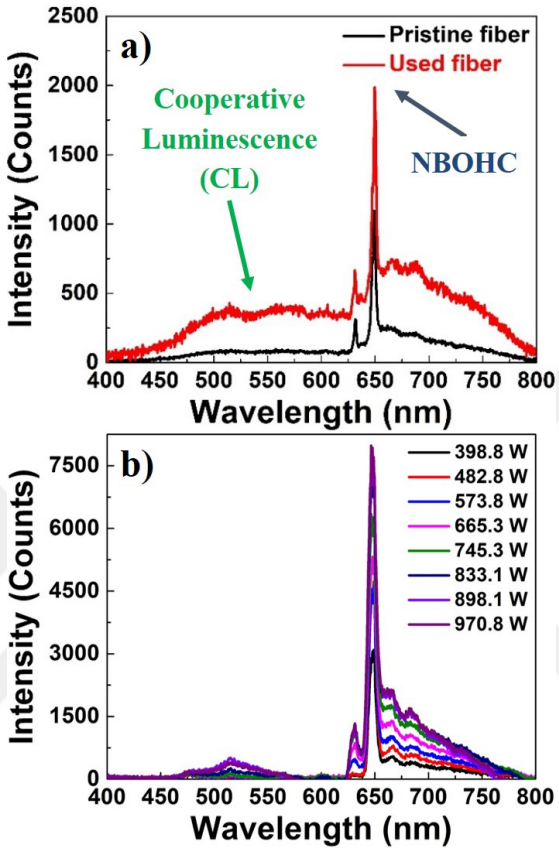

Figure 4.18: (a) The comparison of the pristine and the used fiber in terms of NBOHC color center and CL signal and (b) the evolution of the NBOHC signal for the pristine fiber versus laser power.

pristine one as shown in **Fig. 4.18a**. It is important to note that not only CL but also NBOHC color center signal increases in time. Additionally, I have also taken the color center spectra belonging to power levels between 400 W and 1 kW to illustrate the increase in the color center signal as shown in **Fig. 4.18b**.

As mentioned earlier, there is a relation between CL and CT (**Eqn. 4.1**), responsible for the Photodarkening effect inside the fiber. This effect appears more dominantly while the laser operation time increases as observed in the previous study. Beside CL is present under 915 nm and 975 nm pump radiation exposure, it also presents under UV excitation [172]. Therefore, I have decided to support the CL data shown in **Fig. 4.18a**. For that purpose, I have exposed both used and pristine versions 105# fiber to a UV laser operating 325 nm wavelength. As a result, I have obtained the data and sketched it as illustrated in **Fig. 4.19**.

As expected, CL signal of used fiber is five times greater than the pristine one and it is consistent to the data given in the previous figure. Both spectra proves that while the laser operation time passes more CL signal is attained and so the Photodarkening effect is more dominant.

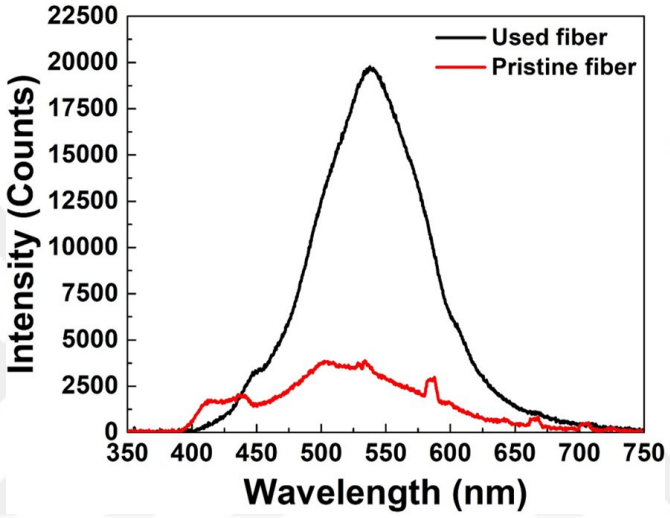

Figure 4.19: (a) The UV excitation result of both used and pristine 105# fiber.

To sum up, in this study, I could not establish any organic relation between the TMI effect and the color center formation; however, I have observed the Photodarkening effect and analyzed NBOHC color center formation versus the laser power. Also, the pristine and the used versions of the same fiber have been investigated concerning the color center formation mechanism inside them based on home-made Yb-doped active fiber.

Chapter 5

Side-Pump Combiner Fabrication in (1 + 1) x 1 Configuration

5.1 Introduction

Fiber laser oscillator and amplifier systems consist of critical components, i.e., semiconductor diode lasers, pump combiners, fiber Bragg gratings (FBGs), and active fiber. One of the crucial components is pump combiners utilized to combine multiple high-power diode lasers' power into one output fiber to maintain the monolithic structure of the fiber laser systems. Pump combiners are divided into two concerning the existence of the signal fiber. One is composed of pure pump fibers, and the other, along with the pump fibers, also includes a signal fiber called a combiner with signal feed-through [178–184]. Regardless of the signal fiber's existence, the most popular fabrication technique of the pump combiners is the fused tapered fiber bundle (TFB) for end-pump configuration. The only difference is that the pump and the signal fiber are tapered together for the pump combiner with signal feed-through. However, since the whole fibers, including the signal fiber, are tapered in the end-pump configuration, the pumping can

only be achieved in one direction. Therefore, this situation results in the non-homogeneous thermal load on the active fiber, decreasing the threshold for non-linear effects in the fiber laser system. But, recently, it has been demonstrated that counter-pumping or bi-directional pumping mechanisms allow the power to scale up, providing higher non-linear interaction thresholds by homogenizing the thermal load on the active fiber. The non-linear interactions fed on the thermo-optical effects are mainly Stimulated Raman Scattering (SRS) and, most recently and notably, Transverse Mode Instability (TMI). This effect is present due to the interactions between the fundamental and higher-order modes (HOMs). It thus reduces the quality of the laser beam drastically, as explained in the previous chapter of this thesis.

As a solution to these problems, an alternative to the end-pump technique has been proposed to make both counter pumping, and bi-directional pumping possible is the side pump coupler technique. The fiber core remains uninterrupted [185–187], and there is no restriction for the number of the pump ports [188], thus providing more freedom than the other one. There are several techniques on the side pump combiner fabrication published in the literature, such as the V-groove technique [189], the embedded-mirror method [190], angle-polished pump fiber technique [191, 192], and fused tapered method [193, 194]. This method is based on a direct fusion of one or several tapered pump fibers to the surface of a signal fiber. In that respect, this method is promising because of its high coupling efficiency and handling high pump power up to kW-class.

5.2 On a Home-Made Photonic Cyrstal Fiber

I have followed the direct fusion method to fabricate the side pump combiners since it allows high power operation with a high pump coupling efficiency. This method consists of two consecutive steps. The first one is to taper the pump fiber adiabatically to sustain the guidance of the pump light in the pump fiber while the diameter of the fiber decreases. After then the tapered pump fibers are fused to signal fiber horizontally to accomplish the side coupling by fusion

splicing. The schematic representation of a side pump combiner in a (1 + 1) x 1 configuration has been shown in **Fig. 5.1** for the sake visualization.

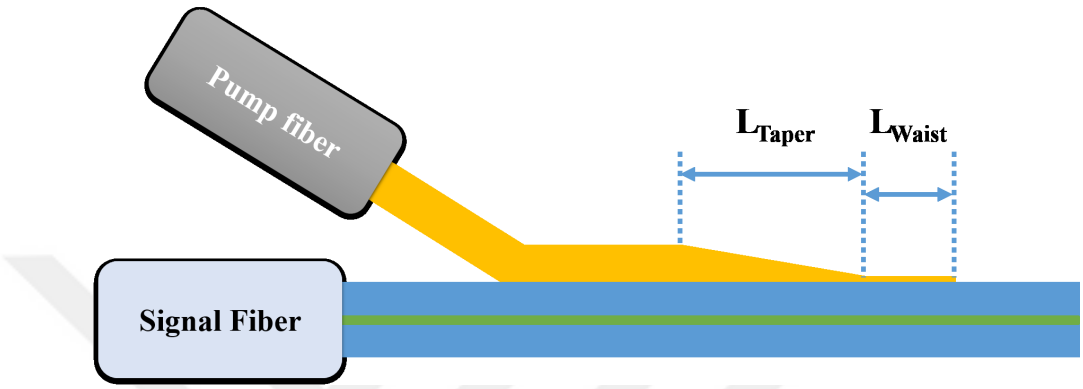

Figure 5.1: Schematic representation of a side pump combiner in (1 + 1) x 1 configuration.

Several critical parameters determine the quality and pump coupling efficiency of the side pump combiner: taper length, waist length, and the waist diameter of the taper. Both the taper process and the fusion splicing have been performed by Fujikura LAZERMaster LZM-100 glass processing system, whose photograph is shown in **Fig. 5.2**. Additionally, all of the parameters mentioned above can be highly controlled by this equipment as well. The so-called glass processing system has an embedded CO_2 laser inside with a 10.6 μm central wavelength and 30 W maximum output power. The reason why a CO_2 laser has been utilized in this system is that the absorption of SiO_2 material is at the maximum level between the 8 μm–10 μm wavelength regions [195]. In this region, there is only one laser system readily available is CO_2 laser. Additionally, all of the fibers that I have been dealing with are aluminophosphosilicate fibers. It is also a general fact that the vast majority of these fibers consist of SiO_2 material. SiO_2 has a tetrahedral structure, Silicon (Si) atom in the center bonded to 4 Oxygen (O) atoms. The absorption phenomenon occurs due to the interaction of the CO_2 laser and the Si – O bond. The dihedral angle between two Si – Si bonds (tetrahedron angle) is 109.5° and the angle formed by the Si – O bonds in the Si – O – Si bridge is 144° [196].

CO_2 laser source has a 4 mm beam diameter and is divided into two parts via a beam splitter to radiate the fiber from two axes. This feature provides

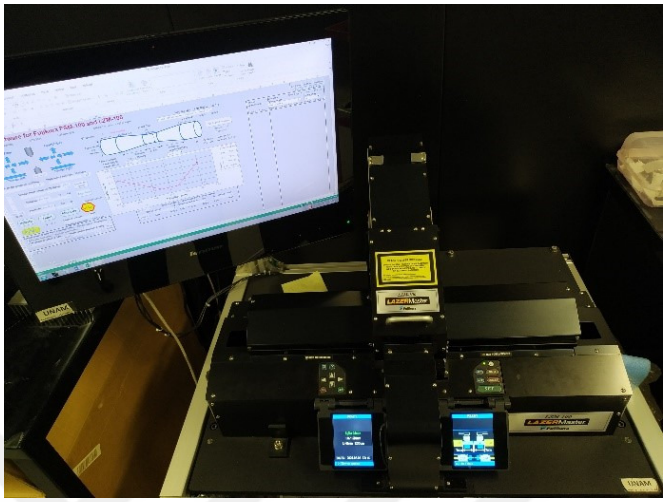

Figure 5.2: Fujikura LZM-100 LAZERMaster glass processing system.

homogeneous heat distribution along with the fiber. This machine is also capable of rotation besides horizontal movement with a micron size precision and has 15 cm maximum stage movement capability.

5.2.1 Taper results of the pump fiber

As a first step for the side pump combiner fabrication, I have tapered a 130 μm cladding diameter pump fiber to 30 μm and 45 μm taper waist diameters, respectively, with taper lengths of 50 mm and 70 mm for comparison. However, 70 mm taper length has been utilized to produce side pump fabrication in this study. Before working with the LZM-100 glass processing machine, the CO_2 laser model requires a warming-up process for the sake of stability, and this situation is also a general procedure for all laser systems based on any gas.

Another critical step needed after the warming up process is the power calibration to scale the necessary power to taper. This process has generally been completed with a fiber sample having 125 μm cladding diameter. In this process, the machine operates and gradually increases the laser power until the fiber's melting temperature. At this point, the power level corresponding to the melting point of the fiber is recorded as a reference laser power level during the whole

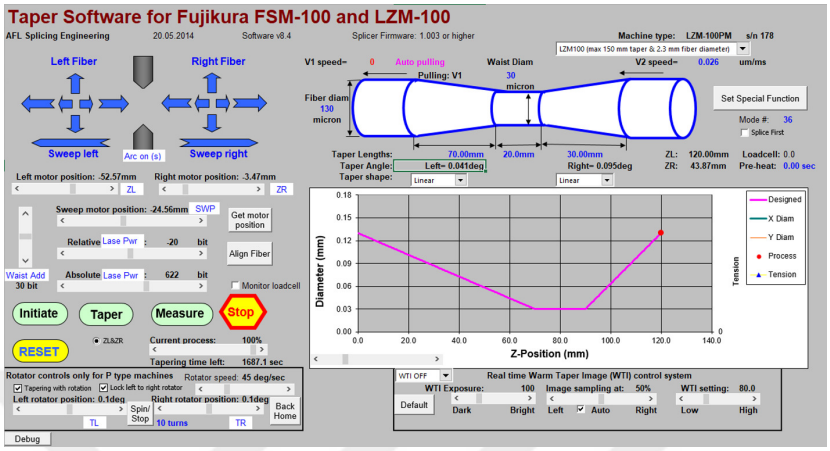

Figure 5.3: The interface of the software of the LZM-100 glass processing system.

experiment. As a piece of additional information, this process must be repeated in a maximum of six months. The power calibration process has ended with a 622-bit value corresponding to a power level of 9.75 W for this specific fiber. This number will be a reference power level throughout this study, and it will be arranged accordingly. In the taper software program, 622-bit laser power value is accepted as absolute laser power parameter from now on, as can be seen from the **Fig. 5.3**. The other parameters that can be altered via this software are taper lengths, waist diameter, pulling speed, relative power, waist add power, and rotator speed.

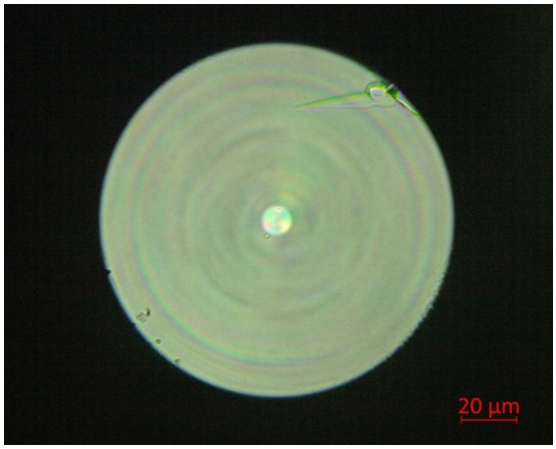

Figure 5.4: Optical microscope image of the cross-section of the pump fiber having 130 μm cladding diameter with 50x objective in Dark Field (DF) mode.

All of these so-called parameters have been optimized for the fiber having 130 μm cladding diameter whose optical microscope image of the cross-section has been shown in **Fig. 5.4**. As mentioned briefly above, the 130 μm cladding fiber has been tapered to two different taper waist diameters and taper lengths for comparison. The chosen parameters are 30 μm and 45 μm for taper waist diameter and 50 mm and 70 mm for taper length. First, the pump fiber tapered to 30 μm taper waist diameter corresponds to a taper ratio of 4.33. Then, I have tapered the pump fiber to 45 μm taper waist diameter, corresponding to a taper ratio of 2.89.

For the taper ratio of 4.33, I have optimized the power of the CO_2 laser to STD-20 bit (9.4 W) and the pulling velocity as 0.02 μm/ms for 50 mm taper length. Waist add-power has also been arranged as 30 bit to sustain the waist diameter to achieve the desired diameter. The rotation speed has also been set to 45°/s for all the tapers and has never been changed during the experiments. The parameters have been kept the same other than the pulling speed since taper length increases from 50 mm to 70 mm. However, I have slightly increased the pulling speed from 0.02 μm/ms to 0.026 μm/ms for the sake of saving some time during the taper process since while the pulling speed is low, it takes much more time to be completed.

Table 5.1: PCF Side Pump Combiner Fabrication Parameters.

Taper length	**Waist diameter**	**Laser power**	**Pulling speed**
50 mm	30 μm	STD-20	0.02
	45 μm	STD-40	0.03
70 mm	30 μm	STD-20	0.02
	45 μm	STD-40	0.026

For the taper ratio of 2.89, I have slightly decreased the power of the CO_2 laser to STD-40 bit (9.2 W) and increased the pulling velocity to 0.03 μm/ms for 50 mm taper length as compared to 30 μm taper waist diameter. Since while desired taper waist diameter decreases, the pulling speed must be slowed down accordingly. The other parameters have been kept the same for 70 mm taper length for 45 μm taper waist diameter since this amount of power has been

enough to taper. The summary of all of the parameters has shown as in **Table 5.1**.

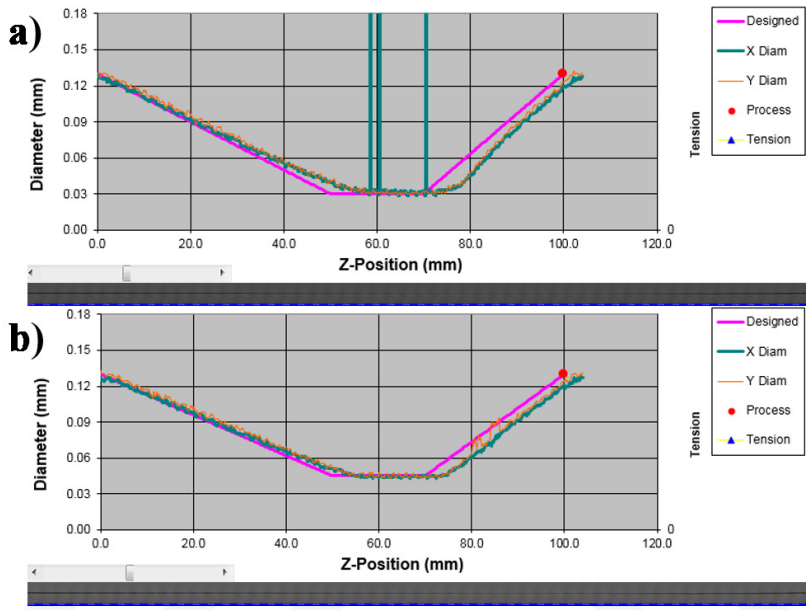

Figure 5.5: The taper results of the 130 μm pump fiber with 50 mm taper length for (a) 30 μm and (b) 45 μm taper waist diameter.

The taper results obtained regarding all the parameters listed above have been grouped based on the taper lengths 50 mm and 70 mm, respectively. Firstly, I have shared the taper results of the pump fiber with 50 mm taper length for both 30 μm and 45 μm taper waist diameters as shown in **Fig. 5.5**.

In the same manner, the taper results of the pump fiber with 70 mm taper length for both 30 μm and 45 μm taper waist diameters have been shown in **Fig. 5.6**. After completing the taper process, by clicking the measure button on the taper software, the machine scans the whole taper region, takes pictures, and forms a single photograph. The images belonging to each taper have also been shown below the taper results in these two figures.

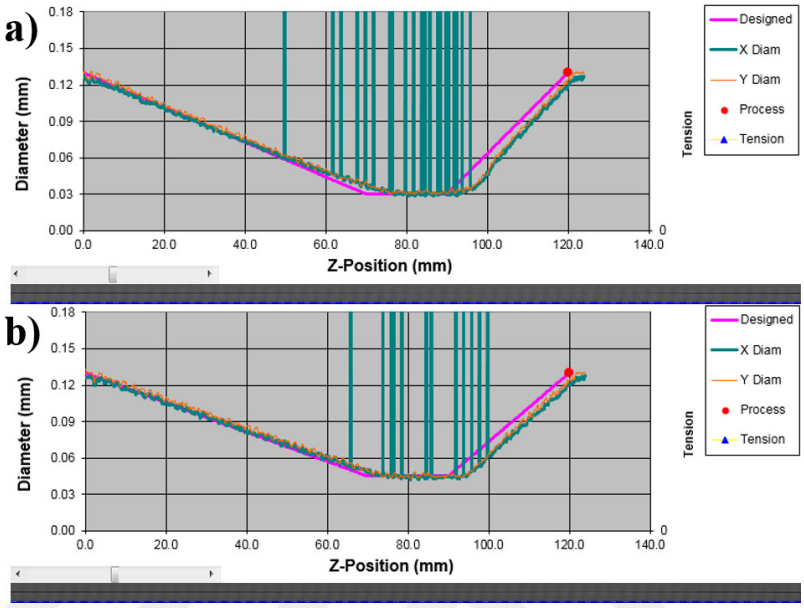

Figure 5.6: The taper results of the 130 μm pump fiber with 70 mm taper length for (a) 30 μm and (b) 45 μm taper waist diameter.

5.2.2 Photonic crystal fibers

Yb doped high power fiber laser systems have reached saturation in all regards, such as power scaling and the non-linear effects thresholds. Therefore, several other specialty fibers have been proposed to further both power scaling and the thresholds of the non-linear effects. These so-called specialty fibers are of a more general class of micro-structured optical fibers, where light is guided by structural modifications and not only by refractive index differences. These fibers can be divided into two groups based on the waveguide mechanisms. First one is hollow-core Photonic band-gap fibers (HCPBGFs) [197–200], and the other one is solid core Photonic crystal fibers (PCFs), also called holey-fibers or hole-assisted fibers [201–204]. PBGFs have hollow core structures, unlike solid-core PCFs and the working principle is also different than them. The photonic band-gap effect is responsible for the guiding light inside the core due to the micro-structured cladding region rather than a core with an increased refractive index compared to conventional step-index fibers.

On the other hand, the index guiding mechanism is responsible for solid core

PCFs like the conventional optical fibers. And, the cladding region of these fibers has been formed with the periodic structure of air holes, most likely in a hexagonal lattice form by utilizing the capillary tubes for the preform fabrication. The fiber's design may vary depending on the parameters such as d, the diameter of the air holes, and Λ, the distance between two adjacent holes (lattice constant). The criteria for the single-mode operation of a PCF is given below [205–207]:

$$\frac{d}{\Lambda} < 0.4. \tag{5.1}$$

In the light of this information, I have also studied the all-solid core PCF fabrication with various air hole and fiber cladding diameters; however, all have been designed and fabricated based on a 2-layered hexagonal lattice structure. For the preform fabrication, silica rods and capillaries have been used to form the planned construction, and then the whole stack has been fused to fabricate the PCF form. Although there are fibers in the repository having 8 μm air hole diameter, I have chosen the PCF #7 whose core/cladding diameters are 45 μm/360 μm, respectively. Additionally, the average air hole diameter for this fiber is around 12 μm, and the average lattice constant is 25 μm, then by a simple calculation

$$\frac{d}{\Lambda} = \frac{12\mu m}{25\mu m} = 0.48. \tag{5.2}$$

With these specifications, this fiber is not a single-mode one before the CO_2 laser operation compared to the other ones. However, on the other hand, I have confronted the air hole collapse problem while working with the PCF having 8 μm air hole diameters with a specific laser power required to achieve enough fuse depth. In this respect, I have benefited from a larger air hole diameter of the PCF #7 and prevented the collapse of the fiber, and arranged the power of the CO_2 laser system more freely during the side pump combiner fabrication. An optical microscope image of the cross-section of PCF #7 having 360 μm cladding diameter has been shown in **Fig. 5.7** with 20x objective in Dark Field (DF) mode for the sake of visualization.

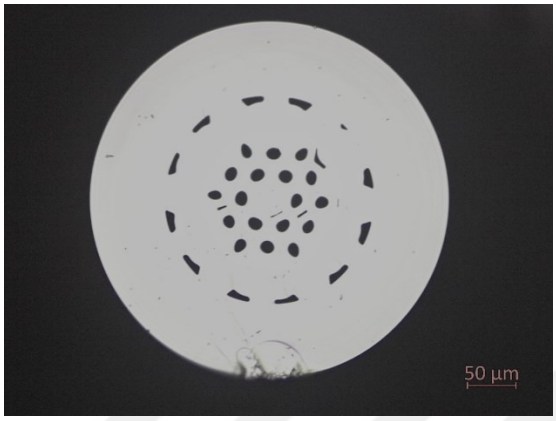

Figure 5.7: Optical microscope image of the cross-section of PCF #7 having 360 μm cladding diameter with 20x objective in Dark Field (DF) mode.

5.2.3 Characterization of the combiners

Before the side pump combiner fabrication, I have studied the CO_2 laser power optimization to analyze the power threshold that the fiber collapses. For this experiment, I have exposed only the PCF to the CO_2 laser radiation and observed that the air hole diameters of the fiber dramatically decrease beyond the laser power level of STD–100 (8 W). Afterward, tapered pump fibers and PCF #7 signal fiber have been spliced to fabricate side pump combiners.However, the laser power optimization study has been performed again to achieve the desired fused depth and prevent the collapse of the PCF simultaneously for this case since with the tapered fiber, the total size of the sample increases. PCF alone has 360 μm diameter, but adding the tapered fiber up becomes 390 μm for 30 μm and 405 μm diameters for 45 μm taper waist diameters, at the center and keep increasing up to the edges.

Therefore, the laser power has been rearranged to STD–135 bit (7.4 W) in this study for both combiners. The difference between the two power calibration values is that while the sample size increases, the interaction of the laser and the material also enhances, and thus the required energy lowers. Therefore, I have also obtained the best results with this laser power value.

As mentioned above, taper waist length has been chosen as 30 mm with a taper

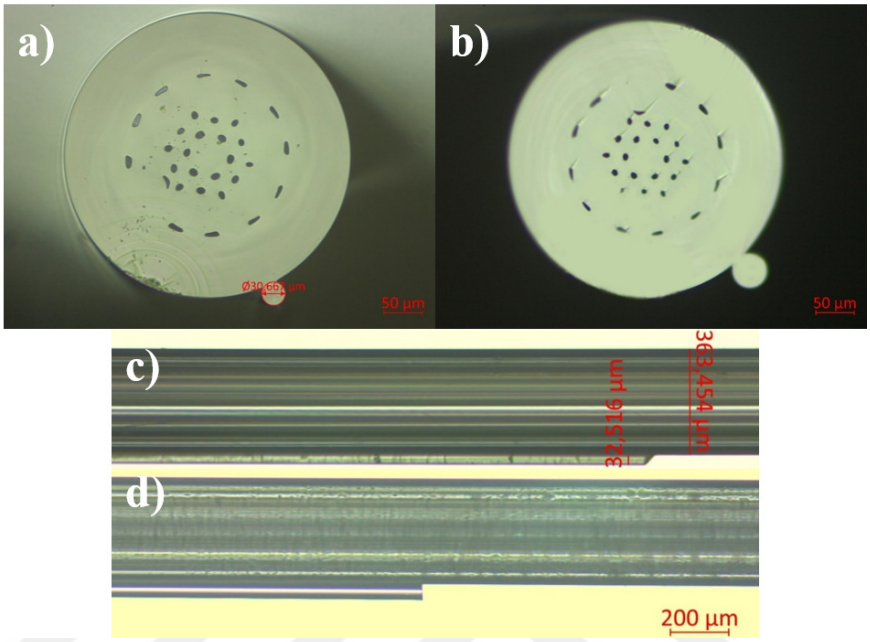

Figure 5.8: Optical microscope images of the cross-section of (1 x 1) + 1 PCF side pump combiners based on (a) 30 μm taper and (b) 45 μm taper, and (c, d) their side-view images, respectively.

length of 70 mm. Therefore, to cover the taper waist region with some regions of the tapered fiber, the splice has been performed along 60 mm long. It has taken 60 seconds with 1000 μm/ms stage velocity by the LZM-100 LAZERMaster glass processing system. The PCF and the tapered fiber have been carefully mounted to the fiber holder to attain the best contact region so that the pump coupling efficiency would be higher. Besides, two fibers have been coiled to each other in helix structure by rotating two left and right rotators of the splicing machine in counter direction for 360° angle. After many trials, I have fabricated two combiners based on these parameters. As a result, optical microscope images of the cross-section of the (1 + 1) x 1 PCF side pump combiners have been shown in **Fig. 5.8a** and **Fig. 5.8b** based on 30 μm and 45 μm tapers, respectively. In addition, side view images of the combiners have also been demonstrated in **Fig. 5.8c** and **Fig. 5.8d** to illustrate the splice quality between the tapered pump fiber and the PCF.

After the fabrication, both side pump combiner samples were subjected to the optical characterization, which was performed with a high-power diode laser with

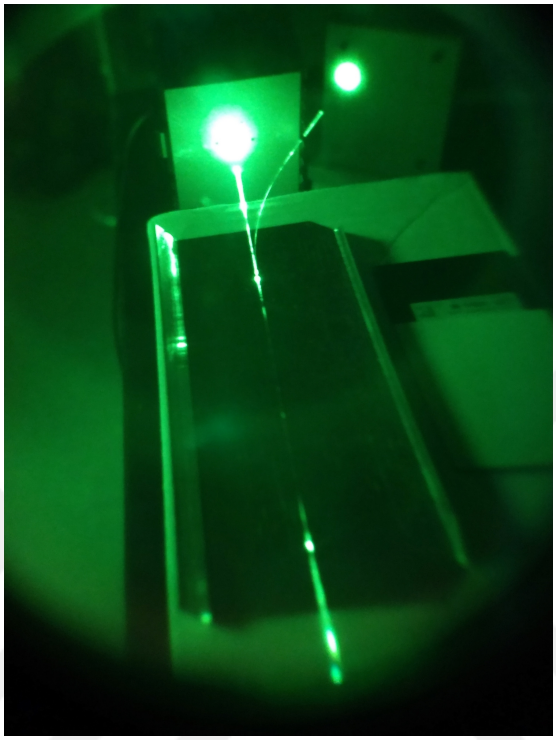

Figure 5.9: The infrared camera image of a PCF side pump combiner sample in (1 + 1) x 1 configuration during the coupling efficiency test.

976 nm central wavelength and 125 W maximum output power. The output fiber of the pump diode has been spliced to the pump port of the combiner directly. As an example, the infrared camera image of a side pump combiner sample has been taken during the pump-power coupling efficiency test for the sake of visualization. 60 mm-long splice region at the center could be observed by the infrared camera thanks to the light guiding. The image belonging to this experiment has been shown in **Fig. 5.9**.

Eventually, I have obtained 113.4 W power of total launched pump power with an efficiency of 90% for the combiner based on 45 μm tapered pump fiber, as shown in **Fig. 5.10a**. On the other hand, I have obtained 119.2 W power of total launched pump power with an efficiency of 95% for the combiner based on 30 μm tapered pump fiber, as shown in **Fig. 5.10b**. In this study, I have also observed a 5% difference between the 30 μm and 45 μm taper waist diameters. In summary, the optical efficiency increases while the taper waist diameter decreases as expected with parallel to the intuitive sense and the literature study that has

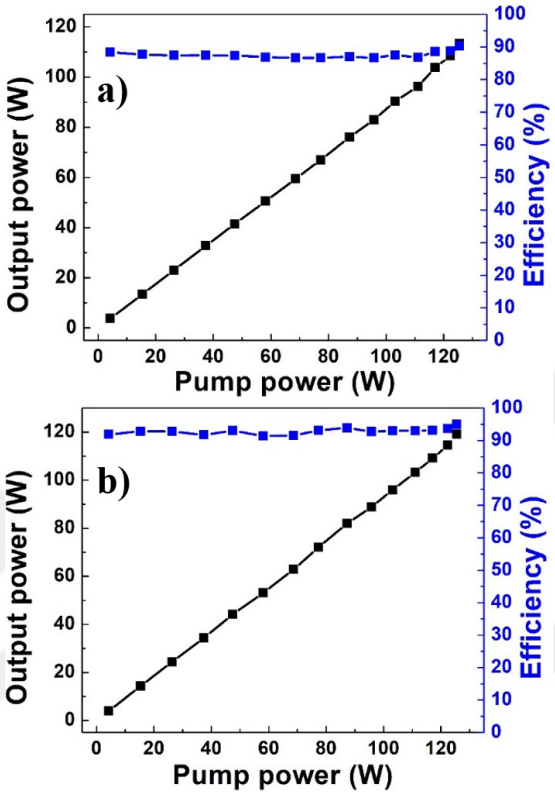

Figure 5.10: Power and efficiency characterization of the side pump combiners (a) based on 45 μm taper waist diameter and (b) based on 30 μm taper waist diameter.

been published [187, 193, 194].

5.2.4 Signal Transmission of the PCF

After the pump power and coupling efficiency test, I have also tested the signal transmission capability of PCF #7. For that purpose, I have taken a piece of signal fiber, and to fulfill the whole core region of the PCF, I have integrated 4 mm 105μm /125μm multi-mode (MM) fiber with a 0.22 numerical aperture (NA). After then, this fiber has been integrated into PCF, whose optical microscope image has been shown in **Fig. 5.11a**. Finally, having utilized a 30 mm asphericon lens, I have obtained an output beam profile as shown in **Fig. 5.11b**.

In high-power laser applications, an endcap component would be added to

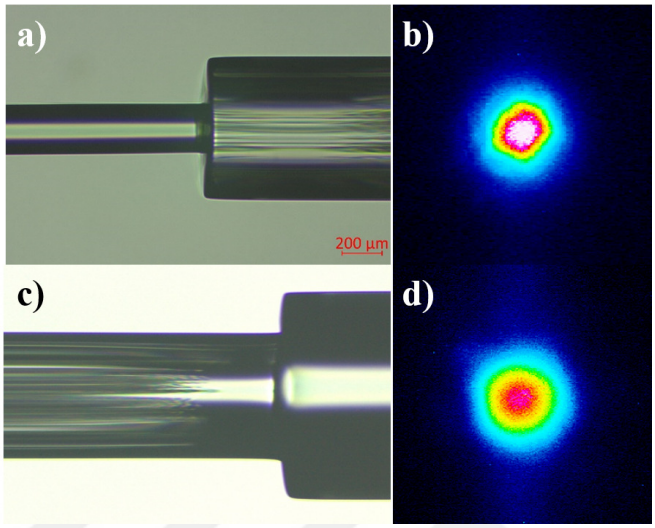

Figure 5.11: (a) Optical microscope image of the splice point between 125 μm fiber to PCF and (b) the corresponding beam-profile output and (c) the optical microscope image of the endcap and (d) the corresponding output beam profile for PCF signal transmission study.

the system to prevent damage to the output fiber. For that purpose, a 5 mm piece of triple-clad fiber (400μm/440μm/660μm) has been spliced to the end of PCF as an endcap. The optical microscope image of the splice between the PCF and the triple-clad fiber has been shown in **Fig. 5.11c**. Moreover, the output beam profile has been recorded to prove the preservation of signal transmission over the endcap, as shown in **Fig. 5.11d**. In conclusion, PCF based side pump combiner study has been completed using PCF #7 and 130 μm pump fiber with two different taper waist diameters.

5.3 On a Ultra-low NA Active Fiber

I have continued the side pump combiner study with a different fiber elaborated in the 3rd chapter of this thesis. The so-called fiber is ultra-low NA active fiber with octagonal shape whose optical microscope image of the cross-section shown in **Fig. 3.7** with low and high index polymer coatings onside, respectively. Just as a reminder, the cladding diameter of the fiber is 410 μm. Therefore, since this

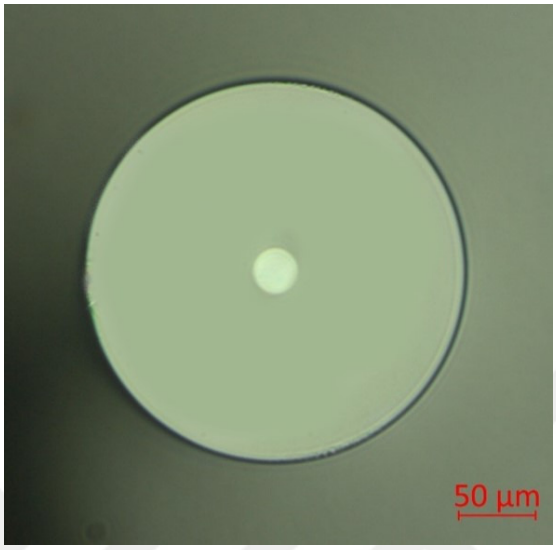

Figure 5.12: Optical microscope image of the pump fiber's cross-section having 250 μm cladding diameter to taper.

fiber has larger cladding diameter than PCF and is a step-index all-solid LMA fiber, power optimization study will be easier than the previous one. Differently, I have chosen a pump fiber having a 250 μm cladding diameter, considering high power laser applications for the future in this study. As a beginning, the ultra-low NA acive fiber based side pump combiner will also be fabricate in a (1 + 1) x 1 configuration. The optical microscope image of the pump fiber has been demonstrated in **Fig. 5.12**.

5.3.1 Taper results of the pump fiber

In this study, 250 μm cladding pump fiber has been tapered to two different waist diameters for comparison. First of all, I have tapered this pump fiber to a 40 μm taper waist diameter, as shown in **Fig. 5.13a**. In addition, taper length has been modified to 65 mm in this experiment. And then I have decided to increase the length of the taper waist. Thus, I have increased it to 35 mm for this taper to make the splicing process more effortless and enhance the pump coupling efficiency.

Table 5.2: Ultra-low NA Side Pump Combiner Fabrication Parameters.

Taper length	**Waist diameter**	**Waist length**	**Pulling speed**	**Laser power**	**Waist-add power**
65 mm	40 μm	35 mm	0.025	STD–150 bit	20 bit
60 mm	50 μm	40 mm	0.04	STD–150 bit	20 bit

After determining the taper parameters, I have also optimized the power of the CO_2 laser to STD–150 bit (7.2 W) and the pulling velocity as 0.025 μm/ms for 40 mm taper length. As mentioned earlier, while the fiber enlarges, the interaction between the laser and the material increases, and thus the required energy lowers. The reason why lower power is enough for 250 μm cladding pump fiber than 130 μm cladding pump fiber is this so-called fact. Waist add-power has also been arranged as 20 bit to sustain the waist diameter to achieve the desired diameter for this taper.

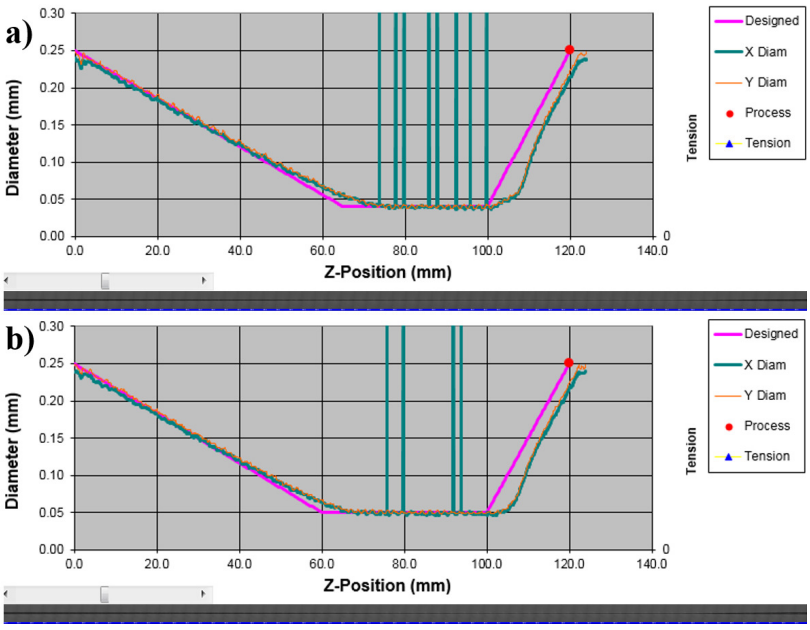

Figure 5.13: The taper result of the 250 μm pump fiber (a) with 65 mm taper length for 40 μm taper waist diameter and (b) 60 mm taper length for 50 μm taper waist diameter.

Secondly, I have tapered this pump fiber to a 50 μm taper waist diameter, as shown in **Fig. 5.13b**. Taper length has been altered to 60 mm, and waist-length has been increased to 40 mm for this taper. I have used the same power level but changed the pulling velocity to 0.04 μm/ms for 50 mm taper length. Waist add-power has also been arranged as 20 bit to sustain the waist diameter to achieve the desired diameter. All parameters have been summarized as in **Table 5.2**.

5.3.2 Optical characterization of the sample

After the tapering process, I have studied the splicing of the ultra-low NA active fiber and the tapered pump fiber utilizing the LZM-100 glass processing system. First of all, the laser power optimization study has been performed to achieve desired fused depth for this side pump combiner fabrication. Since this fiber has an octagonal shape and does not have air holes like PCF, I could utilize more power than the previous case. Thus, the laser power has been set to STD–75 bit (8.5 W) in this study for both combiner samples. The splice has been performed along 70 mm-long, and it has taken a time of 70 s with 1000 μm/ms stage velocity by the so-called glass processing system. However, the octagonal shape of the fiber prevented us from twisting fibers from each other.

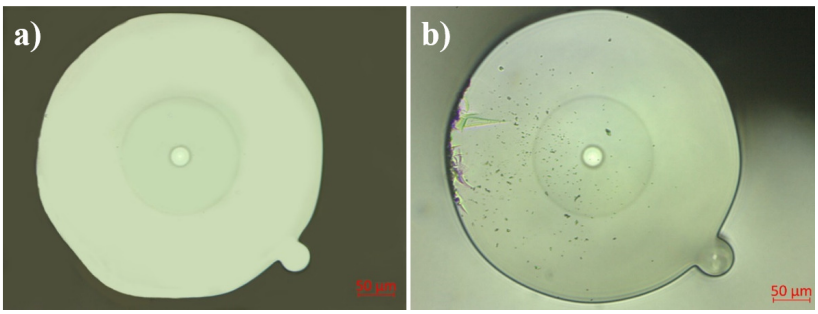

Figure 5.14: Optical microscope images of the cross-section of (1 x 1) + 1 ultra-low NA side pump combiners based on (a) 40 μm taper and (b) 50 μm taper.

On the contrary, the interaction between the ultra-low NA active fiber and the pared fiber decreases, and thus the splice quality and efficiency are affected severely. Therefore, I decided to perform the splicing in a horizontal configuration

to tapered fiber lying on the top edge of the active fiber. I have increased the splicing length and time since I have also increased the taper waist length to avoid losing the pump coupling efficiency. After all these arrangements, I have fabricated two combiners based on 40 μm and 50 μm tapered pump fibers. As a result, the optical microscope images of the cross-section of both combiners have been shown in **Fig. 5.14a** and **Fig. 5.14b**.

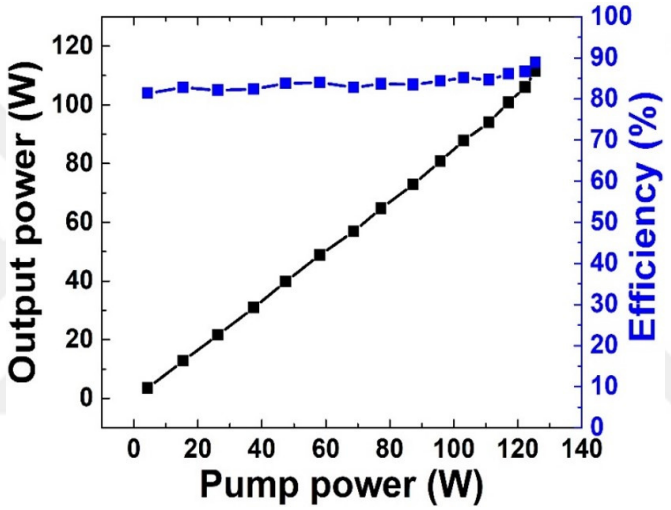

Figure 5.15: Power and efficiency characterization of side pump combiner on the low-NA active fiber with 40 μm taper waist diameter of 250 μm pump fiber.

I have fabricated two combiners based on two different tapered fibers as mentioned above; however, I have just characterized the one based on 40 μm tapered fiber due to the failure during the test for the other one. Thus, the optical characterization of this successful combiner has been performed with the same setup explained in the previous section. In return, I have obtained 111.6 W power of total launched pump power with an efficiency of 89% for the combiner based on 40 μm tapered pump fiber, as shown in **Fig. 5.15**.

Chapter 6

Conclusions

In the first part of this study, I have built high-power fiber laser oscillators and amplifier systems utilizing commercial Yb-doped active fibers. Having gained engineering experience, I have contributed to the mechanical design of the laser cavity itself, the cooling plates for optical components, and the active fiber that needs to be cooled down during high power operation. Besides, I have extensively studied the handling of an optical fiber, such as cleaving and splicing processes, having vital importance for high power laser operation. Additionally, I have also studied carefully the thermal management of the whole system. As a result of this extensive study, I could have built high power fiber laser systems with up to a 2 kW maximum power level based on commercial Yb-doped active fibers.

Besides, I have fabricated Yb-doped active fibers having 20 μm and 400 μm core and cladding diameters, respectively. After certain optimization studies, I have fabricated low-loss high-quality Yb-doped Aluminophosphosilicate (APS) fibers similar to the commercial counterpart, Nufern branded optical fibers. In the same manner, I have also established high power fiber laser systems to characterize the homemade self-fabricated Yb-doped fibers in the Master Oscillator Power Amplifier (MOPA) configuration. During these studies, I have confronted the so-called non-linear effects mentioned in the 1st chapter of this thesis, namely, the SRS, the SBS, finally, and most importantly, the TMI effect. Decreasing the

fiber length and increasing the bandwidth of the FBG component in the cavity might resolve and mitigate the SRS and the SBS effect. However, on the other hand, mitigating the TMI effect requires more effort and a new approach.

For that purpose, I have aimed to fabricate a new generation of Yb-doped active fiber having a numerical aperture (NA) lower than the value of 0.06, also called ultra-low NA active fiber. I have achieved this by precisely controlling the amount of the Yb element in the matrix with the help of the Modified Chemical Vapor Deposition (MCVD) system. Since the Yb element increasingly contributes to the fiber's NA, I have decreased the Yb ion concentration to obtain an active fiber having an NA of 0.034, as explained in the 3rd chapter of this thesis. After the fabrication, I have performed optical characterization of the fiber up to 1 kW power level in a MOPA configuration in a bending diameter around 90 cm with a diffraction-limited output beam. Our system was pump limited; therefore, I could not observe the TMI threshold of the fiber. In brief, this study proves that ultra-low NA fibers might be a powerful tool to mitigate the TMI effect by inhibiting the higher-order modes (HOMs) intrinsically.

In the second part of this thesis, I have aimed to establish an organic relation between the color center formation inside the fiber and the TMI effect. For that purpose, first of all, I have configured a laser cavity to trigger the TMI effect by bending the active fiber loosely, in a greater diameter than the one required to eliminate the HOMs. This time we favor the presence of the HOMs to sustain the TMI effect in the cavity. Then, I have utilized two different probe lasers (red and green) and measured the change in their intensities in the presence of the TMI effect. Afterward, I have repeated the experiment by revising the laser cavity by bending the active fiber tight in a 10 cm diameter to eliminate this time the HOMs. We expected to observe different attitudes in the change of the probe lasers' intensity; however, the expectation was not fulfilled. As a result, I have obtained the same behavioral pattern from the probe lasers' intensity in the presence and the lack of the TMI effect. Therefore, I have concluded no organic relation exists between the color centers inside the fiber and the TMI effect.

Finally, I have studied side pump combiner technique, another method to mitigate the TMI effect by decreasing and homogenizing the thermal load on the active fiber. For that purpose, I have studied side pump combiner fabrication based on (1 + 1) x 1 configuration, comprising one signal fiber and one pump fiber. Aiming to achieve novelty, I have implemented this technique to a homemade Photonic Crystal Fiber (PCF) and the ultra-low NA active fiber mentioned previously. For that purpose, I have utilized a CO_2 laser system to taper the pump fiber up to desired taper waist diameters. After that, the tapered pump fiber and the signal fiber have been spliced by the same system. As a result of this preliminary study, I have attained 95% and 89% pump coupling efficiencies from the PCF and ultra-low NA active fiber-based side pump combiners, respectively. These results have been obtained by carefully adjusting the power of the CO_2 laser and the exposure time.

In conclusion, this thesis mentions the development of fiber laser systems having high-power, high-beam quality, and related problems. Pointing the most critical and recent issue out, I have proposed some solutions to mitigate this phenomenon, the TMI effect. Additionally, I have conducted experiments to relate the TMI effect and intrinsic properties of the active fiber.

Bibliography

[1] T. H. Maiman, "Stimulated Optical Radiation in Ruby," *Nature*, vol. 187, no. 4736, pp. 493–494, 1960.

[2] W. Duley, "Gas lasers," in *Encyclopedia of Physical Science and Technology*, pp. 399–408, New York: Academic Press, third edition ed., 2003.

[3] H. Gedda, J. Powell, and A. Kaplan, "A process efficiency comparison of nd:yag and co2 laser cladding," *Welding in the World, Le Soudage Dans Le Monde*, vol. 46, pp. 75–86, 07 2002.

[4] G. Huber, C. Kränkel, and K. Petermann, "Solid-state lasers: status and future [invited]," *J. Opt. Soc. Am. B*, vol. 27, pp. B93–B105, Nov 2010.

[5] G. Boulon, "Fifty years of advances in solid-state laser materials," *Optical Materials*, vol. 34, no. 3, pp. 499–512, 2012.

[6] J. Yan and N. Takayama, "Fundamentals of laser processing," in *Micro and Nanoscale Laser Processing of Hard Brittle Materials*, Micro and Nano Technologies, pp. 17–35, Elsevier, 2020.

[7] B. Lepadatescu and G. C. Cristinel, "Some applications of CO_2 laser in industrial engineering," *J. Chem. Chem. Eng.*, vol. 02, 2017.

[8] K. Y. Benyounis, S. A. Elsheikhi, F. M. Shuaeib, and H. Achour, "CO_2 laser welding challenges, modeling and optimization," in *Reference Module in Materials Science and Materials Engineering*, Elsevier, 2019.

[9] P. Loosen, "Advances in CO_2 laser technology for industrial applications," in *9th International Symposium on Gas Flow and Chemical Lasers*,

vol. 1810, pp. 26 – 33, International Society for Optics and Photonics, SPIE, 1993.

[10] C. J. Koester and E. Snitzer, "Amplification in a fiber laser," *Appl. Opt.*, vol. 3, pp. 1182–1186, Oct 1964.

[11] J. Stone and C. A. Burrus, "Neodymium-doped fiber lasers: Room temperature CW operation with an injection laser pump," *Appl. Opt.*, vol. 13, pp. 1256–1258, Jun 1974.

[12] R. Mears, L. Reekie, S. Poole, and D. Payne, "Neodymium-doped silica single-mode fibre lasers," *Electron. Lett.*, vol. 21, pp. 738–740, August 1985.

[13] R. J. Mears, L. Reekie, I. M. Jauncey, and D. N. Payne, "Low-noise erbium-doped fibre amplifier operating at 1.54 μm," *Electron. Lett.*, vol. 23, pp. 1026–1028, 1987.

[14] Y. Jeong, J. Nilsson, J. Sahu, P. Dupriez, C. Codemard, D. Soh, C. Farrell, J. Kim, D. Richardson, and D. Payne, "High power fiber lasers," in *Pacific Rim Conference on Lasers Electro-Optics*, pp. 1056–1057, 2005.

[15] M. N. Zervas and C. A. Codemard, "High power fiber lasers: A review," *IEEE J. Sel. Top. Quantum Electron.*, vol. 20, no. 5, pp. 219–241, 2014.

[16] C. Jauregui, J. Limpert, and A. Tünnermann, "High-power fibre lasers," *Nat. Photon.*, vol. 7, no. 11, pp. 861–867, 2013.

[17] D. J. Richardson, J. Nilsson, and W. A. Clarkson, "High power fiber lasers: current status and future perspectives [invited]," *J. Opt. Soc. Am. B*, vol. 27, pp. B63–B92, Nov 2010.

[18] C. Gao, Z. Huang, Y. Wang, H. Zhan, L. Ni, K. Peng, Y. Li, Z. Jia, X. Wang, A. You, X. Xiang, J. Wang, F. Jing, H. Lin, and A. Lin, "Yb-doped Aluminophosphosilicate laser fiber," *J. Lightw. Technol.*, vol. 34, pp. 5170–5174, Nov 2016.

[19] D. Lipatov, A. N. Guryanov, M. V. Yashkov, M. M. Bubnov, and M. E. Likhachev, "Fabrication of Yb_2O_3-Al_2O_3-P_2O_5-SiO_2 optical fibers with a

perfect step-index profile by the MCVD process," *Inorg. Mater.*, vol. 54, pp. 276–282, 2018.

[20] S. Kuhn, F. Möller, C. Hupel, S. Hein, F. Beier, J. Nold, N. Haarlammert, T. Schreiber, R. Eberhardt, and A. Tünnermann, "Active materials for high-power fiber lasers prepared by all-solution doping technique," in *Optical Components and Materials XV*, vol. 10528, pp. 29 – 40, International Society for Optics and Photonics, SPIE, 2018.

[21] S. Kuhn, S. Hein, C. Hupel, J. Nold, N. Haarlammert, T. Schreiber, R. Eberhardt, and A. Tünnermann, "All-solution doping technique for high power fiber lasers - refractive index influence in the vicinity of Al:P=1:1," in *Laser Congress 2017 (ASSL, LAC)*, p. ATu5A.6, Optical Society of America, 2017.

[22] S. Kuhn, S. Hein, C. Hupel, J. Ihring, J. Nold, N. Haarlammert, T. Schreiber, R. Eberhardt, and A. Tünnermann, "All-solution doping technique for tailoring core composition toward Yb:$AlPO_4$:SiO_2," in *Advanced Solid State Lasers*, p. AM4A.5, Optical Society of America, 2015.

[23] S. She, B. Liu, C. Chang, Y. Xu, X. Xiao, X. Cui, Z. Li, J. Zheng, S. Gao, Y. Zhang, Y. Li, Z. Zhou, L. Mei, C. Hou, and H. Guo, "Yb/Ce codoped aluminosilicate fiber with high laser stability for multi-kW level laser," *J. Lightw. Technol.*, vol. 38, no. 24, pp. 6924–6931, 2020.

[24] L. Liao, Y. Wang, Y. Xing, H. Li, J. Peng, N. Dai, and J. Li, "Fabrication, measurement, and application of 20/400 Yb-doped fiber," *Appl. Opt.*, vol. 54, pp. 6516–6520, Jul 2015.

[25] A. N. Abramov, M. M. Bubnov, A. N. Guryanov, D. S. Lipatov, M. E. Likhachev, M. A. Melkumov, and M. V. Yashkov, "Fabrication of Active Fluoroaluminosilicate Fibers for High-Power Fiber Lasers," *Inorg. Mater.*, vol. 54, no. 3, pp. 271–275, 2018.

[26] E. Sekiya, P. Barua, K. Saito, and A. Ikushima, "Fabrication of Yb-doped silica glass through the modification of MCVD process," *J. Non-Cryst. Solids*, vol. 354, no. 42, pp. 4737–4742, 2008.

[27] K. J. Lim, S. K. W. Seah, J. Y. Ye, W. W. Lim, C. P. Seah, Y. B. Tan, S. Tan, H. Lim, R. Sidharthan, A. R. Prasadh, C. J. Chang, S. Yoo, and S. L. Chua, "High absorption large-mode area step-index fiber for tandem-pumped high-brightness high-power lasers," *Photon. Res.*, vol. 8, pp. 1599–1604, Oct 2020.

[28] V. Dominic, S. MacCormack, R. Waarts, S. Sanders, S. Bicknese, R. Dohle, E. Wolak, P. Yeh, and E. Zucker, "110 w fibre laser," *Electron. Lett.*, vol. 35, pp. 1158–1160, July 1999.

[29] K. Ueda, H. Sekiguchi, and H. Kan, "kW fiber lasers for industrial applications," in *The 5th Pacific Rim Conference on Lasers and Electro-Optics*, vol. 2, p. 443, 2003.

[30] V. Gapontsev, D. Gapontsev, N. Platonov, O. Shkurikhin, V. Fomin, A. Mashkin, M. Abramov, and S. Ferin, "2 kW CW ytterbium fiber laser with record diffraction-limited brightness," in *CLEO/Europe Conference on Lasers and Electro-Optics Europe*, pp. 508–, 2005.

[31] K. C. Kao and G. A. Hockham, "Dielectric-fibre surface waveguides for optical frequencies," in *Proc. IEE*, vol. 113, pp. 1151–1158, July 1966.

[32] L. G. Cohen and J. Stone, "Interferometric measurements of minimum dispersion spectra in short lengths of single-mode fiber," in *Optical Fiber Communication*, p. PD2, Optical Society of America, 1982.

[33] R. Tricker, "Optical fibres in power systems," in *Electrical Engineer's Reference Book (Sixteenth Edition)* (M. Laughton and D. Warne, eds.), pp. 37–1–37–17, Oxford: Newnes, sixteenth edition ed., 2003.

[34] E. M. A. Elkaramany, M. F. O. Hameed, and S. S. A. Obayya, *Introduction to Optical Waveguides*, pp. 3–27. Springer International Publishing, 2019.

[35] Y. Koike and K. Koike, "Optical fibers," in *Polymer Science: A Comprehensive Reference*, pp. 283–304, Amsterdam: Elsevier, 2012.

[36] A. Kumar, R. Varshney, and K. Thyagarajan, "Birefringence calculations in elliptical-core optical fibres," *Electron. Lett.*, vol. 20, pp. 112–113, February 1984.

[37] R. Davies, D. Davidson, and M. Singh, "Single-mode optical fiber with arbitrary refractive index profile: Propagation solution by the numerov method," *J. Lightw. Technol.*, vol. 3, no. 3, pp. 619–627, 1985.

[38] M. O. Vassell, "Calculation of propagating modes in a graded-index optical fibre," *Optoelectron.*, vol. 6, no. 4, pp. 271–286, 1974.

[39] J. H. Povlsen, P. Danielsen, and G. Jacobsen, "Modal propagation constants, group delays, and eigenfields for practical multimode graded-index fibers," *J. Opt. Soc. Am.*, vol. 72, pp. 1506–1513, Nov 1982.

[40] G. Jacobsen, "Evanescent-wave analysis of general clad graded-index fibers," *J. Opt. Soc. Am.*, vol. 72, pp. 699–709, Jun 1982.

[41] D. Gloge, "Weakly guiding fibers," *Appl. Opt.*, vol. 10, pp. 2252–2258, Oct 1971.

[42] A. W. Snyder, "Weakly guiding optical fibers," *J. Opt. Soc. Am.*, vol. 70, pp. 405–411, Apr 1980.

[43] J. D. Love, C. D. Hussey, A. W. Snyder, and R. A. Sammut, "Polarization corrections to mode propagation on weakly guiding fibers," *J. Opt. Soc. Am.*, vol. 72, pp. 1583–1591, Dec 1982.

[44] A. Kwan, J. Dudley, and E. Lantz, "Who really discovered snell's law?," *Physics World*, vol. 15, pp. 64–64, apr 2002.

[45] N. Bloembergen and P. S. Pershan, "Light Waves at the Boundary of Nonlinear Media," *Phys. Rev.*, vol. 128, no. 2, pp. 606–622, 1962.

[46] M. Rodrigues and P. S. Carvalho, "Laws of reflection and Snell's law revisited by video modeling," in *12th Education and Training in Optics and Photonics Conference*, vol. 9289, pp. 513 – 516, International Society for Optics and Photonics, SPIE, 2014.

[47] J. Metz, "The geometry of snell's law," *The Physics Teacher*, vol. 52, no. 3, pp. 177–177, 2014.

[48] S.-R. Kothapalli, H. Liu, J. C. Liao, Z. Cheng, and S. S. Gambhir, "Endoscopic imaging of cerenkov luminescence," *Biomed. Opt. Express*, vol. 3, pp. 1215–1225, Jun 2012.

[49] N. A. Issa and W. E. Padden, "Light acceptance properties of multimode microstructured optical fibers: Impact of multiple layers," *Opt. Express*, vol. 12, pp. 3224–3235, Jul 2004.

[50] Y. Kato, K. Kitayama, S. Seikai, and N. Uchida, "Effective cutoff wavelength of the LP_{11} mode in single-mode fiber cables," *IEEE J. Quant. Electron.*, vol. 17, no. 1, pp. 35–39, 1981.

[51] D. Bayuwati, T. B. Waluyo, and I. Mulyanto, "Determination of the effective cut-off wavelength of several single-mode fiber patchcords," *J. Phys. Conf. Ser.*, vol. 985, p. 012002, mar 2018.

[52] Y. Kitayama and S. Tanaka, "Effective cutoff wavelength of single-mode fiber," in *Optical Fiber Communication*, p. TuN14, Optical Society of America, 1984.

[53] M. N. Zervas, "High power ytterbium-doped fiber lasers — fundamentals and applications," *Int. J. Mod. Phys. B*, vol. 28, no. 12, p. 1442009, 2014.

[54] G. P. Agrawal, "Chapter 5 - fiber lasers," in *Applications of Nonlinear Fiber Optics (Third Edition)* (G. P. Agrawal, ed.), pp. 193–254, Academic Press, third edition ed., 2021.

[55] K. Shima, S. Ikoma, K. Uchiyama, Y. Takubo, M. Kashiwagi, and D. Tanaka, "5-kW single stage all-fiber Yb-doped single-mode fiber laser for materials processing," in *Fiber Lasers XV: Technology and Systems*, vol. 10512, pp. 45 – 50, International Society for Optics and Photonics, SPIE, 2018.

[56] P. Muniz-Cánovas, Y. O. Barmenkov, A. V. Kir'yanov, J. L. Cruz, and M. V. Andrés, "Ytterbium-doped fiber laser as pulsed source of narrowband amplified spontaneous emission," *Sci. Rep.*, vol. 9, no. 1, p. 13073, 2019.

[57] D. Zhu, Y. Zhao, Y. Tu, R. Li, K. Liu, Y. Zhao, B. Yu, and L. Lu, "Relaxation characteristics for efficient fluorescence lifetime detection of gain media in the fiber laser," *Appl. Opt.*, vol. 60, pp. 5678–5681, Jul 2021.

[58] M. Montecchi, A. Mecozzi, M. Settembre, M. Tamburrini, and L. DiGaspare, "Gain and noise in rare-earth-doped optical fibers," *J. Opt. Soc. Am. B*, vol. 8, pp. 134–141, Jan 1991.

[59] E. S. Magden, P. Callahan, N. Li, J. D. B. Bradley, N. Singh, A. Ruocco, L. A. Kolodziejski, E. P. Ippen, and M. R. Watts, "Frequency domain spectroscopy in rare-earth-doped gain media," *IEEE J. Sel. Top. Quantum Electron.*, vol. 24, no. 5, pp. 1–10, 2018.

[60] A. Dutta, "Ytterbium-doped fibers for high-power fiber lasers," *AIP Conference Proceedings*, vol. 2352, no. 1, p. 020071, 2021.

[61] J. Kawanaka, S. Tokita, H. Nishioka, M. Fujita, K. Yamakawa, K. ichi Ueda, and Y. Izawa, "Dramatically improved laser characteristics of diode-pumped Yb-doped materials at low temperature," *Laser Phys.*, vol. 15, pp. 1306–1312, 2005.

[62] G. Town and N. Akhmediev, "Lasers — optical fiber lasers," in *Encyclopedia of Modern Optics* (R. D. Guenther, ed.), pp. 475–485, Oxford: Elsevier, 2005.

[63] C. X. Yu, O. Shatrovoy, T. Y. Fan, and T. F. Taunay, "Diode-pumped narrow linewidth multi-kilowatt metalized Yb fiber amplifier," *Opt. Lett.*, vol. 41, pp. 5202–5205, Nov 2016.

[64] D. Marcuse, "Classical derivation of the laser rate equation," *IEEE J. Quantum Electron.*, vol. 19, no. 8, pp. 1228–1231, 1983.

[65] G. L. Lippi, J. Mørk, and G. P. Puccioni, "Numerical solutions to the Laser Rate Equations with noise: technical issues, implementation and pitfalls

," in *Nanophotonics VII* (D. L. Andrews, A. J. Bain, J.-M. Nunzi, and A. Ostendorf, eds.), vol. 10672, pp. 82 – 95, International Society for Optics and Photonics, SPIE, 2018.

[66] F. C. Maciuc, C. I. Stere, and A.-R. P. Sterian, "Rate equations for an erbium laser system: a numerical approach," in *ROMOPTO 2000: Sixth Conference on Optics* (V. I. Vlad, ed.), vol. 4430, pp. 136 – 146, International Society for Optics and Photonics, SPIE, 2001.

[67] H. Yokoyama and S. D. Brorson, "Rate equation analysis of microcavity lasers," *J. Appl. Phys.*, vol. 66, no. 10, pp. 4801–4805, 1989.

[68] S. P. Singh, R. Gangwar, and N. Singh, "Nonlinear scattering effects in optical fibers," *Prog. Electromagn. Res.*, vol. 74, pp. 379–405, 2007.

[69] R. Kale, P. M. Ingale, and R. T. Murade, "Comparison of SRS & SBS (non linear scattering) in optical fiber," *Int. J. Recent Technol.*, vol. 2, pp. 118–122, 2013.

[70] M. Niklès, L. Thévenaz, and P. A. Robert, "Brillouin gain spectrum characterization in single-mode optical fibers," *J. Lightw. Technol.*, vol. 15, pp. 1842–1851, 1997.

[71] D. Cotter, "Observation of stimulated Brillouin scattering in low-loss silica fibre at 1.3 μm," *Electron. Lett.*, vol. 18, pp. 495–496, 1982.

[72] Y. Ohmori, Y. Sasaki, and T. Edahiro, "Fibre-length dependence of critical power for stimulated Raman scattering," *Electron. Lett.*, vol. 17, pp. 593–594, 1981.

[73] G. L. Lan, P. K. Banerjee, and S. S. Mitra, "Raman scattering in optical fibers," *J. Raman Spectrosc.*, vol. 11, pp. 416–423, 1981.

[74] R. G. Smith, "Optical power handling capacity of low loss optical fibers as determined by stimulated Raman and Brillouin scattering," *Appl. Opt.*, vol. 11, pp. 2489–2494, 1972.

[75] Y. R. Shen and N. Bloembergen, "Theory of stimulated Brillouin and Raman scattering," *Phys. Rev.*, vol. 137, pp. 1787–1805, 1965.

[76] A. Roohforouz, R. Eyni Chenar, R. Rezaei-Nasirabad, S. Azizi, K. Hejaz, A. Hamedani Golshan, A. Abedinajafi, V. Vatani, and S. H. Nabavi, "The effect of population inversion saturation on the transverse mode instability threshold in high power fiber laser oscillators," *Sci. Rep.*, vol. 11, no. 1, p. 21116, 2021.

[77] S. E. Kholaif, Y. Tu, C. Stihler, C. Jauregui, and J. Limpert, "Characterization of transverse mode instability in fiber-laser systems using a position-sensitive detector," in *Fiber Lasers XVIII: Technology and Systems* (M. N. Zervas, ed.), vol. 11665, pp. 193 – 198, International Society for Optics and Photonics, SPIE, 2021.

[78] C. Jauregui, C. Stihler, S. Kholaif, Y. Tu, and J. Limpert, "Mitigation of transverse mode instability in polarization maintaining, high-power fiber amplifiers," in *Fiber Lasers XVIII: Technology and Systems* (M. N. Zervas, ed.), vol. 11665, pp. 147 – 152, International Society for Optics and Photonics, SPIE, 2021.

[79] C. V. S. Raman, "A new radiation," *Indian J. Phys.*, vol. 2, pp. 387–396, 1928.

[80] D. J. Dougherty, F. X. Kärtner, H. A. Haus, and E. P. Ippen, "Measurement of the raman gain spectrum of optical fibers," *Opt. Lett.*, vol. 20, pp. 31–33, Jan 1995.

[81] R. Shuker and R. W. Gammon, "Raman-scattering selection-rule breaking and the density of states in amorphous materials," *Phys. Rev. Lett.*, vol. 25, pp. 222–225, Jul 1970.

[82] R. Y. Chiao, C. H. Townes, and B. P. Stoicheff, "Stimulated brillouin scattering and coherent generation of intense hypersonic waves," *Phys. Rev. Lett.*, vol. 12, pp. 592–595, May 1964.

[83] R. Tkach, A. Chraplyvy, and R. Derosier, "Spontaneous brillouin scattering for single-mode optical-fibre characterisation," *Electron. Lett.*, vol. 22, pp. 1011–1013(2), September 1986.

[84] C. Jauregui, C. Stihler, and J. Limpert, "Transverse mode instability," *Adv. Opt. Photon.*, vol. 12, pp. 429–484, Jun 2020.

[85] A. V. Smith and J. J. Smith, "Mode instability in high power fiber amplifiers," *Opt. Express*, vol. 19, pp. 10180–10192, May 2011.

[86] T. Eidam, C. Wirth, C. Jauregui, F. Stutzki, F. Jansen, H. J. Otto, O. Schmidt, T. Schreiber, J. Limpert, and A. Tünnermann, "Experimental observations of the threshold-like onset of mode instabilities in high power fiber amplifiers," *Opt. Express*, vol. 19, pp. 13218–13224, Jun 2011.

[87] M. Kuznetsov, O. Vershinin, V. Tyrtyshnyy, and O. Antipov, "Low-threshold mode instability in Yb^{3+}-doped few-mode fiber amplifiers," *Opt. Express*, vol. 22, pp. 29714–29725, Dec 2014.

[88] D. Alekseev, V. Tyrtyshnyy, M. Kuznetsov, and O. Antipov, "Transverse-mode instability in high-gain few-mode Yb^{3+}-doped fiber amplifiers with a 10-μm core diameter with or without backward reflection," *IEEE J. Sel. Top. Quantum Electron.*, vol. 24, pp. 1–8, May 2018.

[89] C. Jauregui, T. Eidam, J. Limpert, and A. Tünnermann, "Impact of modal interference on the beam quality of high-power fiber amplifiers," *Opt. Express*, vol. 19, pp. 3258–3271, Feb 2011.

[90] L. Dong, "Stimulated thermal rayleigh scattering in optical fibers," *Opt. Express*, vol. 21, pp. 2642–2656, Feb 2013.

[91] K. R. Hansen, T. T. Alkeskjold, J. Broeng, and J. Lægsgaard, "Theoretical analysis of mode instability in high-power fiber amplifiers," *Opt. Express*, vol. 21, pp. 1944–1971, Jan 2013.

[92] M. M. Johansen, K. R. Hansen, T. T. Alkeskjold, and J. Lægsgaard, "Fiber amplifiers under thermal loads leading to transverse mode instability," in *Fiber Lasers XI: Technology, Systems, and Applications*, vol. 8961, pp. 494 – 502, International Society for Optics and Photonics, SPIE, 2014.

[93] B. G. Ward, "Modeling of transient modal instability in fiber amplifiers," *Opt. Express*, vol. 21, pp. 12053–12067, May 2013.

[94] K. R. Hansen, T. T. Alkeskjold, J. Broeng, and J. Lægsgaard, "Thermally induced mode coupling in rare-earth doped fiber amplifiers," *Opt. Lett.*, vol. 37, pp. 2382–2384, Jun 2012.

[95] K. R. Hansen, T. T. Alkeskjold, J. Broeng, and J. Lægsgaard, "Thermo-optical effects in high-power Ytterbium-doped fiber amplifiers," *Opt. Express*, vol. 19, pp. 23965–23980, Nov 2011.

[96] F. Jansen, F. Stutzki, H.-J. Otto, T. Eidam, A. Liem, C. Jauregui, J. Limpert, and A. Tünnermann, "Thermally induced waveguide changes in active fibers," *Opt. Express*, vol. 20, pp. 3997–4008, Feb 2012.

[97] L. Dong, "Thermal lensing in optical fibers," *Opt. Express*, vol. 24, pp. 19841–19852, Aug 2016.

[98] W. Liu, J. Cao, and J. Chen, "Study on thermal-lens induced mode coupling in step-index large mode area fiber lasers," *Opt. Express*, vol. 27, pp. 9164–9177, Mar 2019.

[99] J. Boullet, C. Vincont, A. Jolly, and C. Pierre, "Regime dependence of photo-darkening-induced modal degradation in high power fiber amplifier (Conference Presentation)," in *Fiber Lasers XIV: Technology and Systems*, vol. 10083, pp. 128 – 128, International Society for Optics and Photonics, SPIE, 2017.

[100] H. J. Otto, N. Modsching, C. Jauregui, J. Limpert, and A. Tünnermann, "Impact of photodarkening on the mode instability threshold," *Opt. Express*, vol. 23, pp. 15265–15277, Jun 2015.

[101] R. Cao, Y. Wang, G. Chen, N. Zhao, Y. Xing, Y. Liu, X. Lin, Y. Cheng, H. Li, L. Yang, and J. Li, "Investigation of photo-darkening-induced thermal load in Yb-doped fiber lasers," *IEEE Photon. Technol. Lett.*, vol. 31, pp. 809–812, June 2019.

[102] O. Antipov, M. Kuznetsov, D. Alekseev, and V. Tyrtyshnyy, "Influence of a backward reflection on low-threshold mode instability in Yb^{3+}-doped few-mode fiber amplifiers," *Opt. Express*, vol. 24, pp. 14871–14879, Jun 2016.

[103] D. Hanna, R. Percival, I. R. Perry, R. G. Smart, P. Suni, J. Townsend, and A. Tropper, "Continuous-wave oscillation of a monomode ytterbium-doped fibre laser," *Electron. Lett.*, vol. 24, pp. 1111–1113, 1988.

[104] D. Hanna, R. Percival, I. Perry, R. Smart, P. Suni, and A. Tropper, "An Ytterbium-doped monomode fibre laser: Broadly tunable operation from 1.010 μm to 1.162 μm and three-level operation at 974 nm," *J. Mod. Opt.*, vol. 37, no. 4, pp. 517–525, 1990.

[105] H. Pask, R. Carman, D. Hanna, A. Tropper, C. Mackechnie, P. Barber, and J. Dawes, "Ytterbium-doped silica fiber lasers: Versatile sources for the 1–1.2 μm region," *IEEE J. Sel. Top. Quantum Electron.*, vol. 1, no. 1, pp. 2–13, 1995.

[106] J. Allain, M. Monerie, H. Poignant, and T. Georges, "High-efficiency ytterbium-doped fluoride fibre laser," *J. Non-Cryst. Solids*, vol. 161, pp. 270–273, 1993.

[107] C. MacKechnie, W. Barnes, D. Hanna, and J. Townsen, "High power ytterbium (Yb^{3+})-doped fibre laser operating in the 1.12 μm region," *Electron. Lett.*, vol. 29, pp. 52–53, January 1993.

[108] S. Magne, M. Druetta, J. Goure, J. Thevenin, P. Ferdinand, and G. Monnom, "An ytterbium-doped monomode fiber laser: amplified spontaneous emission, modeling of the gain and tunability in an external cavity," *J. Lumin.*, vol. 60-61, pp. 647–650, 1994.

[109] R. Paschotta, J. Nilsson, A. Tropper, and D. Hanna, "Ytterbium-doped fiber amplifiers," *IEEE J. Quantum Electron.*, vol. 33, no. 7, pp. 1049–1056, 1997.

[110] R. Paschotta, D. Hanna, P. De Natale, G. Modugno, M. Inguscio, and P. Laporta, "Power amplifier for 1083 nm using ytterbium doped fibre," *Opt. Commun.*, vol. 136, no. 3, pp. 243–246, 1997.

[111] J. P. Koplow, D. A. V. Kliner, and L. Goldberg, "Single-mode operation of a coiled multimode fiber amplifier," *Opt. Lett.*, vol. 25, pp. 442–444, Apr 2000.

[112] N. S. Platonov, D. V. Gapontsev, V. P. Gapontsev, and V. Shumilin, "135 W CW fiber laser with perfect single mode output," in *Conference on Lasers and Electro-Optics*, p. CPDC3, Optical Society of America, 2002.

[113] J. Limpert, A. Liem, H. Zellmer, and A. Tünnermann, "500 W continuous-wave fibre laser with excellent beam quality," *Electron. Lett.*, vol. 39, pp. 645–647, 2003.

[114] E. Stiles, "New developments in IPG fiber laser technology," in *Proceedings of the 5th International Workshop on Fiber Lasers*, 2009.

[115] Y. Midilli, O. B. Efunbajo, B. şimşek, and B. Ortaç, "1018 nm yb-doped high-power fiber laser pumped by broadband pump sources around 915 nm with output power above 100 w," *Appl. Opt.*, vol. 56, pp. 7225–7229, Sep 2017.

[116] W. Wang, J. Leng, J. Cao, S. Guo, X. Xu, and Z. Jiang, "Method for stripping cladding light in the high power fiber laser," *Opt. Commun.*, vol. 287, pp. 187–191, 2013.

[117] M. Berisset, L. Lebrun, M. Faucon, R. Kling, J. Boullet, and C. Aguergaray, "Laser surface texturization for high power cladding light stripper," in *Components and Packaging for Laser Systems II*, vol. 9730, pp. 220 – 226, International Society for Optics and Photonics, SPIE, 2016.

[118] S. Zou, H. Chen, J. Zhang, H. Yu, Z. Zhang, J. Sun, and X. Lin, "Cladding light stripper of high average stripped power density with high attenuation of 39 dB and low temperature rise," *IEEE Photon. J.*, vol. 10, no. 1, pp. 1–10, 2018.

[119] S. Zou, H. Yu, J. Zhang, J. Zuo, Z. Dong, S. Xu, L. Chang, P. Zhao, and X. Lin, "Highly efficient fiber cladding light stripper fabricated by chemical mask etching method," *J. Lightw. Technol.*, vol. 38, no. 18, pp. 5136–5141, 2020.

[120] M. Wysmolek, C. Ottenhues, T. Pulzer, T. Theeg, H. Sayinc, M. Steinke, U. Morgner, J. Neumann, and D. Kracht, "Microstructured fiber cladding light stripper for kilowatt-class laser systems," *Appl. Opt.*, vol. 57, pp. 6640–6644, Aug 2018.

[121] E. Y. Yildirim, A. Karatutlu, E. T. Balk, Y. Midilli, and B. Ortaç, "Combined method for the fabrication of high-power cladding light stripper using a buffered oxide etchant," *Appl. Opt.*, vol. 58, pp. 6926–6933, Sep 2019.

[122] A. Kliner, K.-C. Hou, M. Plötner, C. Hupel, T. Stelzner, T. Schreiber, R. Eberhardt, and A. Tünnermann, "Fabrication and evaluation of a 500 W cladding-light stripper," in *MOEMS and Miniaturized Systems XII*, vol. 8616, pp. 178 – 185, International Society for Optics and Photonics, SPIE, 2013.

[123] J. Anderegg, S. J. Brosnan, and P. Thielen, "System and method to remove light from cladding," Mar 2006.

[124] L. Bansal, V. R. Supradeepa, T. Kremp, S. Sullivan, and C. H. III, "High power cladding mode stripper," in *Fiber Lasers XII: Technology, Systems, and Applications*, vol. 9344, pp. 65 – 70, International Society for Optics and Photonics, SPIE, 2015.

[125] A. Wetter, M. Faucher, and B. Sévigny, "High power cladding light strippers," in *Fiber Lasers V: Technology, Systems, and Applications*, vol. 6873, pp. 473 – 480, International Society for Optics and Photonics, SPIE, 2008.

[126] W. Guo, Z. Chen, H. Zhou, J. Li, and J. Hou, "Cascaded cladding light extracting strippers for high power fiber lasers and amplifiers," *IEEE Photon. J.*, vol. 6, no. 3, pp. 1–6, 2014.

[127] Y. Jeong, A. J. Boyland, J. K. Sahu, S. Chung, J. Nilsson, and D. N. Payne, "Multi-kilowatt single-mode ytterbium-doped large-core fiber laser," *J. Opt. Soc. Korea*, vol. 13, no. 4, pp. 416–422, 2009.

[128] K. Tankala, B. Samson, A. Carter, J. Farroni, D. Machewirth, N. Jacobson, U. Manyam, A. Sanchez, M.-Y. Chen, A. Galvanauskas, W. Torruellas, and

Y. Chen, "New developments in high power eye-safe LMA fibers," in *Fiber Lasers III: Technology, Systems, and Applications*, vol. 6102, pp. 27–35, International Society for Optics and Photonics, SPIE, 2006.

[129] D. Walton, S. Gray, J. Wang, M.-J. Li, X. Chen, A. Liu, L. Zenteno, and A. Crowley, "Kilowatt-level, narrow-linewidth capable fibers and lasers," in *Fiber Lasers IV: Technology, Systems, and Applications*, vol. 6453, pp. 251–260, International Society for Optics and Photonics, SPIE, 2007.

[130] C. Jauregui, J. Limpert, and A. Tünnermann, "On the raman threshold of passive large mode area fibers," in *Fiber Lasers VIII: Technology, Systems, and Applications*, vol. 7914, pp. 70–75, International Society for Optics and Photonics, SPIE, 2011.

[131] D. Jablonowski, "Fiber manufacture at AT&T with the MCVD process," *J. Lightw. Technol.*, vol. 4, no. 8, pp. 1016–1019, 1986.

[132] W. M. Flegal, E. A. Haney, R. S. Elliott, J. T. Kamino, and D. N. Ernst, "Report: Making single-mode preforms by the MCVD process," *AT&T Tech. J.*, vol. 65, pp. 56–61, January 1986.

[133] C. Hupel, S. Kuhn, S. Hein, N. Haarlammert, J. Nold, F. Beier, B. Sattler, T. Schreiber, R. Eberhardt, and A. Tünnermann, "MCVD based fabrication of low-NA fibers for high power fiber laser application," in *Advanced Solid State Lasers*, p. AM4A.2, Optical Society of America, 2015.

[134] A. V. Smith and J. J. Smith, "Modeled fiber amplifier performance near the mode instability threshold," 2013.

[135] B. Ward, C. Robin, and I. Dajani, "Origin of thermal modal instabilities in large mode area fiber amplifiers," *Opt. Express*, vol. 20, pp. 11407–11422, May 2012.

[136] C. Jauregui, T. Eidam, H. J. Otto, F. Stutzki, F. Jansen, J. Limpert, and A. Tünnermann, "Physical origin of mode instabilities in high-power fiber laser systems," *Opt. Express*, vol. 20, pp. 12912–12925, Jun 2012.

[137] R. Tao, X. Wang, and P. Zhou, "Comprehensive theoretical study of mode instability in high-power fiber lasers by employing a universal model and its implications," *IEEE J. Sel. Top. Quantum*, vol. 24, no. 3, pp. 1–19, 2018.

[138] Y. Jeong, J. K. Sahu, D. N. Payne, and J. Nilsson, "Ytterbium-doped large-core fiber laser with 1.36 kW continuous-wave output power," *Opt. Express*, vol. 12, pp. 6088–6092, Dec 2004.

[139] D. Jain, Y. Jung, P. Barua, S. Alam, and J. K. Sahu, "Demonstration of ultra-low NA rare-earth doped step index fiber for applications in high power fiber lasers," *Opt. Express*, vol. 23, pp. 7407–7415, Mar 2015.

[140] F. Kong, C. Dunn, J. Parsons, M. T. Kalichevsky-Dong, T. W. Hawkins, M. Jones, and L. Dong, "Large-mode-area fibers operating near single-mode regime," *Opt. Express*, vol. 24, pp. 10295–10301, May 2016.

[141] V. Khitrov, J. D. Minelly, R. Tumminelli, V. Petit, and E. S. Pooler, "3 kW single-mode direct diode-pumped fiber laser," in *Fiber Lasers XI: Technology, Systems, and Applications*, vol. 8961, pp. 137–142, International Society for Optics and Photonics, SPIE, 2014.

[142] F. Beier, C. Hupel, J. Nold, S. Kuhn, S. Hein, J. Ihring, B. Sattler, N. Haarlammert, T. Schreiber, R. Eberhardt, and A. Tünnermann, "Narrow linewidth, single mode 3 kW average power from a directly diode pumped ytterbium-doped low NA fiber amplifier," *Opt. Express*, vol. 24, pp. 6011–6020, Mar 2016.

[143] F. Beier, C. Hupel, S. Kuhn, S. Hein, J. Nold, F. Proske, B. Sattler, A. Liem, C. Jauregui, J. Limpert, N. Haarlammert, T. Schreiber, R. Eberhardt, and A. Tünnermann, "Single mode 4.3 kW output power from a diode-pumped Yb-doped fiber amplifier," *Opt. Express*, vol. 25, pp. 14892–14899, Jun 2017.

[144] K. Peng, H. Zhan, L. Ni, X. Wang, Y. Wang, C. Gao, Y. Li, J. Wang, F. Jing, and A. Lin, "Single-mode large-mode-area laser fiber with ultralow numerical aperture and high beam quality," *Appl. Opt.*, vol. 55, pp. 10133–10137, Dec 2016.

[145] S. Liu, K. Peng, H. Zhan, L. Ni, X. Wang, Y. Wang, Y. Li, J. Yu, L. Jiang, R. Zhu, J. Wang, F. Jing, and A. Lin, "3 kW 20/400 Yb-doped aluminophosphosilicate fiber with high stability," *IEEE Photon. J.*, vol. 10, no. 5, pp. 1–8, 2018.

[146] T. Deschamps, N. Ollier, H. Vezin, and C. Gonnet, "Clusters dissolution of Yb^{3+} in codoped SiO_2-Al_2O_3-P_2O_5 glass fiber and its relevance to photodarkening," *J. Chem. Phys.*, vol. 136, no. 1, p. 014503, 2012.

[147] S. Jetschke, S. Unger, A. Schwuchow, M. Leich, and J. Kirchhof, "Efficient Yb laser fibers with low photodarkening by optimization of the core composition," *Opt. Express*, vol. 16, pp. 15540–15545, Sep 2008.

[148] D. H. Rank, C. W. Cho, N. D. Foltz, and T. A. Wiggins, "Stimulated thermal Rayleigh scattering," *Phys. Rev. Lett.*, vol. 19, pp. 828–830, Oct 1967.

[149] T. J. Karr, M. C. Rushford, J. R. Murray, and J. R. Morris, "Measurement of the stimulated thermal Rayleigh scattering instability," *J. Opt. Soc. Am. B*, vol. 8, pp. 993–999, May 1991.

[150] H. B. Lü, S. Z. Xu, H. J. Wang, X. D. Yuan, C. Zhao, and Y. Q. Fu, "Evolution of Oxygen Deficiency Center on Fused Silica Surface Irradiated by Ultraviolet Laser and Posttreatment," *Adv. Condens. Matter Phys.*, vol. 2014, p. 769059, 2014.

[151] N. Richard, L. Martin-Samos, S. Girard, A. Ruini, A. Boukenter, Y. Ouerdane, and J.-P. Meunier, "Oxygen deficient centers in silica: optical properties within many-body perturbation theory," *J. Phys.: Condens. Matter*, vol. 25, p. 335502, jul 2013.

[152] L. Skuja, "Optically active oxygen-deficiency-related centers in amorphous silicon dioxide," *J. Non-Cryst. Solids*, vol. 239, no. 1, pp. 16–48, 1998.

[153] M. Cannas, S. Agnello, R. Boscaino, F. M. Gelardi, M. Leone, and B. Boizot, "Optical properties of oxygen-deficiency related centers in amorphous SiO_2 investigated by synchrotron radiation," *Radiat. Eff. Defect S.*, vol. 157, no. 6-12, pp. 1045–1049, 2002.

[154] L. Skuja, "Optically active oxygen-deficiency-related centers in amorphous silicon dioxide," *J. Non-cryst. Solids*, vol. 239, pp. 16–48, 1998.

[155] P. S. Russell, D. P. Hand, Y. T. Chow, and L. J. Poyntz-Wright, "Optically induced creation, transformation, and organization of defects and color centers in optical fibers," in *International Workshop on Photoinduced Self-Organization Effects in Optical Fiber*, vol. 1516, pp. 47 – 54, International Society for Optics and Photonics, SPIE, 1991.

[156] C. L. Janer, A. Carballar, L. Navarro, J. L. Galo, and R. M. Rubio, "Photosensitivity color-center model for Ge-doped Silica preforms," *IEEE Photon. J.*, vol. 5, no. 4, pp. 6100511–6100511, 2013.

[157] T. Arai, K. Ichii, K. Okada, T. Kitabayashi, S. Tanigawa, and M. Fujimaki, "Photodarkening phenomenon in Yb-doped fibers," *Fujikura Technical Review*, 2009.

[158] J. Koponen, M. Söderlund, H. J. Hoffman, D. A. V. Kliner, J. P. Koplow, and M. Hotoleanu, "Photodarkening rate in Yb-doped silica fibers," *Appl. Opt.*, vol. 47, pp. 1247–1256, Mar 2008.

[159] K. E. Mattsson, "Photo darkening of rare earth doped silica," *Opt. Express*, vol. 19, pp. 19797–19812, Oct 2011.

[160] S. Yoo, C. Basu, A. J. Boyland, C. Sones, J. Nilsson, J. K. Sahu, and D. Payne, "Photodarkening in Yb-doped aluminosilicate fibers induced by 488 nm irradiation," *Opt. Lett.*, vol. 32, pp. 1626–1628, Jun 2007.

[161] S. Wang, F. Lou, C. Yu, Q. Zhou, M. Wang, S. Feng, D. Chen, L. Hu, W. Chen, M. Guzik, and G. Boulon, "Influence of Al^{3+} and P^{5+} ion contents on the valence state of Yb^{3+} ions and the dispersion effect of Al^{3+} and P^{5+} ions on Yb^{3+} ions in silica glass," *J. Mater. Chem. C*, vol. 2, pp. 4406–4414, 2014.

[162] C. G. Carlson, K. E. Keister, P. D. Dragic, A. Croteau, and J. G. Eden, "Photoexcitation of Yb-doped aluminosilicate fibers at 250 nm: evidence for excitation transfer from oxygen deficiency centers to Yb^{3+}," *J. Opt. Soc. Am. B*, vol. 27, pp. 2087–2094, Oct 2010.

[163] C. Wang, G. Zhou, H. Liu, Y. Han, W. Wang, and L. Hou, "Properties of non-bridging oxygen hole centers defects in Yb^{3+}/Al^{3+} co-doped photonic crystal fiber by using powder melting technology," *J. Lightw. Technol.*, vol. 31, pp. 2864–2868, Sep 2013.

[164] P. D. Dragic, M. Cavillon, and J. Ballato, "Materials for optical fiber lasers: A review," *Appl. Phys. Rev.*, vol. 5, no. 4, p. 041301, 2018.

[165] I. Manek-Hönninger, J. Boullet, T. Cardinal, F. Guillen, S. Ermeneux, M. Podgorski, R. B. Doua, and F. Salin, "Photodarkening and photobleaching of an Ytterbium-doped silica double-clad LMA fiber," *Opt. Express*, vol. 15, pp. 1606–1611, Feb 2007.

[166] S. Jetschke, A. Schwuchow, and S. Unger, "Transient absorption in pumped Yb fibers opens a path to photodarkening," *Laser Phys. Lett.*, vol. 11, p. 085101, jun 2014.

[167] J. J. Koponen, M. J. Söderlund, H. J. Hoffman, and S. K. T. Tammela, "Measuring photodarkening from single-mode Ytterbium doped silica fibers," *Opt. Express*, vol. 14, pp. 11539–11544, Nov 2006.

[168] M. Li, R. Cao, N. Zhao, Y. Liu, G. Chen, J. Leng, J. Chen, and J. Li, "Investigation of the photodarkening of Yb-Li co-doped silica fiber," *Opt. Mater. Express*, vol. 8, pp. 3007–3013, Oct 2018.

[169] H. Gebavi, D. Milanese, S. Taccheo, D. Mechin, A. Monteville, F. S. Freyria, B. Bonelli, and T. Robin, "Photodarkening of infrared irradiated Yb^{3+}-doped alumino-silicate glasses: Effect on UV absorption bands and fluorescence spectra," *Fibers*, vol. 1, no. 3, pp. 101–109, 2013.

[170] P. D. Dragic, C. G. Carlson, and A. Croteau, "Characterization of defect luminescence in Yb doped silica fibers: part I NBOHC," *Opt. Express*, vol. 16, pp. 4688–4697, Mar 2008.

[171] J. Jasapara, M. Andrejco, D. DiGiovanni, and R. Windeler, "Effect of heat and H_2 gas on the photo-darkening of Yb^{3+} fibers," in *Conference on Lasers and Electro-Optics/Quantum Electronics and Laser Science Conference and*

Photonic Applications Systems Technologies, p. CTuQ5, Optical Society of America, 2006.

[172] M. Engholm, L. Norin, and D. Åberg, "Strong UV absorption and visible luminescence in ytterbium-doped aluminosilicate glass under UV excitation," *Opt. Lett.*, vol. 32, pp. 3352–3354, Nov 2007.

[173] M. Engholm and L. Norin, "Preventing photodarkening in Ytterbium-doped high power fiber lasers; correlation to the UV-transparency of the core glass," *Opt. Express*, vol. 16, pp. 1260–1268, Jan 2008.

[174] M. Engholm, P. Jelger, F. Laurell, and L. Norin, "Improved photodarkening resistivity in Ytterbium-doped fiber lasers by Cerium codoping," *Opt. Lett.*, vol. 34, pp. 1285–1287, Apr 2009.

[175] S. Jetschke, S. Unger, A. Schwuchow, M. Leich, and J. Kirchhof, "Efficient Yb laser fibers with low photodarkening by optimization of the core composition," *Opt. Express*, vol. 16, pp. 15540–15545, Sep 2008.

[176] T. Deschamps, N. Ollier, H. Vezin, and C. Gonnet, "Clusters dissolution of Yb^{3+} in codoped SiO_2-Al_2O_3-P_2O_5 glass fiber and its relevance to photodarkening," *J. Chem. Phys.*, vol. 136, no. 1, p. 014503, 2012.

[177] B. Schaudel, P. Goldner, M. Prassas, and F. Auzel, "Cooperative luminescence as a probe of clustering in Yb^{3+} doped glasses," *J. Alloys Compd.*, vol. 300-301, pp. 443–449, 2000.

[178] D. J. DiGiovanni and A. J. Stentz, "Tapered fiber bundles for coupling light into and out of cladding-pumped fiber devices," Jul 1999.

[179] Q. Xiao, H. Ren, X. Chen, P. Yan, and M. Gong, "Tapered fiber bundle 7×1 end-pumping coupler capable of high power CW operation," *IEEE Photon. Technol. Lett.*, vol. 25, no. 24, pp. 2442–2445, 2013.

[180] C. H. III, M. Fishteyn, A. D. Yablon, M. J. Andrejco, K. Brar, J. Mann, M. D. Mermelstein, and D. J. DiGiovanni, "Tapered fiber bundles for combining laser pumps," in *Fiber Lasers II: Technology, Systems, and Applications*, vol. 5709, pp. 263 – 272, SPIE, 2005.

[181] A. Kosterin, V. Temyanko, M. Fallahi, and M. Mansuripur, "Tapered fiber bundles for combining high-power diode lasers," *Appl. Opt.*, vol. 43, pp. 3893–3900, Jul 2004.

[182] H. Zhou, Z. Chen, X. Zhou, J. Hou, and J. Chen, "All-fiber 7 × 1 pump combiner for high power fiber laser," *Opt. Commun.*, vol. 347, pp. 137–140, 2015.

[183] Q. Xiao, P. Yan, J. He, Y. Wang, X. Zhang, and M. Gong, "Tapered fused fiber bundle coupler capable of 1 kW laser combining and 300 W laser splitting," *Laser Phys.*, vol. 21, no. 8, pp. 1415–1419, 2011.

[184] Q. Xiao, Y. Huang, J. Sun, X. Wang, D. Li, M. Gong, and P. Yan, "Research on multi-kilowatts level tapered fiber bundle N×1 pumping combiner for high power fiber laser," *Front. Optoelectron.*, vol. 9, no. 2, pp. 301–305, 2016.

[185] C. Jauregui, S. Böhme, G. Wenetiadis, J. Limpert, and A. Tünnermann, "Side-pump combiner for all-fiber monolithic fiber lasers and amplifiers," *J. Opt. Soc. Am. B*, vol. 27, pp. 1011–1015, May 2010.

[186] Y. Sintov, Y. Glick, T. Koplowitch, O. Katz, Y. Nafcha, Y. Shamir, and R. Lavi, "A novel side coupling technique for rugged all-fiber lasers and amplifiers," in *Laser Source Technology for Defense and Security III*, vol. 6552, pp. 163 – 171, SPIE, 2007.

[187] T. Theeg, H. Sayinc, J. Neumann, L. Overmeyer, and D. Kracht, "Pump and signal combiner for bi-directional pumping of all-fiber lasers and amplifiers," *Opt. Express*, vol. 20, pp. 28125–28141, Dec 2012.

[188] Q. Tan, T. Ge, X. Zhang, and Z. Wang, "Cascaded combiners for a high power CW fiber laser," *Laser Phys.*, vol. 26, p. 025102, dec 2015.

[189] J. Koplow, L. Goldberg, and D. Kliner, "Compact 1-W Yb-doped double-cladding fiber amplifier using V-groove side-pumping," *IEEE Photon. Technol. Lett.*, vol. 10, no. 6, pp. 793–795, 1998.

[190] J. Koplow, S. Moore, and D. Kliner, "A new method for side pumping of double-clad fiber sources," *IEEE J. Quantum Electron.*, vol. 39, no. 4, pp. 529–540, 2003.

[191] Q. Xiao, P. Yan, Y. Wang, J. Hao, X. Zhang, and M. Gong, "Fused angle-polished multi-points side-pumping coupler for monolithic fiber lasers and amplifiers," *Opt. Commun.*, vol. 285, no. 8, pp. 2137–2143, 2012.

[192] Q. Xiao, P. Yan, S. Yin, J. Hao, and M. Gong, "100 W ytterbium-doped monolithic fiber laser with fused angle-polished side-pumping configuration," *Laser Phys. Lett.*, vol. 8, pp. 125–129, dec 2010.

[193] Q. Xiao, P. Yan, H. Ren, X. Chen, and M. Gong, "A side-pump coupler with refractive index valley configuration for fiber lasers and amplifiers," *J. Lightw. Technol.*, vol. 31, pp. 2715–2722, Aug 2013.

[194] C. Lei, Z. Chen, J. Leng, Y. Gu, and J. Hou, "The influence of fused depth on the side-pumping combiner for all-fiber lasers and amplifiers," *J. Lightw. Technol.*, vol. 35, pp. 1922–1928, May 2017.

[195] A. D. McLachlan and F. P. Meyer, "Temperature dependence of the extinction coefficient of fused silica for CO_2 laser wavelengths," *Appl. Opt.*, vol. 26, pp. 1728–1731, May 1987.

[196] N. Tomozeiu, "Silicon Oxide (SiO_x, $0<x<2$): a Challenging Material for Optoelectronics," in *Optoelectronics - Materials and Techniques*, ch. 3, Rijeka: IntechOpen, 2011.

[197] R. F. Cregan, B. J. Mangan, J. C. Knight, T. A. Birks, P. S. J. Russell, P. J. Roberts, and D. C. Allan, "Single-mode photonic band gap guidance of light in air," *Science*, vol. 285, no. 5433, pp. 1537–1539, 1999.

[198] J. C. Knight, J. Broeng, T. A. Birks, and P. S. J. Russell, "Photonic band gap guidance in optical fibers," *Science*, vol. 282, no. 5393, pp. 1476–1478, 1998.

[199] F. Poletti, M. N. Petrovich, and D. J. Richardson, "Hollow-core photonic bandgap fibers: technology and applications," *Nanophotonics*, vol. 2, no. 5-6, pp. 315–340, 2013.

[200] C. M. Smith, N. Venkataraman, M. T. Gallagher, D. Müller, J. A. West, N. F. Borrelli, D. C. Allan, and K. W. Koch, "Low-loss hollow-core silica/air photonic bandgap fibre," *Nature*, vol. 424, no. 6949, pp. 657–659, 2003.

[201] J. C. Knight, T. A. Birks, P. S. J. Russell, and D. M. Atkin, "All-silica single-mode optical fiber with photonic crystal cladding," *Opt. Lett.*, vol. 21, pp. 1547–1549, Oct 1996.

[202] J. C. Knight, T. A. Birks, P. S. J. Russell, and D. M. Atkin, "All-silica single-mode optical fiber with photonic crystal cladding: errata," *Opt. Lett.*, vol. 22, pp. 484–485, Apr 1997.

[203] T. A. Birks, J. C. Knight, and P. S. J. Russell, "Endlessly single-mode photonic crystal fiber," *Opt. Lett.*, vol. 22, pp. 961–963, Jul 1997.

[204] J. C. Knight, "Photonic crystal fibres," *Nature*, vol. 424, no. 6950, pp. 847–851, 2003.

[205] P. Russell, "Photonic Crystal Fibers," *Science*, vol. 299, no. 5605, pp. 358–362, 2003.

[206] P. S. Russell, "Photonic-Crystal Fibers," *J. Lightw. Technol.*, vol. 24, pp. 4729–4749, Dec 2006.

[207] K. Kiang, K. Frampton, T. Monro, R. Moore, J. Tucknott, D. Hewak, D. Richardson, and H. Rutt, "Extruded singlemode non-silica glass holey optical fibres," *Electron. Lett.*, vol. 38, pp. 546–547, June 2002.

Appendix A

RP Fiber Power script made based on the form settings

include "Units.inc"

lambda:=660 nm

include "Yb-Nufern LMA-YDF-20-400-M.inc"

; Basic fiber parameters:

L_f:= 16 fiber length

No_z_steps:=100 {no steps along the fiber}

; Refractive index profile:

r_core:=10 um {core radius}

n_cl:=1.44 {cladding index}

dr:=2e-6 {radial resolution of index table}

defarray n_f[0,r_core,dr]

readlist r, n_f[1e-6*r]:

0, 1.442

2, 1.444

4, 1.444

6, 1.443

8, 1.441

10, 1.44

n_f(r):=if r¡=r_core then n_f [r] else n_cl

calc

begin

n_max:=n_cl;

for r:=0 to r_core step dr

do n_max:=maxr(n_max,n_f(r));

end

; Parameters of the channels:

l_p1:=976 nm

w_p1:=w_p

I_p1(r):=(r<=w_p1)

```
l_s1:=1080 nm

w_s1:=w_s

I_s1(r):=exp(-2*(r/w_s1)^2)

P_pump1_fw_in:=1300

P_pump1_bw_in:=0

P_signal1_fw_in:=0

P_signal1_bw_in:=0

; Function for defining the model:

def_model():=

begin

global allow all;

set_fiber(L_f, No_z_steps, 'Yb');

set_n_profile("n_f", r_core); {for the mode solver}

add_ring(r_core, N_Yb);

max_N:=N_Yb;

max_r:=r_core;

P_in_max:=0;

P_in_max:=maxr(P_in_max, P_pump1_fw_in);

pump1_fw:=addinputchannel(P_pump1_fw_in, l_p1, 'I_p1', loss_p, forward);
```

```
P_in_max:=maxr(P_in_max, P_pump1_bw_in);

pump1_bw:=addinputchannel(P_pump1_bw_in, l_p1, 'I_p1', loss_p, backward);

P_in_max:=maxr(P_in_max, P_signal1_fw_in);

signal1_fw:=addinputchannel(P_signal1_fw_in, l_s1, 'I_s1', loss_s, forward);

P_in_max:=maxr(P_in_max, P_signal1_bw_in);

signal1_bw:=addinputchannel(P_signal1_bw_in, l_s1, 'I_s1', loss_s, backward);

set_R(signal1_fw, 0.99, 0.1);

finish_fiber();

end;

calc def_model()

show "Output powers:"

P_pump1_fw_out:=P_out(pump1_fw)

show "pump1_fw: ", P_pump1_fw_out:d3:"W"

write ["P_pump1_fw_out=", P_pump1_fw_out:d3:"W"], >>(FName$)

P_pump1_bw_out:=P_out(pump1_bw)

show "pump1_bw: ", P_pump1_bw_out:d3:"W"

write ["P_pump1_bw_out=", P_pump1_bw_out:d3:"W"], >>(FName$)

P_signal1_fw_out:=P_out(signal1_fw)

show "signal1_fw: ", P_signal1_fw_out:d3:"W"
```

```
write ["P_signal1_fw_out=", P_signal1_fw_out:d3:"W"], >>(FName$)
P_signal1_bw_out:=P_out(signal1_bw)
show "signal1_bw:", P_signal1_bw_out:d3:"W"
write ["P_signal1_bw_out=", P_signal1_bw_out:d3:"W"], >>(FName$)
G_signal1:=sp_gain(signal1_fw)
show "G_signal1:", G_signal1:d3:np:"dB"
write ["G_signal1=", G_signal1:d3:np:"dB"], >>(FName$)
show "r_core:", r_core:d3:"m"
show "n_cl:", n_cl:f3
show "n_max: ", n_max:f3
show "lambda: ", lambda:d3:"(n)m"
l_max:=l_max(lambda)
m_max:=m_max(lambda)
; Display all existing modes with their beta values
; in the output window:
show NoModes(lambda), " modes:"
for m:=1 to m_max do
for l:=0 to l_max do
if ModeExists(l,m,lambda)
```

```
then show “LP”, l, (if l>9 or m>9 then ”,”), m, ”: ”,
beta_lm(l,m,lambda)*1e-6:f5:“/μm”
ModeList$(lambda):=
list of all modes in text form
begin
global s$, lambda;
s$:=””;
for m:=1 to m_max(lambda)
do for l:=0 to l_max(lambda)
do if ModeExists(l,m,lambda)
then s$:=s$+”, LP”+str(l)+(if l>9 or m>9 then ”,”)+str(m);
copy(s$,3,1000);
end;
; Calculate maximum mode amplitudes for scaling purposes:
defarray A_max_lm[0,l_max; 1,m_max]
calc
begin
v_g_min:=c; v_g_max:=0;
for l:=0 to l_max
```

```
do for m:=1 to m_max
do if ModeExists(l,m,lambda)
then A_max_lm[l,m]:=sqrt(maxf(I_lm(l,m,lambda,r), r in [0, r_core],
divide=20, xtol=0.1e-6));
end
; - - - - - - - - - - - - -
lambda_p:=lambda
l_max:=l_max(lambda_p)
m_max:=m_max(lambda_p)
diagram 1, size_px=(600,80+((600)-50)*(m_max/(1+l_max)))
"Transverse Mode Profiles"
defarray I_max_lm[0,l_max; 1,m_max]
calc
begin
for l:=0 to l_max
do for m:=1 to m_max
do if ModeExists(l,m,lambda_p)
then I_max_lm[l,m]:=maxf(I_lm(l,m,lambda_p,r), r in [0, 2*r_core],
divide=20, xtol=0.1e-6);
```

```
end

x: -0.5, l_max+0.5, 1

"mode index l", @x

y: +0.5, m_max+0.5, 1

"mode index m", @y

frame

legpos 200, 0

hx hy

! r_max:=1.8*r_core

cp:

begin

var l, m, xm, ym, A;

l:=round(x);

m:=round(y);

if ModeExists(l,m,lambda_p)

then begin

xm:=l;

ym:=m;

A:=A_lm_xy(l,m,lambda_p,r_max*2*(x-xm),r_max*2*(y-ym))/sqrt(I_max_lm[l,m]);
```

```
color_A(A)

end

else white;

end

; - - - - - - - - - - - - - -

diagram 2, size_px=(600,400):

x: 0, L_f

"position in fiber (m)", @x

P_max:=P_in_max

P_max:=maxr(P_max, P(pump1_fw,L_f))

P_max:=maxr(P_max, P(pump1_bw,0))

P_max:=maxr(P¡*_max, P(signal1_fw,L_f))

P_max:=maxr(P_max, P(signal1_bw,0))

y: 0, 1.1*P_max

frame

legpos 200, 0

hx hy

f: P(pump1_fw, x),

color=red, width=3, "pump1_fw (W)"
```

f: P(pump1_bw, x),

color=red, style=dotdashed, width=3, "pump1_bw (W)"

f: P(signal1_fw, x),

color=blue, width=3, "signal1_fw (W)"

f: P(signal1_bw, x),

color=blue, style=dotdashed, width=3, "signal1_bw (W)"